Kinetic isotope and trace element partitioning during calcite precipitation from aqueous solution

by

Laura Christina Nielsen

A dissertation submitted in partial satisfaction of the
requirements for the degree of
Doctor of Philosophy

in

Earth and Planetary Science

in the

Graduate Division

of the

University of California, Berkeley

Committee in charge:

Professor Donald J DePaolo, Chair
Professor Burkhard Militzer
Professor Garrison Sposito

Spring 2012

Kinetic isotope and trace element partitioning during calcite precipitation from aqueous solution

Abstract

Kinetic isotope and trace element partitioning during calcite precipitation from aqueous solution

by

Laura Christina Nielsen

Doctor of Philosophy in Earth and Planetary Science

University of California, Berkeley

Professor Donald J DePaolo, Chair

Precipitation of carbonate minerals is ubiquitous in the near-surface environment, and the isotopic and trace element composition of carbonates may be used to reconstruct the conditions of growth. Little is known about the mechanisms controlling isotope and trace element distribution into carbonates. Proposed growth mechanisms are typically inferred from the supersaturation dependence of $CaCO_3$ precipitation rates. As different experimental techniques often generate different apparent reaction orders, numerous hypothesized mechanisms can be found in the literature. These descriptions of crystallization pathway cannot be used to identify processes controlling trace element and isotope partitioning.

Recent advances in experimental methodology allow us to observe microscopic to nanoscopic structures at the mineral surface during growth. The mechanisms controlling calcite growth have been directly determined by using fluid flow cells placed in an atomic force microscope (AFM; chapter 3). Calcite growth below the threshold oversaturation for amorphous calcium carbonate (ACC) formation – typical of seawater and most terrestrial fluids – occurs primarily through the attachment of ions to kink sites on the surface. The net flux of ions to kink sites governs both overall growth rate and mineral composition.

In this thesis, I present a self-consistent model based on observed calcite growth mechanisms that may be used to predict growth rate (chapter 1), and isotopic (chapter 2; Nielsen et al., 2012) and trace element (chapter 5; Nielsen et al., in prep) partitioning as a function of solution composition. I apply this model to calcium isotope fractionation during the precipitation of synthetic calcite, which I grew and analyzed using novel secondary ion mass spectrometry (SIMS) methods (chapter 3). In chapter 4 (Nielsen and DePaolo, in review), I model calcium isotope fractionation in carbonate minerals that I collected from the highly alkaline Mono Lake, CA. The mechanistic framework developed here may be extended to multicomponent systems, and may be adapted for use in reactive transport models. When interpreted through the lens of this model, trace element and isotope signatures preserved in carbonates may eventually be used to reconstruct the chemistry of natural aqueous fluids.

To my Family

and

To Devin.

Contents

List of Figures

List of Tables

List of Symbols

Variable	Units	Description
a	m	molecular spacing along the step
a_j	M	activity of j in solution
α	J/m^2	step edge free energy per unit step height
α_b		fractionation factor during detachment
α_{eq}		equilibrium fractionation factor
α_f		fractionation factor during attachment
b	m	kink depth
β_{st}		step kinetic coefficient
ΔG^*	J	Gibbs free energy of the critical nucleus
d	mol/m^3	solid density
ϵ_j	J	kink site formation energy
γ	J/m	edge free energy of the critical nucleus
γ_{AB}		activity coefficient of mineral AB in a solid solution
h	m	step height
I	m^{-2}s^{-1}	nucleation frequency
i	s^{-1}	rate of stable kink formation (1D nucleation rate)
K_{sp}		equilibrium solubility
k	J/K	Boltzmann constant
k_j	s^{-1} M^{-1}	rate coefficient of j attachment to a kink site
ν_j	s^{-1}	rate coefficient of j detachment from a kink site
ξ_j		2D nucleus shape factor
Ω	m^3	growth unit volume
P_j		probability that a given kink site is a j site
R_i^j	mol m^{-2} s^{-1}	rate of reaction j for ion i
r		flux ratio
r_a		A:B ion activity ratio (solution stoichiometry)
r_x		isotope ratio of the solution
r_x		isotope ratio of the crystal
ρ		kink density
S		oversaturation (IAP/K$_{sp}$)
σ		supersaturation (ln(IAP/K$_{sp}$))
$\Sigma\Pi$		total solubility
T	K	temperature
u_j	s^{-1}	propagation rate of kink type j
v_{st}	m/s	lateral step velocity
x		solid mole fraction
y		aqueous mole fraction
y_0	m	step spacing or terrace width
$[j]$	M	concentration of j in solution
(j)	M	activity of j in solution

Acknowledgments

This thesis represents my attempt to synthesize and build upon the scientific perspectives of my advisors here at UC Berkeley. These include several stellar scientists – Donald DePaolo, Garrison Sposito, Jim DeYoreo and Ian Bourg – whose mentorship has been crucial to my growth. My primary advisor, Donald DePaolo, deserves my deepest gratitude for his supportiveness and (occasionally tacit) encouragement. He *tried* to keep my mind on the big picture. Jim De Yoreo helped me access the tools and knowhow required to understand the molecular mechanisms governing crystal growth. His body of work drew me towards the fascinating realm of micro- and nano-scale surface processes. Garrison Spositio and Ian Bourg were my collaborators for a project not included in this thesis, but their ideas and demeanor have had a profound influence on my development. I took several of Gary's courses, and each lecture was a great pleasure to attend. I hope to have absorbed some of their calm curiosity and poise.

No graduate education is complete without the unique sort of interaction that happens between graduate students. My UC tenure was filled with folks whom I now consider to be both colleagues and friends. These people include Jim Watkins, Jenny Druhan, Amy Hofmann, Brook Peterson, Sarah Brownlee, Joanne Emerson, Tyler Arbour, Zack Geballe, Peter Olds, Bill Mitchell, and Ben Legg, among others. Thanks for all of your support, for our interesting discussions, and for getting excited about science with me!

Thanks to the scientists, technicians and administrators who have helped me without question: Marilyn Saarni, Tom Owens, Shaun Brown, Wenbo Yang, Joern Larsen, April Van Hise, Laurence Miller, Marion Banks, Dawn Geddes, Micaelee Ellswythe, and Margie Winn. You have all greatly improved my time here at Berkeley.

Time spent with friends and family has kept me balanced and happy for the past four years. Thanks, mom and dad, for 25 years of supporting me, loving me, and giving me the tools – and the freedom – to discover what I'm passionate about. Needless to say, I wouldn't be here with out you. Thanks, sister Karen, for inspiring me to be a strong and independent woman. Thanks, friends, for loving me, and filling my life with happiness and excitement. Jackie Keller, Rachel Hochman, Ben Koons, Katie Ammons, David Strauss, Ali Frizell and Leslie Rice, thank you for being there for me when I need you. Lastly I would like to thank the love of my life, my fiancé Devin Lammers. He supported my decision to go to Berkeley, even though it made things harder for us in the short term; he gave up a stellar situation in Colorado to join me in the Bay; he's showed me more happiness than I thought I was capable of experiencing. And the adventure's only just begun!

Many thanks are due to the ARCS foundation, which sponsored my first two years of graduate school, and to the Class of 1951 Chair for conference and travel support. Funding for this research was provided in part by the Center for Nanoscale Control of Geologic CO_2, an Energy Frontier Research Center funded by the U.S. Department of Energy, Office of Science, Office of Basic Energy Sciences under Award Number DE-AC02-05CH11231 and by the Director, Office of Science, Office of Basic Energy Sciences, of the U.S. Department of Energy under Contract No. DE-AC02-05CH11231.

Chapter 1

Kinetics and mechanisms of calcite growth

1.1 Introduction

Mineral precipitation from aqueous solution is a widely studied process, with direct relevance to aqueous and environmental geochemistry, geobiology, and industry. Macroscopic descriptions of growth and dissolution rate laws for $CaCO_3$ abound in the geochemical literature, (e.g. Chou et al., 1989; Zuddas and Mucci, 1994; Zhang and Dawe, 1998; Morse and Arvidson, 2002; Steefel and Maher, 2009). Traditionally, growth rate laws have been cast in terms of supersaturation with respect to a given mineral phase,

$$R = k[\Omega - 1]^n, \tag{1.1}$$

where k is the rate constant for forward reaction, $\Omega = IAP/K_{sp}$ is oversaturation, IAP is the ion activity product, K_{sp} is solubility and n represents the order of the rate law, with the n=1 case representing a linear rate law. When expressed in this fashion, the kinetics of processes directly observed during calcite precipitation – for example kink and step propagation on the mineral surface – are not considered. Furthermore, the net attachment rates of individual constituents such as Ca^{2+} and its isotopologues, and the effect of solution stoichiometry or the ratio of Ca^{2+}:CO_3^{2-} on these rates, cannot be explicitly modeled. Unlike traditional growth rate laws, microscopic models for mineral precipitation (e.g. Burton et al., 1951; Zhang and Nancollas, 1990) can be used to directly quantify the net fluxes of ions to observed microscopic growth features. In this chapter, we detail a microscopic model based on the work of Zhang and Nancollas (1998) that accurately captures the kinetics of calcite precipitation from aqueous solution, which we extend in later sections to model surface controlled isotope fractionation and trace element partitioning.

1.2 Microscopic and macroscopic models of calcite growth kinetics

The first microscopic descriptions of mineral growth kinetics arose during the 1950s. The seminal Burton, Cabrera, & Frank (1951; BCF) paper details what is now referred to as terrace-ledge-kink (TLK) theory, a thermodynamic description of the microscopic structure of mineral surfaces and classical, dislocation-driven mineral growth. This paper identified ubiquitous microscopic features occurring at the surface of minerals including steps and kinks, which will be discussed in detail below (Figure 1.1). TLK theory has been applied to model mineral growth from aqueous solution in numerous systems, including KH_2PO_4 (KDP) (DeYoreo et al., 1994) and calcite (Teng et al., 1998, 1999, 2000).

Application of the TLK model is not strictly valid in the case of relatively insoluble minerals where kink formation is limited by the rate of stable 1D nucleation along the step (DeYoreo et al., 2009). More recent models of kink creation, propagation, and collision (CPC) may be used to quantify kink densities of lower-solubility minerals such as calcite (Zhang and Nancollas, 1990, 1998; Larsen et al., 2010).

Calcium carbonate mineral precipitation has been extensively studied as a model system for both microscopic (Dove et al., 2008; Teng et al., 1998, 2000), and macroscopic (Zhang and Dawe, 1998; Tang et al., 2008a; DePaolo, 2011) theories for mineral growth and trace element and isotope distribution. Teng et al. (2000) applied BCF theory to calcite precipitation and demonstrated that dislocation-driven spiral growth is the dominant growth mechanism at low thermodynamic driving force (i.e. low oversaturation), while at higher oversaturation, step generation and growth is driven by 2D nucleation. Each growth mechanism is associated with distinct microscopic surface structures and corresponding rate laws: dislocation-driven step growth rate is a linear function of oversaturation as predicted by classical (e.g. BCF) theory, while higher order rate laws, (e.g. Malkin et al., 1989; van der Eerden, 1993; Dove et al., 2008), describe 2D nucleation-driven growth at low oversaturations.

Zhang and Nancollas (1998) detailed a model for ion-by-ion AB (NaCl structure) crystal growth based on CPC theory, which accounts for the stoichiometry of the growth solution. This model applies a kinetic steady state approach and considers the elementary attachment and detachment of ions to and from the mineral surface (Zhang and Nancollas, 1990). Though the theory was explicitly derived for the (001) face of an AB crystal, Larsen et al. (2010) demonstrated that this theory can accurately predict changes in calcite precipitation rate on the calcite $\{10\bar{1}4\}$ face due to changes in solution stoichiometry, and Wolthers et al. (2012) have recently extended the model to account for solution pH.

In this chapter, I introduce a model for growth rate as a function of oversaturation and solution stoichiometry for the cases of spiral dislocation- and 2D nucleation-driven step growth, based on reactions occurring at microscopic features on the mineral surface. I extend the Zhang and Nancollas (1998) model of ion-by-ion growth for an AB crystal, allowing for differences in A and B ion attachment and detachment kinetics. It will be shown that the exchange of ions between the mineral surface and aqueous solution are controlled by

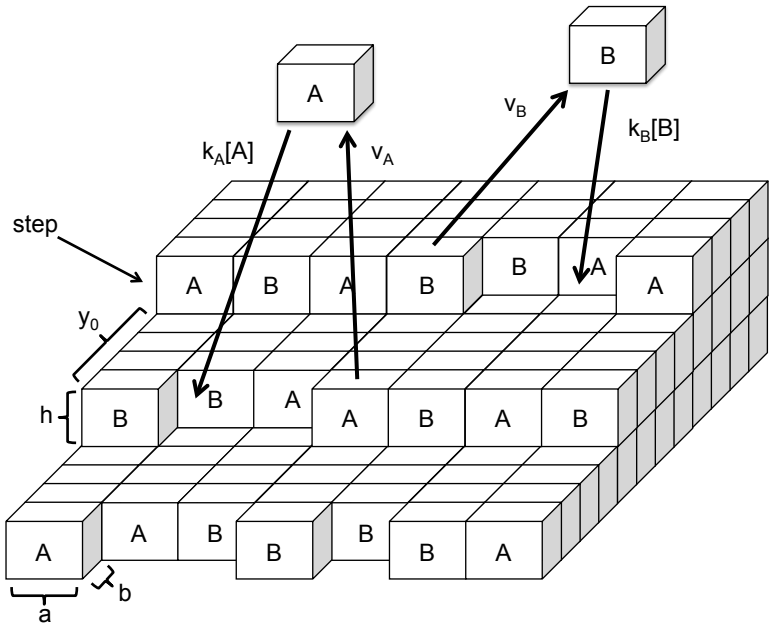

Figure 1.1: Schematic of kink sites and step edges at the AB mineral surface. Aqueous ions of type A exchange with the surface via attachment (with frequency $k_A(A)$ ($s^{-1}M^{-1}$)) and detachment (with frequency ν_A (s^{-1})) to and from kink sites. Step height (h), terrace width (y_0), kink depth (b), and molecular unit width (a) are depicted.

the density and composition of reactive kink sites. In chapter 2, a third component A' is introduced into the kinetic theory. This derivation can describe the step velocity anisotropy of acute and obtuse faces of spiral growth hillocks observed in calcite. Exchange of ions between mineral kink sites and aqueous solution dictates the final trace element and isotopic composition of the mineral, so we extend this model for the first time in chapters 2 and 5 to describe isotopic and trace element partitioning during surface controlled mineral growth.

1.3 Mechanics of AB crystal growth

The surface of a sparingly soluble AB mineral such as calcite in contact with aqueous solution is schematically depicted in Fig. 1.1. Assuming that the oversaturation is smaller than that at which amorphous precursor phases are generated, mineral growth and dissolution proceed via the advancement and retreat of monomolecular steps across the surface. At low oversaturations, steps are generated at dislocations on the surface, leading to the formation of growth hillocks (Figure 1.2; Teng et al., 2000). At higher oversaturations, the thermodynamic driving force becomes sufficiently high to cause heterogeneous nucleation on the surface (Teng et al., 2000). The resulting 2D nuclei act as sources of step edges

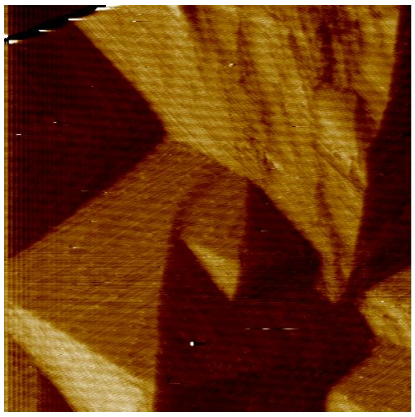

Figure 1.2: AFM image of calcite growth hillocks during precipitation from supersaturated aqueous solution. Scale is 10 × 10 μm, and monomolecular steps are visible along the sides of the hillocks.

analogous to growth hillocks. The advancement of these steps drives overall mineral growth. In both cases, A and B ion attachment and detachment occur primarily at kink sites along step edges, offsets in the step of one molecular unit width where a large number of chemical bonds are unsatisfied. If an individual growth unit is a molecule (i.e. CO_3^{2-}), the molecular orientation at the step edge may affect kink structure and therefore the energetics of bond formation and breaking. On the primary cleavage face of calcite, $\{10\bar{1}4\}$, carbonate ionic units are oriented at an angle to the surface, forming obtuse (+) and acute (−) steps, which may travel at different speeds under different solution compositions.

1.4 Spiral growth of non-Kossel AB crystals

Rate of ion incorporation and exchange

The growth of an AB crystal may be modeled by quantifying the relative rates of ion incorporation and back exchange with solution. For a two-component mineral with an NaCl structure growing via dislocation-driven step growth (spiral growth) from aqueous solution, the net rate of ion incorporation ($\frac{molAB}{m^2 s}$) depends on the difference of ion fluxes to (R_f) and from (R_b) the mineral surface,

$$R_{net} = \frac{R_f - R_b}{2} = \frac{\rho u h b d}{2 y_0}, \tag{1.2}$$

where ρ is kink density (unitless) or the probability of a given site being a kink site, u is the net overall kink propagation rate (s^{-1}), h is the unit step height (m), d is the solid phase density (mol/m^3), b is kink depth (m), and y_0 is the step spacing (m). The total rate of A

and B ion attachment to the surface is $R_f = R_A^f + R_B^f$ ($\frac{mol}{m^2 s}$), and the rate of detachment from the surface is $R_b = R_A^b + R_B^b$ in the same units. For component A,

$$R_A^{net} = R_A^f - R_A^b. \tag{1.3}$$

Based on mineral surface geometry, the net rate of surface normal mineral growth due to A incorporation ($\frac{molA}{m^2 s}$) is equal to:

$$R_A^{net} = \frac{\rho u_A^{net} hbd}{y_0} = \frac{v_{st} bd}{y_0} \tag{1.4}$$

where u_i^{net} is the rate of kink propagation for ion i (s^{-1}), and v_{st} is the lateral step velocity (m/s). For a pure AB mineral, $R_A^{net} = R_B^{net} = R_{net}$ to preserve crystal stoichiometry. Kink density ρ is defined as a/x_0, where x_0 (m) is the average distance between kink sites along a step, and a is the intermolecular distance along the step (m). Rate of kink propagation, u_{net}, is the net frequency of attachment of ions to a kink site. Step spacing or terrace width may be expressed as $y_0 = 4\Gamma L_c$ for a symmetrical growth hillock (Teng et al., 2000), where Γ is approximately equal to 1 for calcite and L_c is critical step length,

$$L_c = \frac{2h|\vec{a} \times \vec{b}|\alpha}{kT\sigma}, \tag{1.5}$$

which depends on step edge free energy per unit step height α (J/m^2), the Boltzmann constant k (J/K), temperature T (K), and oversaturation $\sigma = ln(IAP/K_{sp})$. Asymmetrical growth hillocks may be generated in minerals such as calcite by growth rate anisotropy, where obtuse and acute step velocities are not equal (see Appendix B). The rate formulation presented thusfar assumes that all ion attachment and detachment occurs at kink sites and that 2D nucleation is insignificant (Zhang and Nancollas, 1998).

Assuming an A ion can only be added to a B kink site and removed from an A site (e.g. Fig. 1.1), the rate of A kink propagation may be written,

$$u_A = u_A^f - u_A^b, \tag{1.6}$$

where the frequency of A detachment from A kink sites with detachment rate constant ν_A (s^{-1}) is equal to

$$u_A^b = \nu_A P_A, \tag{1.7}$$

and the frequency of A addition to B kinks with attachment rate constant k_A (s^{-1} M^{-1}) is equal to

$$u_A^f = k_A(A) P_B. \tag{1.8}$$

P_A and P_B are the probabilities of a given kink site being an A or B site respectively (Zhang and Nancollas, 1998), and parentheses denote ion activity. The overall kink propagation rate is the sum of A and B net kink propagation rates, $u = u_A + u_B$. All kink sites are either A or B sites, so $P_A + P_B = 1$.

Combining Eqs. 1.4 and 1.6 - 1.8, the forward and back fluxes of A at the surface become:

$$R_A^f = \frac{\rho k_A(A) P_B hbd}{y_0} \tag{1.9}$$

and

$$R_A^b = \frac{\rho \nu_A P_A hbd}{y_0}. \tag{1.10}$$

Kink site composition

Net ion fluxes and therefore growth rate depend on the overall kink density, so the relative abundances of A and B kink sites must be determined. During growth or dissolution, the rate of addition of A must always equal that of B to preserve crystal stoichiometry, so

$$u_A = u_B. \tag{1.11}$$

It follows from Eqs. 1.6-1.8 that $k_A(A)P_B - \nu_A P_A = k_B(B)P_A - \nu_B P_B$. Substituting $1 - P_A$ for P_B, we find that the probability that a given kink site is an A or B site respectively is:

$$P_A = \frac{k_A(A) + \nu_B}{k_A(A) + k_B(B) + \nu_A + \nu_B}, \tag{1.12}$$

and

$$P_B = \frac{k_B(B) + \nu_A}{k_A(A) + k_B(B) + \nu_A + \nu_B}. \tag{1.13}$$

Calculation of surface kink density

The balance of kink site formation via 1D nucleation of AB ion pairs and annihilation via kink collision dictates the steady state kink density of the mineral surface. When the rate of 1D nucleation is equal to i, and the kink propagation rate is u,

$$\rho = 2\sqrt{\frac{i}{2u}}. \tag{1.14}$$

A derivation of this expression may be found in Appendix A.

For an AB crystal, Zhang and Nancollas (1998) determined a simplified expression for the rate of formation of stable 1D nuclei, i, as a function of solution composition,

$$i_A = 2\exp\left(\frac{-2\epsilon_A}{kT}\right)(S-1)\frac{\nu_B k_A(A)}{k_A(A) + \nu_B}, \tag{1.15}$$

and

$$i_B = 2\exp\left(\frac{-2\epsilon_B}{kT}\right)(S-1)\frac{\nu_A k_B(B)}{k_B(B) + \nu_A}, \tag{1.16}$$

where S is oversaturation defined as $S = \frac{(A)(B)}{K_{sp}}$ $(= \Omega)$, ϵ_j is the kink formation energy of a j kink site (J) and $i = \frac{i_A + i_B}{2}$. Kink formation energy is related to solid-solid and solid-fluid AB bond energies (Zhang and Nancollas, 1990). Combining Eqs. 1.6 - 1.8 and identical equations for B, the kink propagation rate becomes

$$u = \frac{2k_A k_B(A)(B) - 2\nu_A \nu_B}{k_A(A) + k_B(B) + \nu_A + \nu_B} \tag{1.17}$$

(Zhang and Nancollas, 1998).

Eqs. 1.15 - 1.17 may be substituted into Eq. 1.14 to calculate kink density along the step:

$$\rho = \left[(S-1)\left(\left[\exp\left(\frac{-2\epsilon_A}{kT}\right)\frac{\nu_B k_A(A)}{\nu_B + k_A(A)}\right] + \left[\exp\left(\frac{-2\epsilon_B}{kT}\right)\frac{\nu_A k_B(B)}{\nu_A + k_B(B)}\right]\right) \left(\frac{\nu_A + \nu_B + k_A(A) + k_B(B)}{k_A(A)k_B(B) - \nu_A\nu_B}\right)\right]^{1/2}. \tag{1.18}$$

A simplified expression may be found in Zhang and Nancollas (1998), where the attachment and detachment flux constants of A are assumed to equal those of B.

Growth rate as a function of oversaturation and solution stoichiometry

To obtain growth rate in terms of solution saturation (S) and stoichiometry $(r_a = (A)/(B))$, attachment and detachment fluxes must be recast in terms of S and flux ratio r. As in Zhang and Nancollas (1998), we define flux ratio such that

$$r = \frac{k_A}{k_B} r_a. \tag{1.19}$$

The solubility of an AB crystal is defined as $K_{sp} = (A)_{eq}(B)_{eq}$. At equilibrium, the forward and back fluxes of A and B are equal, so $\rho k_A (A)_{eq} P_B = \rho \nu_A P_A$, thus

$$(A)_{eq} = \frac{\nu_A P_A}{k_A P_B}. \tag{1.20}$$

Similarly,

$$(B)_{eq} = \frac{\nu_B P_B}{k_B P_A}. \tag{1.21}$$

These equations simplify to,

$$K_{sp} = \frac{\nu_A \nu_B}{k_A k_B}, \tag{1.22}$$

which is solubility expressed in terms of the forward and backward flux coefficients. By substituting Eq. 1.22 into the standard equation relating S and K_{sp} we obtain an expression for S in terms of the flux coefficients and the aqueous ion concentrations,

$$S = \frac{k_A k_B (A)(B)}{\nu_A \nu_B}, \tag{1.23}$$

which then also allows us to write the forward ionic fluxes in terms of S and r as:

$$k_B(B) = \left(S \frac{\nu_A \nu_B}{r} \right)^{1/2}, \tag{1.24}$$

and

$$k_A(A) = \left(S \nu_A \nu_B r \right)^{1/2}. \tag{1.25}$$

The overall precipitation rate, R_{net} may now be expressed in terms of oversaturation, S, and flux ratio, r, by substituting ρ (Eq. 1.18) and u (Eq. 1.17) into Eq. 1.2:

$$R_{net} = \frac{hbd}{2y_0} \Bigg\{ \left[\left(\exp\left(\frac{-2\epsilon_A}{kT} \right) \frac{\nu_B^{3/2} (S\nu_A r)^{1/2}}{\nu_B + (S\nu_A\nu_B r)^{1/2}} \right) + \left(\exp\left(\frac{-2\epsilon_B}{kT} \right) \frac{\nu_A^{3/2} (S\frac{\nu_B}{r})^{1/2}}{\nu_A + (S\frac{\nu_A\nu_B}{r})^{1/2}} \right) \right] \left[\frac{\nu_A + \nu_B + (S\nu_A\nu_B r)^{1/2} + (S\frac{\nu_A\nu_B}{r})^{1/2}}{\nu_A + \nu_B} \right] \Bigg\}^{1/2} \left[\frac{2\nu_A\nu_B(S-1)}{\nu_A + \nu_B + (S\nu_A\nu_B r)^{1/2} + (S\frac{\nu_A\nu_B}{r})^{1/2}} \right]. \tag{1.26}$$

Step velocity (m/s) may similarly be written in terms of S and r (i.e. Eq. 1.4):

$$v_{st} = \frac{R_{net} y_0}{bd} = \rho u h. \tag{1.27}$$

The dependence of growth rate, R_{net}, on S and r_a is plotted in Fig. 1.3. Rate is maximized at high oversaturation and Ca^{2+}:$CO_3^{2-} \sim 1$ when $\nu_A \sim \nu_B$ and $k_A \sim k_B$. Fig. 1.3 also shows that R_{net} is more strongly dependent on S than on r, but that r can change R_{net} by about a factor of 10 when increased or decreased by 3 orders of magnitude, a range that is accessed in natural aqueous solutions.

The rate of exchange of a given ion between the mineral surface and aqueous solution dictates the ultimate trace element and isotopic composition of the solid phase (DePaolo, 2011). The relative exchange flux for A may be expressed as a function of supersaturation, S, and flux ratio, r (Eq. 1.19), from the ratio of back to forward reaction rates:

$$\frac{R_A^b}{R_A^f} = \frac{\nu_A P_A}{k_A(A) P_B} = \frac{\nu_A}{k_A(A)} \left(\frac{\nu_B + (S\nu_A\nu_B r)^{1/2}}{\nu_A + (S\frac{\nu_A\nu_B}{r})^{1/2}} \right). \tag{1.28}$$

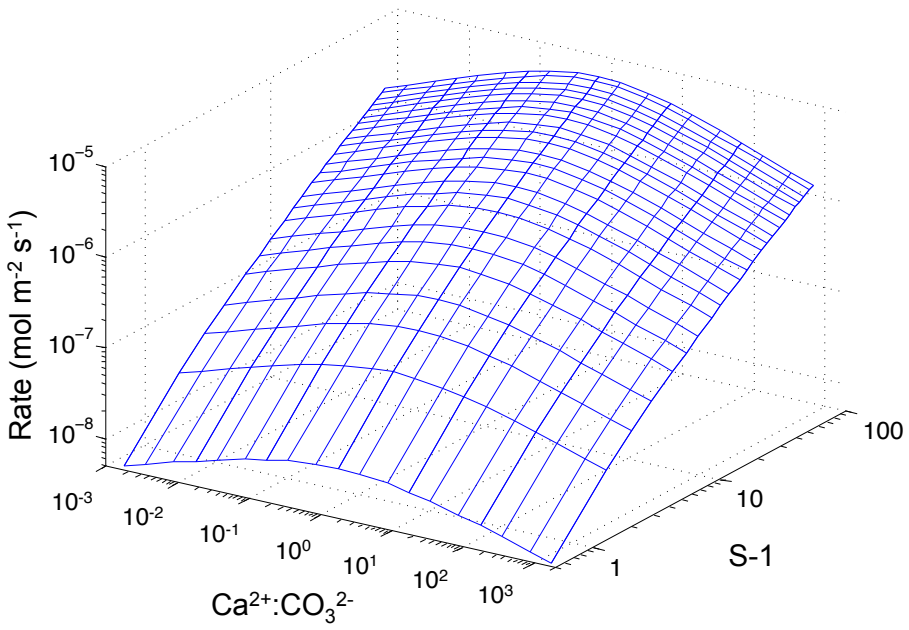

Figure 1.3: Growth rate modeled as a function of oversaturation, S, and solution stoichiometry,r_a, based on Eq. 1.26 and parameters used in fit B (see section 2.4). For a given oversaturation, growth rate is greatest at Ca^{2+}:CO_3^{2-} = 1, when $\nu_A = \nu_B$ and $k_A = k_B$.

If we assume that the rate coefficients of A and B ion attachment and detachment are equal (e.g. $k_A = k_B$ and $\nu_A = \nu_B$) and substitute Eqs. 1.19, 1.24, and 1.25, Eq. 1.28 reduces to:

$$\frac{R_A^b}{R_A^f} = \frac{1}{\sqrt{Sr_a}}\left(\frac{1+\sqrt{Sr_a}}{1+\sqrt{S/r_a}}\right), \tag{1.29}$$

which is solely dependent on mineral solubility and solution composition. The exchange flux of A based on Eq. 1.29 is plotted as a function of oversaturation and solution stoichiometry in Fig. 1.4. High values of R_b/R_f for A promote equilibrium fractionation or partitioning of A isotopes between the solid phase and aqueous solution. Conversely, low values of R_b/R_f drive the mineral-aqueous system towards kinetic control. Decreasing R_b/R_f may be accomplished by increasing oversaturation, because with increasing S, the first term on the right hand side of Eq. 1.29 decreases. Decreasing A:B (r_a) also decreases R_b/R_f, because decreasing r_a simultaneously decreases the numerator and increases the denominator of the term in parentheses of Eq. 1.29 (Fig. 1.4).

In DePaolo (2011), the backward flux R_b is assumed to equal the mineral dissolution rate under infinite undersaturation at appropriate P, T and pH. According to the model

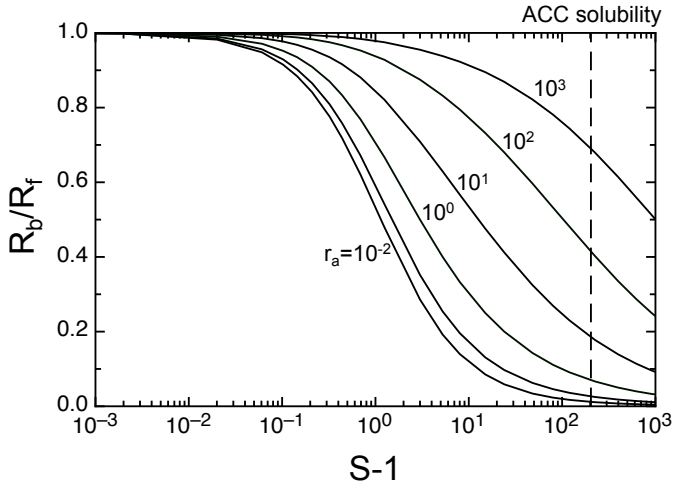

Figure 1.4: Plot of Ca exchange flux ratio, R_b/R_f (Eq. 1.29), as a function of oversaturation S and the Ca^{2+}:CO_3^{2-} activity ratio in solution (r_a). Increasing S or decreasing r_a will decrease the magnitude of the backward exchange flux (R_b) relative to the forward reaction flux (R_f), driving the system towards kinetically controlled isotope or trace element partitioning. Typical seawater r_a values vary from 10^2 to 10^3. The dashed line indicates where amorphous calcium carbonate (ACC) will begin to form. An important feature illustrated here is that the S at which R_b/R_f approaches 1 depends strongly on r_a. Also, the transition from near equilibrium conditions ($R_b >> R_f$) to kinetically controlled conditions ($R_b << R_f$) occurs over a larger range of S as r_a increases. This is a condition that is recognized by DePaolo as being needed to fit available data and is explained here by invoking a microscopic model of crystal growth (DePaolo, 2011).

presented here, the net detachment flux of A and B varies with both oversaturation S and solution stoichiometry, although R_b is close to the measured calcite dissolution rate under the S and r_a conditions applicable to seawater and to the available laboratory measurements of Ca isotope fractionation (Fig. 1.5).

1.5 Higher order growth rates and nucleation

The derivation presented above for the relationship between R_{net}, S, and r_a for spiral growth (e.g. Figure 1.2) must be modified for high oversaturations where the spiral growth mechanism does not operate. With increasing oversaturation, the dominant mechanism of step initiation undergoes a transformation, where steps initially sourced from screw dislocations on the surface begin to nucleate directly on the surface as 2D islands. This transformation is associated with a higher-order dependence of growth rate on oversaturation at

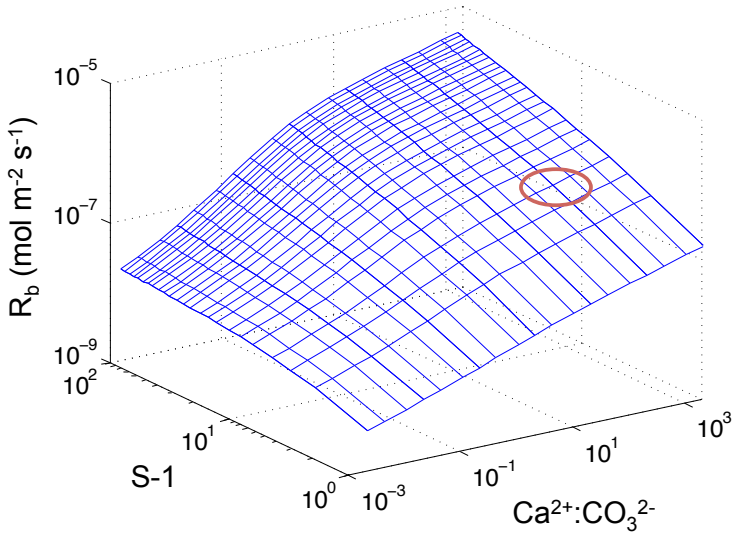

Figure 1.5: Net ion detachment flux modeled as a function of oversaturation and solution stoichiometry using Eqs. 1.10, 1.5, and 1.18, and fit B parameters (see section 2.4). Oval shows the expected R_b value range for solutions with surface seawater-like values of S and r_a. The expected values are close to the value of 6×10^{-7} mol m^{-2} s^{-1} assumed by DePaolo (2011) to be the value of R_b appropriate to modeling the experiments of Tang et al. (2008a) .

low oversaturations (e.g. Teng et al., 2000), which converges to a first order rate dependence at high oversaturations. Van der Eerden (1993) determined an expression for the rate of surface normal growth (m/s) driven by 2D nucleation:

$$R = 1.137h\left(Iv_{st}^2\right)^{1/3}, \tag{1.30}$$

where h is step height, I is nucleation frequency (m^{-2} s^{-1}), and v_{st} is step velocity (m/s). Nucleation frequency may be written

$$I = \beta_{st}\frac{h}{\Omega_V}\left(\frac{\xi_2 h\sigma}{\pi\Omega_V}\right)^{1/2} exp\left(\frac{-\Delta G^*}{kT}\right) \tag{1.31}$$

where ξ_2 is an area shape factor, ΔG^* is the excess Gibbs free energy of the critical nucleus relative to an empty terrace, Ω_V is the growth unit volume (e.g. $\sim hab$), and β_{st} is the step kinetic coefficient (van der Eerden, 1993). The step kinetic coefficient of van der Eerden (1993) depends on step velocity following,

$$\beta_{st} = \frac{v_{st}}{\sigma}. \tag{1.32}$$

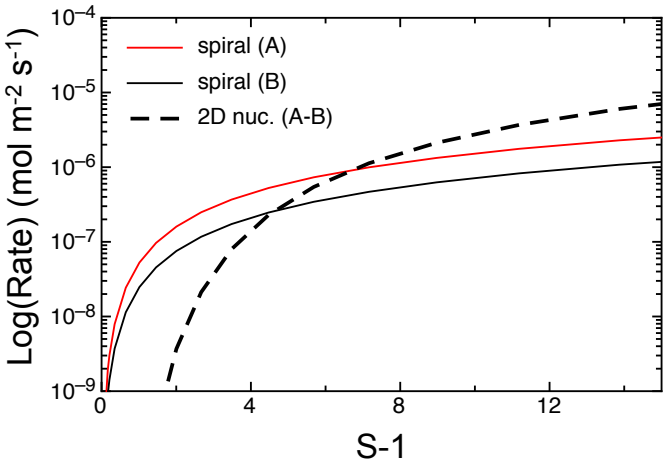

Figure 1.6: Spiral- and 2D nucleation-driven growth rates (Eqs. 1.26 and 1.30) plotted as a function of oversaturation for model parameters obtained for fits A and B (section 2.4). At low oversaturation, dislocation driven step growth controls growth rate, but above the critical supersaturation (i.e. the intersection of both curves), 2D nucleation controls rate. The transition to 2D nucleation-driven growth occurs at lower supersaturation for fit B, which has a higher step edge free energy per unit step height.

This differs from a more typical expression for β_{st}, where the step kinetic coefficient is assumed to be proportional to the difference between the mineral constituent ion concentration in solution and its equilibrium concentration, (e.g. Teng et al., 2000).

Following van der Eerden (1993), the free energy barrier of forming a critical 2D nucleus depends on oversaturation, the chemical driving force for growth:

$$\Delta G^* = \frac{\xi \Omega_V \gamma^2}{hkT\sigma}, \tag{1.33}$$

where γ is the average edge free energy of the nucleus in J/m, and $\xi = 2\xi_2/\xi_1^2$. If I^* is the radius of a rhombic critical nucleus, the perimeter of the nucleus is $\sim \xi_1 \times \mathrm{I}^* \simeq 8 \times \mathrm{I}^*$, and the area of the nucleus is $\sim \xi_2 \times \mathrm{I}^{*2} \simeq 4 \times \mathrm{I}^{*2}$. Thus $\xi \simeq 1/8$.

1.6 Transition from step growth to 2D nucleation

At low oversaturations, dislocation driven step growth will control overall growth rate, because the thermodynamic driving force for formation of 2D nuclei is too low. Above a threshold oversaturation, which can be determined by setting Eqs. 1.26 and 1.30 equal, 2D nucleation will drive growth (Fig. 1.6). The value at which this transition occurs is sensitive to the average edge free energy of the nucleus γ (Eq. 1.33), the kinetic coefficient β_{st} (Eq.

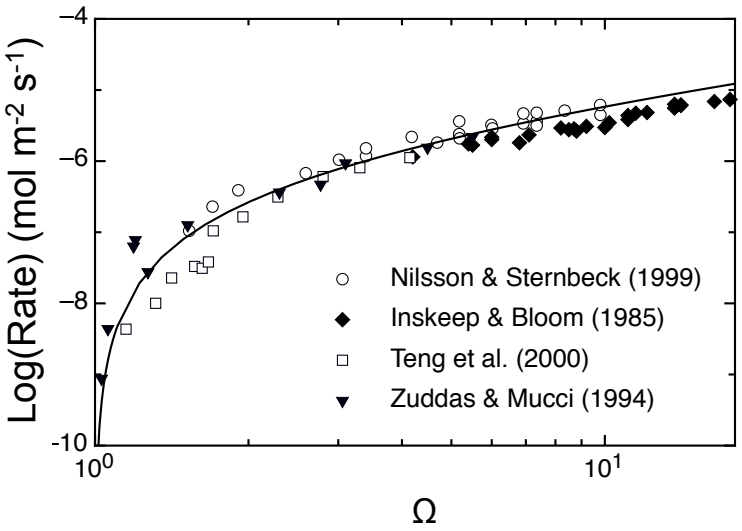

Figure 1.7: Compilation of calcite precipitation rate data modeled using Eq. 1.26 (black line).

1.31), and the mineral step edge free energy per unit step height α (Eq. 1.5). Typical values for calcite are poorly constrained, because the presence of contaminants can significantly reduce the free energy barrier for 2D nucleation, leading to very low apparent threshold supersaturations. The use of a background electrolyte can also significantly reduce the free energy barrier for nucleation, by decreasing the free energy of the surface via non-specific ion adsorption (i.e. Butt et al., 2006). Experiments conducted by Teng et al. (2000) place the transition at around $\sigma \sim 1$ ($S = 2.7$) for calcite, which is considered a lower limit. Fig. 1.6 gives a graphical illustration of the rates associated with the two growth mechanisms, using the parameters employed in fit B described in section 2.4 below, to fit experiments conducted in the absence of significant background electrolyte (Tang et al., 2008b).

1.7 Comparison with experiments

The kinetics of calcite precipitation have been extensively studied using a wide array of experimental techniques and solution compositions (Wiechers et al., 1975; Plummer et al., 1979; Inskeep and Bloom, 1985; Nilsson and Sternbeck, 1999; Teng et al., 2000; Larsen et al., 2010). The most common methods include free drift, pH-stat (Inskeep and Bloom, 1985; Burton and Walter, 1987), chemostat (constant addition Mucci, 1986; Zhong and Mucci, 1993; Zuddas and Mucci, 1994), CO_2 diffusion (Tang et al., 2008b) and fluid cell flow experiments (Teng et al., 2000; Larsen et al., 2010). In the case of pH-stat and chemostat experiments, CO_2 gas is bubbled into the growth solution, which is titrated to maintain a

steady state pH. Experiments of this form, and those that use CO_2 diffusion, are fraught with difficulty because the kinetics of CO_2 hydration are sluggish (Johnson, 1982). Despite the slow equilibration of aqueous species, equilibrium speciation is carried out to determine the concentration of CO_3^{2-} – and thus Ω (= IAP/K_{sp}) – of the growth solution.

The difficulty of controlling and quantifying the solution composition may be overcome by using appropriate methods. CO_2 hydration is faster at lower pH, so pH-stat or chemostat experiments performed at relatively low pH ($< \sim 7.3$) are likely to be more viable. Experiments that allow the solution composition to vary and that calculate growth rate based on the slope of concentration vs. time curves (i.e. free drift) are not subject to error induced by speciation kinetics. Free drift methods for calcite growth (Wiechers et al., 1975) and dissolution (Plummer et al., 1979) routinely yield first order rate dependencies, while pH-stat methods have yielded growth and dissolution reaction orders from 1 to 3 or greater (Table 1.1; Chou et al., 1989). Experimental designs that ensure constant calcium and carbonate ion activity by constant fluid flow over calcite seed (Teng et al., 2000), titration of equimolar Ca^{2+} and CO_3^{2-} (Nilsson and Sternbeck, 1999), or those that avoid bubbling CO_2 into the system (Inskeep and Bloom, 1985) generally yield growth rate dependencies consistent with a partial reaction order of ~ 1 at oversaturations greater than ~ 3, are considered to be reliable.

In Fig. 1.7 we fit the surface reaction model (e.g. Eq. 1.26) to the precipitation rate data that are internally consistent and follow the criteria listed above. Fitting is discussed in detail in section 2.4, and here we use the parameters from Table 2.1, and the attachment

Table 1.1: Experimental determinations of calcite precipitation kinetics. Partial reaction orders are listed for studies with rate data that cannot be modeled using the mechanistic framework described in this chapter.

Study	**Method**	**CO_2 bubbling**	**(Rxn. order)**
Zhong and Mucci (1993)	constant addition	Y	(4.0)
Tang et al. (2008b)	CO_2 diffusion	Y	(3.2)
Burton and Walter (1987)	pH-stat	Y	(2.3)
Mucci (1986)	constant addition	Y	(3.5)
Lopez et al. (2009)[1]	constant addition	Y	
Zuddas and Mucci (1994)	constant addition	Y	(3.3)[2]
Inskeep and Bloom (1985)	pH-stat	N	
Nancollas and Reddy (1971)	free drift	N	
Teng et al. (2000)	flow	N	
Zhang and Dawe (1998)	free drift	N	
Nilsson and Sternbeck (1999)	constant composition	Y	

[1] Fitted in chapter 5.

[2] Only for experiments performed at pH > 7.3.

and detachment rate coefficients fitted to the Teng et al. (2000) step velocity data listed in Table 2.2. The calcite precipitation rate data of Nilsson and Sternbeck (1999), Inskeep and Bloom (1985), Teng et al. (2000) were performed with a background electrolyte concentration > 0.1 M and pH > 7.8. These rate data are consistent with the Zuddas and Mucci (1994) experiments performed with a P_{CO_2} of 0.02 and a pH ~ 7, which is sufficiently low to facilitate equilibration between dissolved inorganic carbon species in solution (Fig. 1.7). All of these experiments converge to a first order rate dependence on oversaturation. Other experiments consistent with this model but offset to lower growth rates are listed in Table 1.1, along with partial reaction orders of literature rate data for experiments that are inconsistent with this model. Partial reaction order was calculated from the slope of Log(Rate) - Log(Ω) curves.

1.8 Conclusion

The mechanism of calcite precipitation from aqueous solution has long been inferred from the dependence of growth kinetics on solution parameters, primarily supersaturation. Varied experimental methodologies have led to a wide array of mechanistic interpretations for calcite growth. In this chapter, we presented a microscopic growth model based on growth mechanisms observed *in situ* - kink and step propagation - that is consistent with a subset of calcite growth rate data (Figure 1.7).

The net rate of AB mineral growth is controlled by the rates of attachment to and detachment from kink sites along step edges at the mineral surface. For sparingly soluble AB minerals such as calcite, precipitation kinetics are limited by the rate of kink formation via 1D nucleation. Using the CPC model framework, the net rates of A and B ion attachment may be separately quantified in terms of elementary attachment and detachment reactions occurring at kink sites. I demonstrated that the exchange fluxes of A and B ions at the mineral aqueous interface depend explicitly on the individual activities of A and B in solution, and not just on overall supersaturation. The rate of ion detachment relative to the net growth rate governs the degree of isotopic equilibration between the mineral and solution (DePaolo, 2011), so this model may be used to quantify surface controls on isotopic and trace element incorporation in calcite.

Chapter 2

Kinetic isotope fractionation during calcite precipitation

2.1 Introduction

Advances in the measurement of stable isotope variations of cations such as Ca, Fe, and Mg (Johnson et al., 2004) provide novel perspectives on mineral formation processes relative to the isotopes of more commonly studied elements like C, O, H, S, and N. Calcium, which is ubiquitous in most surface environments, plays a major role in biogenic and inorganic processes central to the global carbon cycle (Gussone et al., 2003b; Chang et al., 2004a; DePaolo, 2004; Fantle and DePaolo, 2005). Precipitation of calcium carbonate minerals from aqueous solutions produces 0.5 ‰ to 2 ‰ fractionation of $^{44}Ca/^{40}Ca$ between solid and aqueous phase (i.e. Tang et al., 2008a; Lemarchand et al., 2004; DePaolo, 2004; Skulan and DePaolo, 1999; Gussone et al., 2003a; Reynard et al., 2011). Light calcium isotopes are preferentially incorporated into the solid phase due to the relatively sluggish reaction kinetics of heavy isotopes.

Although kinetic, mass-dependent fractionation of stable isotopes and disequilibrium trace element partitioning are widely observed during mineral growth (Paquette and Reeder, 1995; Watson, 1996; Fantle and DePaolo, 2007; Tang et al., 2008b,a), no existing theory links microscopic mineral growth models with macroscopic models of trace element and isotope partitioning during precipitation. In this chapter, a self-consistent model for calcite growth based on CPC theory is derived that predicts isotopic fractionation as a function of growth solution composition. The model is applicable to any sparingly soluble di-molecular salt, and will be extended in chapter 5 to incorporate the nonlinear effects of trace element incorporation on both growth rate and trace element partitioning.

2.2 Models of isotope partitioning during calcite precipitation

Isotopic and trace element partitioning during mineral growth have been shown to be kinetically controlled, (e.g. Young et al., 2002), and numerous models have been invoked to describe these observations. The mechanistic underpinning of these models varies widely, from processes such as solid state diffusion (Watson, 1996), overprinting of equilibrium partitioning between solvated and mineral ions by kinetic effects (Lemarchand et al., 2004), to kinetic separation due to macroscopic ion fluxes in the mineral surface boundary layer (Fantle and DePaolo, 2007; DePaolo, 2011). None of these models is directly tied to the mechanistic models for mineral growth based on creation-propagation-collision (CPC) theory (chapter 1). Though a dependence of trace element (Nehrke et al., 2007) and isotope (Spero et al., 1997, chapter 4) partitioning on solution stoichiometry (i.e. the Ca^{2+} to CO_3^{2-} ratio in solution) has been observed, these observations have not been modeled.

Significant variability in the calcium isotope composition of terrestrial and solar system materials including calcite has been observed and attributed to mass-dependent isotope fractionation (Russell et al., 1978; Simon and DePaolo, 2010). Biogenic fractionation during $CaCO_3$ mineralization is an important source of variation: organisms fractionate calcium isotopes during biomineralization of shell (Skulan et al., 1997; Gussone et al., 2003a; Chang et al., 2004b; DePaolo, 2004; Gussone et al., 2004; Nägler, 2000; Böhm et al., 2006; Hippler et al., 2006, 2009) and bone (Skulan and DePaolo, 1999; DePaolo, 2004; Komiya et al., 2008; Reynard et al., 2010). In all cases, the solid carbonate phase is enriched in the light isotope, typically by $\sim 1 - 2‰$ relative to the growth medium, strongly suggesting a kinetic effect. Isotopic fractionation of similar magnitude has been generated by inorganic precipitation of calcium carbonate in the laboratory (Gussone et al., 2003a; Lemarchand et al., 2004; Gussone et al., 2005; Tang et al., 2008a; Reynard et al., 2011, chapter 3). Kinetic fractionation of oxygen isotopes has also been observed during calcite growth (Dietzel et al., 2009; Gabitov et al., 2011). Controlled growth experiments suggest that calcite growth rate is correlated with the magnitude of isotopic fractionation (Lemarchand et al., 2004; Tang et al., 2008a), and various mechanisms have been proposed to explain these observations.

DePaolo (2011) developed a model that describes the calcium isotope fractionation and strontium partitioning observed by Tang et al. (2008 a & b) during inorganic calcite precipitation experiments. This model posits that the relative attachment and detachment fluxes of ions to the growing mineral surface controls the degree to which a mineral isotopic composition reflects equilibrium (α_{eq}) or kinetic (α_f) fractionation endmembers. When the mineral growth rate exceeds the rate of exchange of ions between mineral and aqueous solution, the isotopic composition tends towards α_f. The equilibrium fractionation is expressed only when growth rate is much smaller than the exchange rate. This model does not account explicitly for the effects of changes to solution composition – other than oversaturation – on isotope fractionation, nor does it take into account the dependence on oversaturation of the densities of microscopic features at which attachment and detachment occur. However, the theory is

consistent with forward and reverse fluxes of ions governing mineral growth in microscopic models of ionic crystal growth (Zhang and Nancollas, 1998) and accounts for much of the available laboratory data on Ca isotope and Sr/Ca fractionation.

The microscopic description of calcite precipitation kinetics provided by CPC theory reduces the problem of surface controlled mineral growth to its rate limiting reactions: kink creation via 1D nucleation, kink propagation via ion attachment to and detachment from kink sites, and kink loss via collision. Because this model explicitly accounts for the net reaction rate of each ionic constituent, it may readily be extended to model the incorporation of isotopes and trace elements in carbonates.

The flux to and from a mineral surface of isotopes substituting for a given constituent ion will depend on the relative abundance of the ion in solution as well as the activation energy barrier for isotope or trace element addition and removal. Heavy isotopes tend to have higher kinetic activation energy barriers for chemical reactions, so reaction kinetics are expected to be slightly more sluggish. Trace elements of the same charge fit more or less favorably into the crystal lattice depending on ion size and site structure, affecting the kinetics of trace element incorporation and the overall mineral solubility. Isotope substitution into the mineral lattice should not significantly affect the rate coefficients of ion attachment or detachment, so we assume that it has no effect on mineral growth kinetics. Using the formulations for growth rate during dislocation- and 2D nucleation-driven growth, we derive an analytical expression for isotopic partitioning as a function of solution oversaturation and ion activity ratio. This expression applies to both 2D nucleation and dislocation driven-step growth mechanisms, because ion exchange occurs primarily at kink sites along the step edge in both cases.

As with growth rate, the ratio of Ca^{2+} to CO_3^{2-} ions in solution (solution stoichiometry) should affect the ability of the mineral surface to exchange ions with solution. In a calcium rich solution, back reaction of Ca ions at the mineral surface will be promoted, because attachment of carbonate ions becomes the growth rate limiting step. Such exchange must facilitate calcium isotopic equilibration of the mineral surface with aqueous solution, driving the solid away from the kinetic endmember composition.

Using the framework developed by DePaolo (2011), we derive a general analytical expression for isotopic fractionation during AB mineral growth as a function of oversaturation and solution stoichiometry. The model accurately describes mass-dependent fractionation of Ca isotopes during calcite growth. In the previous chapter, growth rate was considered in two cases: dislocation-driven (spiral) growth, and 2D nucleation-driven growth. The process of ion attachment and detachment at kinks along step edges governing ion incorporation along steps is the same in both cases. Isotopic fractionation during precipitation, α_p, is derived from an expression for step velocity which applies to both spiral and 2D nucleation-driven growth, so a single expression for α_p is needed. Trace element incorporation affects both surface kink density and growth kinetics, whereas isotopic exchange with solution does not. Trace element incorporation is addressed in detail in chapter 5

We posit that 2D nucleation can explain the high order dependence of growth rate on oversaturation observed in inorganic calcite growth experiments reported by Tang et al. (2008a) , although their experimental design may have contributed significant error to their

estimation of solution supersaturation. We also show that our expression for isotope fractionation is consistent with reported $\Delta^{44/40}$Ca values. As a consequence of the microscopic nature of this derivation, we also conclude that our model is not valid for describing growth from highly oversaturated solutions, where calcite grows by the formation of amorphous calcium carbonate (ACC), which then reorganizes to form a crystalline phase. Formation of ACC may be invoked to explain the rate dependence of Ca isotope fractionation during calcium carbonate growth obtained by Lemarchand et al. (2004) and Gussone et al. (2003), which has an inverse growth rate dependence compared with the Tang et al. (2008a) data modeled here. The growth solutions used by Gussone et al. (2003) and Lemarchand et al., (2004) are all significantly oversaturated with respect to ACC (solubility reported in Clarkson et al. (1992)), while none of the Tang et al. (2008a) solution compositions exceed this solubility threshold. The results of the former two groups are likely due to the mixing of calcite formed via the ACC pathway and that formed by ion-by-ion addition.

2.3 Oversaturation and solution stoichiometry dependent isotope fractionation

During surface-controlled mineral growth, fractionation of rare isotopes of A (defined A' here) may be determined from the relative rates of A' incorporation and removal at kink sites during growth. The partitioning associated with each step and with the overall reaction may be expressed:

$$\alpha_{j-i} = \frac{r_j}{r_i} = \frac{R^j_{A'}}{R^j_A}\frac{1}{r_i}, \tag{2.1}$$

where $i \rightarrow j$ is the forward reaction (e.g. attachment, detachment, or net precipitation), $R^j_{A'}$ and R^j_A are the net rates of A' and A reaction respectively, r_j is the (A'):(A) ratio of the product, and r_i is the (A'):(A) ratio of the reactant.

During step propagation, the fractionation factor of isotopes of A during attachment is

$$\alpha_f = \frac{k_{A'}(A')}{k_A(A)}\frac{1}{r_s} = \frac{k_{A'}}{k_A}, \tag{2.2}$$

where $r_s = \frac{(A')}{(A)}$ in solution. The fractionation factor during detachment is

$$\alpha_b = \frac{\nu_{A'}P_{A'}}{\nu_A P_A}\frac{1}{r_x}, \tag{2.3}$$

where r_x is the ratio of heavy to light isotopes incorporated into the crystal bulk. At steady state, the composition of the mineral bulk with N_i moles of i is constant,

$$\frac{dr_x}{dt} = \frac{1}{N_A}\left(\frac{dN_{A'}}{dt} - r_x\frac{dN_A}{dt}\right) = 0. \tag{2.4}$$

The rate of i addition or removal, $dN_i/dt = R^i_{net}$, and $r_x = R^{A'}_{net}/R^A_{net}$ (DePaolo, 2011). To maintain a steady state isotopic composition, the net rate of A and A' addition to the surface must equal the net rate of A and A' addition to the bulk, so r_x is equal to the the net incorporation of A' by B divided by the net incorporation of A by B,

$$r_x = \frac{k_B(B)P_{A'} - \nu_B P_B P_{B-A'}}{k_B(B)P_A - \nu_B P_B P_{B-A}} = \frac{P_{A'}}{P_A}, \tag{2.5}$$

where P_{B-i} is the probability that a given B site is adjacent to an i site. The relation $r_x = P_{A'}/P_A$ holds as long as the attachment and detachment of B ions to and from A sites have the same coefficients, k_B and ν_B, as to and from A' sites, which is an adequate approximation for isotopic substitution but not for trace element substitution. Invoking this assumption, kink probabilities cancel from expression 2.3, and isotope fractionation during detachment becomes

$$\alpha_b = \frac{\nu_{A'}}{\nu_A}. \tag{2.6}$$

The fractionation factor of A at equilibrium is a function of the attachment and detachment fractionation factors:

$$\alpha_{eq} = \frac{\alpha_f}{\alpha_b} = \frac{k_{A'}\nu_A}{k_A\nu_{A'}}. \tag{2.7}$$

Thus,

$$\nu_{A'} = \frac{\alpha_f}{\alpha_{eq}}\nu_A. \tag{2.8}$$

The total fractionation of A isotopes during precipitation is defined as:

$$\alpha_p = \frac{r_x}{r_s}, \tag{2.9}$$

which leads to the following expression:

$$\alpha_p = \frac{R^{net}_{A'}}{r_s R^{net}_A} = \frac{R^f_{A'} - R^b_{A'}}{r_s(R^f_A - R^b_A)} = \frac{u_{A'}}{r_s u_A}. \tag{2.10}$$

During growth along the step, the rate of A' attachment to the mineral surface may be expressed as:

$$R^f_{A'} = \frac{\rho k_{A'}(A')P_B hbd}{y_0}. \tag{2.11}$$

Similarly, the detachment flux becomes:

$$R^b_{A'} = \frac{\rho \nu_{A'} P_{A'} hbd}{y_0}. \tag{2.12}$$

By substitution, Eq. 2.9 becomes:

$$\alpha_p = \frac{\alpha_f k_A(A)P_B}{k_A(A)P_B + \nu_A P_A\left(\frac{\alpha_f}{\alpha_{eq}} - 1\right)}. \tag{2.13}$$

This expression reduces to the DePaolo (2011) macroscopic model of kinetic isotope fractionation during surface controlled mineral precipitation:

$$\alpha_p = \frac{\alpha_f}{1 + \frac{R_A^b}{R_A^f}\left(\frac{\alpha_f}{\alpha_{eq}} - 1\right)}, \tag{2.14}$$

where R_b/R_f may now be expressed explicitly in terms of S and r via Eq. 1.28. Hence, we have arrived at a microscopic description of isotopic partitioning during crystal growth from aqueous solution that takes account of both solution oversaturation and solution stoichiometry.

2.4 Model application

Calcium isotope fractionation during calcite growth

The theory derived thus far will now be applied to calcium isotope fractionation during calcite precipitation, where Ca^{2+} and CO_3^{2-} substitute for A and B, and heavy and light isotopes ^{44}Ca and ^{40}Ca replace A' and A respectively. Growth rate and the kinetic isotopic fractionation factor are calculated for a given solution composition based on Eqs. 1.26 and 2.13 respectively.

No coherent set of calcite precipitation experiments provides sufficient information to fit all parameters involved in this model. Free energy parameters α and γ and attachment rate constants likely depend on solution compositional variables such as ionic strength, which are not directly accounted for, so values obtained under one set of experimental conditions may not be generally applicable. An attempt to fit the dependence of calcium isotope fractionation on calcite growth kinetics is presented here to demonstrate model implementation, and to reveal gaps in experimental data. We do not account for surface speciation of carbonate, which is addressed in Wolthers et al. (2012). As most experimental data modeled here were obtained within a narrow pH range (8.3-9), and the rate coefficient of cation attachment to both dominant types of CO_3^{2-} surface sites (protonated and deprotonated) may be assumed to be approximately equal (Wolthers et al., 2012), surface carbonate speciation should have little effect on kinetic isotope fractionation of calcium or substituting trace elements or isotopes.

Multiple parameters, including the calcite solubility (K_{sp}), density (d), kink height (h), depth (b) and molecular spacing (a), and kink formation energy (ϵ) were taken from the literature (Table 2.1). Reasonable values for kink formation energy and step edge free energy per unit step height may be derived from Wolthers et al. (2012). We expect these values to vary somewhat with solution composition and experimental setup. The step kinetic coefficient for 2D nucleation driven growth, β_{st}, was calculated from Eq. 1.32, with step velocity, v_{st}, determined from Eqs. 1.26 and 1.27. Parameters not available in the literature, or those with literature values inconsistent with observed precipitation rates were fitted. The following procedure was used to fit the experimental growth rate and isotopic data:

1. Fit detachment and attachment rate coefficients ν and k to step velocity data, calculate kink density and propagation rate using Eqs. 1.18 & 1.17, calculate step velocity using Eq. 1.27, and calculate β_{st} using Eq. 1.32;

2. Fit α_{eq} and α_f to isotopic data, calculate kink site probabilities using Eqs. 1.12 & 1.13, and calculate α_p using Eq. 2.13;

3. Fit step edge free energy per unit step height (α) to spiral growth rate using Eq. 1.26; and

4. Fit edge free energy of the critical nucleus (γ) to rate data, calculate 2D nucleation frequency using Eq. 1.31 & 1.33, and finally calculate the 2D nucleation-driven growth rate using Eq. 1.30.

For each step of fitting, constraints on fitted parameters were obtained from the literature where available. The parameters fitted in step (1) can be evaluated from the solution stoichiometry-dependent step velocities of Davis (2008), Perdikouri et al. (2009), and Larsen et al. (2010) (Table 2.2; Fig. 2.1). A similar relationship between step velocity and solution stoichiometry was observed by Stack & Grantham (2010). However, we do not attempt to fit their data here, because their observed step velocities suggest that calcite becomes undersaturated at very high and very low Ca^{2+}:CO_3^{2-}. This phenomenon has not been observed elsewhere, and could be attributed to the presence of impurities or to the evolution in solution composition prior to entering the fluid cell. In the absence of varied solution stoichiometry data, k and ν parameters were fitted from step velocity as a function of supersaturation data (e.g. Teng et al., 2000).

To fit attachment and detachment rate coefficients, we first assumed that ν_A=ν_B=ν (because the same bond is being broken) and k_A=k_B=k (because ion attachment rate is limited by calcium dehydration either at the surface or in solution). Step velocities were fitted by adjusting a single parameter, k, and solving ν=$\sqrt{k^2 K_{sp}}$ from Eq. 1.22. Step velocities which were maximized at Ca^{2+}:$CO_3^{2-} \neq 1$ require that $\nu_A \neq \nu_B$ and/or $k_A \neq k_B$. These were fitted by slightly adjusting ν_B and k_B, using Eq. 1.22 as a constraint. Final k and ν values obtained for Teng et al., (2000) Larsen et al. (2010), Perdikouri et al. (2009), and Davis (2008) acute and obtuse step velocities were in reasonable agreement (Table 2.2).

For step (2) of the fitting procedure, we used the Fantle & DePaolo (2007) estimate of $\alpha_{eq} \sim 1.0000 \pm 0.0001$, to constrain our fitted value (0.9998). We hypothesize that α_f

Table 2.1: Constants applied in all fits to experimental data displayed in Fig. 2.2. Sources for these constants include Larsen et al. (2010) (ϵ) and Teng et al. (1998) (a, b, h, and K_{sp}).

ϵ/kT	a = 2b (m)	h (m)	d (mol/m^3)	K_{sp}
2.82	$6.4e-10$	$3.1e-10$	27100	$10^{-8.54}$

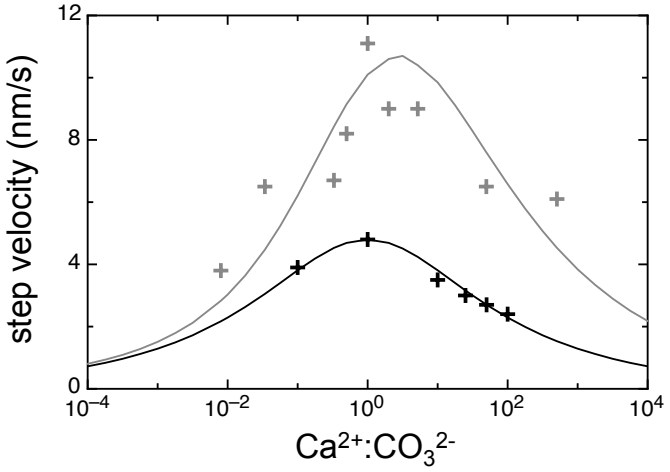

Figure 2.1: Larsen et al. (2010, black) and Davis (2008, grey) obtuse step velocities plotted as a function of solution stoichiometry (plus symbols) using Eq. 1.27. The model fits to these data are plotted as lines, and the corresponding fitted parameters are listed in Table 2.2.

depends on the relative rates of ^{44}Ca and ^{40}Ca ion dehydration. Ongoing work using MD simulations to derive the relative cation desolvation frequencies suggests that the magnitude of these effects could be appropriate to explain the laboratory data (Hofmann et al., 2011). However, for our purposes, $\alpha_f = k_{A'}/k_A$ is fitted without constraint. To determine step edge free energy per unit step height in (3), we use values equal or similar to the value fitted by Teng et al. (2000): $\alpha \sim 1.41$ J/m^2. This parameter exerts a strong control on spiral growth rate. Increasing α shifts the calculated spiral growth rate to lower values (Fig. 1.6). For the final fitting step (4), γ was adjusted to fit the observed dependence of growth rate on supersaturation, because a 2D nucleation-driven growth mechanism likely dominates over the entire growth rate range reported by Tang et al. (2008a). In theory, edge free energy of the critical nucleus should be close to step edge free energy per unit step height multiplied by step height ($\alpha \times h$), and the fitted value is consistent with this constraint.

To illustrate the effects of varying individual parameters on modeling experimental precipitation rate and isotopic data, we present three fits (A, B and C; Table 2.3; Fig. 2.2) to the rate dependence of calcium isotope fractionation reported by Tang et al. (2008a) . Fits A and B use the attachment and detachment rate constants fitted to Larsen et al. (2010) obtuse step velocities, while fit C uses exchange coefficients fitted to Davis (2010) obtuse step speeds (Table 2.2). The kinetic endmember isotopic fractionation factor depends exclusively on exchange coefficients, so A and B use the same fitted value for $\alpha_f = 0.9920$, while the value used in fit C substantially differs $\alpha_f = 0.9963$. Obtuse step velocities were fitted here, because at high Ca^{2+}:CO_3^{2-}, obtuse steps tend to propagate much faster than acute steps

Table 2.2: Attachment and detachment frequency rate constants fitted to reported obtuse (+) and acute (−) step speed data from Teng et al. (2000), Davis (2008), Perdikouri et al. (2009), and Larsen et al. (2010) and corresponding oversaturations (S). Kinetic coefficients fitted to Larsen (+) obtuse step velocities were used in fits A and B, and coefficients fitted to Davis (+) step velocities were used in fit C.

Constant	Davis (+)	Davis (−)	Larsen (+)	Larsen (−)	Perdikouri	Teng (+)
$\nu_{Ca^{2+}}$ (s^{-1})	2.39e1	1.60e2	7.89e1	6.44e2	5.87e1	6.33e2
$\nu_{CO_3^{2-}}$ (s^{-1})	1.39e2	8.25e0	7.89e1	1.82e1	3.95e1	6.33e2
$k_{Ca^{2+}}$ ($s^{-1}M^{-1}$)	9.24e5	6.75e5	1.47e6	3.58e6	3.11e5	1.10e7
$k_{CO_3^{2-}}$ ($s^{-1}M^{-1}$)	1.24e6	6.75e5	1.47e6	1.13e6	2.58e6	1.10e7
S	12	12	4.6	4.6	6.3	

and should therefore dominate the isotopic signature. Because isotopic compositions specific to the vicinal faces of calcite are not available, attempting to fit the data using an expression for isotope fractionation incorporating both step types (Appendix B) would introduce further parameters without significantly promoting our understanding of the system.

Using fit A parameters, we found that it is not possible to generate growth rates as low as those observed by Tang et al. (2008a) at the lowest supersaturations via the spiral growth mechanism. To correct this discrepancy, we adjusted step edge free energy per unit step height α in fits B and C to a value sufficiently high such that modeled spiral growth rates do not exceed the slowest growth rates reported by Tang et al. (2008a) at low oversaturation (Fig. 2.2b; Table 2.3). The value for edge work calculated based on this fitted α exceeds the range of values presented by Wolthers et al. (2012) by a factor of ~ 2. The disagreement in fitted growth rate could arise from erroneous estimates of oversaturation due to sluggish CO_2 hydration in the Tang et al. (2008a) experimental setup.

Table 2.3: Fitted endmember fractionation factor, step edge free energy per unit step height and edge free energy parameters applied in fits A, B and C displayed in Fig. 2.2.

Fit	rate constants	α_f	α_{eq}	α (J/m^2)	γ (J/m)
A	Larsen (+)	0.9920	0.9998	1.41	1.49e-10
B	Larsen (+)	0.9920	0.9998	3.00	1.49e-10
C	Davis (+)	0.9963	0.9998	3.00	1.49e-10

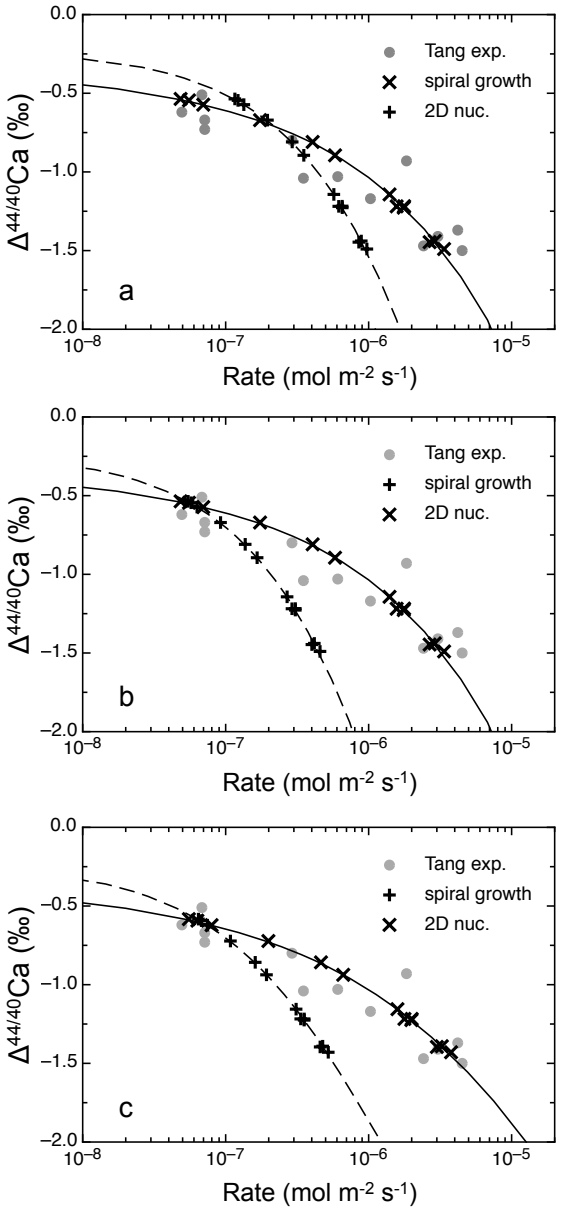

Figure 2.2: Dislocation- and 2D nucleation driven step growth models using parameters from fits A (a), B (b) and C (c) compared with Tang et al. (2008a) experimental data. Rate model fits assuming a spiral growth mechanism are shown as dashed lines, while fits assuming 2D nucleation-driven growth are shown as solid black lines. The experiment-specific modeled data points are shown as black symbols. Tang et al. (2008a) experimental rate vs. $\Delta^{44/40}$Ca data are shown as grey circles and are the same in (a-c).

Carbon and oxygen isotope fractionation during calcite growth

As presented, the model should be applicable to characterizing isotopic fractionation during the attachment of anions to the mineral surface. In the case of calcite, the proposed rate limiting mechanism for ion attachment to kink sites on the surface is the dehydration of the cation. Thus, any difference in rates of CO_3^{2-} dehydration caused by mass differences should be overprinted by the rates of calcium kink dehydration, so the kinetic endmember fractionation factor for both C and O is expected to equal the equilibrium fractionation factor between carbonate adsorbed to calcite as an outer-sphere complex and aqueous CO_3^{2-}. Rate dependent fractionation may still arise if the detachment of carbonate containing heavy C or O is slower than that of carbonate containing light C or O. Inorganic calcite precipitation experiments have yielded conflicting results concerning the growth rate dependence of oxygen isotope fractionation, with some groups observing no dependence (Romanek et al., 1992; Kim and O'Neil, 1997) and others observing a significant growth rate effect (Dietzel et al., 2009; Gabitov et al., 2011). At present, it is unclear whether the carbonate ion mass has any effect on the frequency of detachment. Studies in which growth-rate dependent O isotope fractionation is evident (e.g. Dietzel et al., 2009) must be scrutinized to rule out the effects of isotopic disequilibrium between carbonate species in solution. Solution pH has a large effect on carbonate aqueous speciation, so C and O isotope discrimination between species (e.g. Beck et al., 2005) may be invoked to explain the dependence of C and O isotope fractionation on carbonate concentration during calcite precipitation (Spero et al., 1997). We do not attempt to fit this pH dependence here, because this requires incorporation of the equations derived by Wolthers et al. (2012), which is beyond the scope of this thesis.

Amorphous precursor formation

Tang et al. (2008a) performed precipitation experiments at saturation indices well below the solubility of amorphous calcium carbonate (ACC), so calcite growth in this system likely occurs primarily by ion-by-ion addition and is therefore adequate for comparison with this model. Based on carbonate concentrations and calcium activities calculated using PHREEQc (Parkhurst and Appelo, 1999), the experiments of Lemarchand et al. (2004) and Gussone et al. (2003) were performed at solution supersaturations exceeding the solubility of an amorphous precursor phase (IAP $> 5.9 \times 10^{-7}$) (Clarkson et al., 1992), so they are not expected to be consistent with this model. The observation that the latter two sets of experiments exceeded ACC solubility likely explains why these groups obtain a stable Ca fractionation rate dependence inverse of that reported by Tang et al. (2008a) .

Implications of solution stoichiometry-dependent isotope fractionation

A key prediction of this model is that the isotopic fractionation factor (and the trace element partition coefficient) should depend on solution stoichiometry as well as on growth rate. We hypothesize that at very high Ca^{2+}:CO_3^{2-} ion activity ratios, isotope fractionation will approach the equilibrium limit, because back exchange with the solution is encouraged

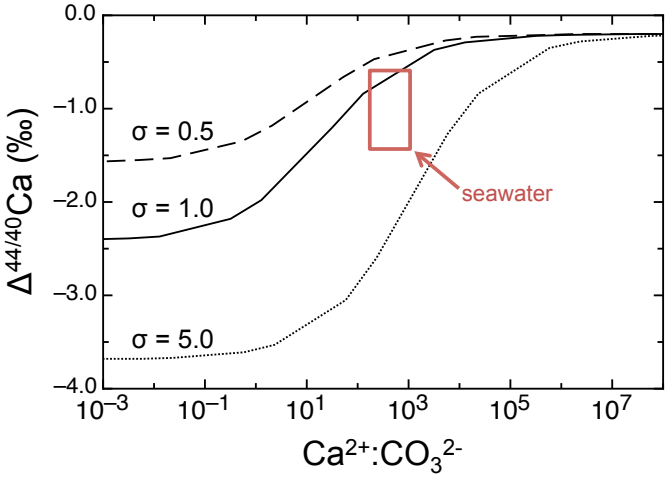

Figure 2.3: Predicted fractionation dependence on solution stoichiometry at varied solution supersaturations calculated from Eq. 2.13, assuming surface reaction controlled growth using the k and ν values of fits A and B. Rectangle shows approximate expected Ca isotope fractionations for calcite precipitated from surface seawater, or slightly more oversaturated seawater-like solutions.

by the abundance of calcium surface sites (high $P_{Ca^{2+}}$) and the low $[CO_3^{2-}]$ in solution (Fig. 2.3). Conversely at very low Ca^{2+}:CO_3^{2-} ion activity ratios, fractionation should approach the kinetic limit. Qualitatively, the effects of varying oversaturation and solution stoichiometry on fractionation factor can be seen in Fig. 2.3.

Calcite precipitation from seawater

Using the model coefficients from fits A and B, calcite precipitation from average seawater ($[Ca^{2+}]$∼2e-3 and $[CO_3^{2-}]$∼4e-6)(Berner, 1965; Russell et al., 2004) is expected to have $\Delta^{44/40}$Ca= 0.60‰, while fit C gives $\Delta^{44/40}$Ca= 0.70‰, which are slightly smaller than values typically inferred for marine $CaCO_3$ calcium isotopic fractionation, (e.g. Gussone et al., 2004; Fantle and DePaolo, 2007; Nielsen et al., 2011). Biomineralizing organisms increase the oversaturation of seawater to promote carbonate precipitation by active transport of calcium ions through tissue (Böhm et al., 2006) or by modification of seawater pH (Erez, 2003). The difference between observed seawater-biomineral calcium isotope fractionation ($\sim$ 1.3‰) and our expected value ($\sim$ 0.7‰) may be explained by the biological enhancement of oversaturation, and the corresponding increase in mineralization rate.

Seawater has an average Ca^{2+}:CO_3^{2-} activity ratio of $\sim$ 450, so inorganic calcium carbonate precipitation from seawater is not expected to reflect the kinetic endmember of isotope fractionation. The carbonate ion concentration and therefore solution stoichiometry is highly variable in the ocean, both geographically (Lea et al., 1999) and temporally (Suzuki et al.,

1995) due to changes in seawater pH. Diurnal shifts as large as 0.7 pH units have been observed in seawater adjacent to coral reefs (Suzuki et al., 1995; Suzuku and Kawahata, 2004). Such significant changes in seawater r_a may explain observed fine-scale variability in coralline $CaCO_3$ trace element composition (Meibom et al., 2008). Ocean acidification due to the loading of anthropogenic CO_2 in the atmosphere will decrease $[CO_3^{2-}]$ relative to $[Ca^{2+}]$, altering carbonate mineral growth kinetics and corresponding mineral composition. The response of biomineralizing organisms to ocean acidification may be monitored by investigating changes in biomineral isotopic composition.

2.5 Conclusion

The addition of ions to and removal of ions from the mineral surface controls crystal isotopic composition during growth. By identifying this mechanism and incorporating compositional variability into preexisting rate relations based on this mechanism, we have derived a general, self-consistent model describing precipitation rate and isotopic composition. This model was applied to the calcite growth experiments of Tang et al. (2008a) and will be extended in chapter 5 to model precipitation rate, taking the effects of trace element substitution on growth kinetics into account. The potential applications of this model are extensive. Given adequate constraints on model parameters, precipitation rate variability may be predicted as a function of solution oversaturation and stoichiometry. This may be useful in the context of reactive transport modeling or when considering the effects of ocean acidification on paleoproxy isotope partitioning into $CaCO_3$. Limited data are available to resolve model parameters, so further experimental data relating solution composition to growth kinetics are necessary.

This model identifies key variables controlling trace element and isotope partitioning into sparingly soluble AB minerals such as calcite. Experimental data required for fitting all model parameters include measurement of:

1. step velocity as a function of S and r_a for both obtuse and acute steps;
2. terrace width as a function of S and r_a for dislocation-driven growth;
3. threshold supersaturation for 2D nucleation;
4. nucleation frequency (I) as a function of S; and
5. isotopic and trace element composition of calcite as a function of S and r_a for both obtuse and acute steps.

To ensure that the hypothesized growth mechanisms are relevant to analyzed calcites, growth must be observed and isotopic composition quantified on samples prepared in the same way. In the following chapter, we present a methodology that allows measurement of $\delta^{44/40}$Ca and *in situ* observation of growth in identical samples.

Chapter 3

Supersaturation dependence of $\Delta^{44/40}$Ca in calcite overgrowth experiments

3.1 Introduction

The effect of solution composition on growth rate and calcium isotope fractionation during calcite precipitation is difficult to determine using standard reactor experimental apparatus, because growth kinetics and growth features cannot be directly observed. Often, the composition of the growth solution evolves during the course of an experiment, so bulk digestions of experimentally precipitated carbonate yield solution-averaged isotopic fractionation factors (e.g. Tang et al., 2008a). Experimental studies linking calcium isotopic composition to calcite precipitation rate have involved nucleation of calcite seeds prior to crystal growth (Lemarchand et al., 2004; Tang et al., 2008a), and nucleation could contribute an isotopic signature that is not due to surface controlled growth kinetics. Relying upon nucleation further results in a range of particle sizes growing at any given time, contributing significant error to the determination of surface area normalized growth rates. Alternative experimental methodologies for linking calcium isotope fractionation to solution composition must be developed to avoid these potential experimental artifacts.

Investigations of the microscopic mechanisms of mineral growth kinetics have long relied upon atomic force microscope (AFM) *in situ* precipitation experiments. These experiments utilize a fluid cell through which fresh solution is pumped at a constant rate, keeping solution composition constant. The fluid cell is placed over a cleaved rhomb of the mineral of interest, and precipitation occurs directly on the mineral surface. No heterogeneous nucleation (nucleation of calcite on a different material) is required prior to mineral precipitation, and propagation of active growth features including kinks and steps may be directly observed and used to calculate the surface normal precipitation rate.

To determine the dependence of calcium isotope fractionation on aqueous solution com-

position (supersaturation and solution stoichiometry), I performed a series of precipitation experiments using a fluid cell apparatus and analyzed the $\delta^{44/40}$Ca of overgrowth material using secondary ion mass spectrometry (SIMS). For varied supersaturation experiments, I determined the calcium isotopic fractionation factor as a function of solution composition. Experiments designed to determine the solution stoichiometry dependence of $\Delta^{44/40}$Ca yielded overgrowth textures that were not possible to analyze reliably via SIMS due to changes in instrumental mass fractionation (IMF) with texture, so these experiments should be repeated in the future.

3.2 Fluid cell calcite precipitation experiments

Calcite overgrowth precipitation experiments were performed in a fluid cell apparatus using stoichiometric solutions of varied supersaturation and non-stoichiometric solutions at fixed supersaturation. Overgrowths greater that 2 μm in thickness were required for SIMS analysis of $\delta^{44/40}$Ca, so the required experimental durations were up to 16 hours. Overgrowth experiments for SIMS analysis were performed out of the AFM to generate sufficient amounts of calcite. Step velocities and terrace widths for several fluid compositions identical to corresponding overgrowth experiments were measured via *in situ* AFM using the same experimental setup.

Flow cell experimental setup

A fluid cell apparatus was used to perform calcite precipitation experiments both in and out of the AFM. Two large 140 mL syringes were separately filled with calcium and carbonate solutions. These syringes were placed on a syringe pump adjusted to a total flow rate of 0.8 mL/min (0.4 mL/min/solution). Both solutions were connected via teflon tubing to an inline magnetic stir apparatus, which ensured that the solutions were well-mixed prior to entering the fluid cell. Several feet of teflon tubing were used to connect the stir cell to the fluid cell to ensure that the mixed fluids were well equilibrated and to minimize the noise created by the syringe pump during AFM imaging. A photograph of the experimental setup outside of the AFM is shown in Fig. 3.1. The fluid cell consists of a small circular reservoir with inlet and outlet openings. To seal the cell, an o-ring is placed in a groove around the reservoir, and the entire cell is placed o-ring down on the cleaved calcite surface. A small amount of pressure is applied to the sample either using the motorized stage in the AFM or simply using tape when performing long experiments out of the AFM.

Growth solution composition

Experimental growth solutions varied in supersaturation from $\sigma \sim 1$ to ~ 5 and in calcium to carbonate ion activity ratio from ~ 0.05 to ~ 20 (Table 3.1). Calcium solutions were prepared from high purity Ca stock, and carbonate solutions were prepared from solid

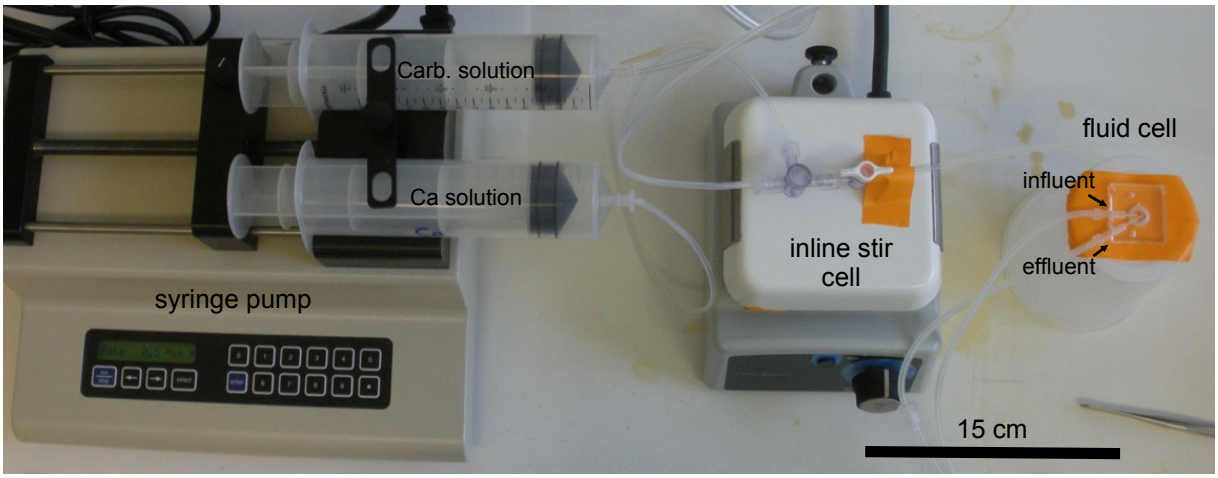

Figure 3.1: Experimental setup for flow experiments. Separate syringes containing calcium and carbonate solutions are pumped into an inline magnetic stir cell where they are thoroughly mixed. The mixed fluid is pumped into the fluid cell, where it flows over a cleaved calcite face.

$NaHCO_3$ (99.998%). The calcium stock solution was composed of anhydrous $CaCl_2$ (99.99%) dissolved in DDI water yielding a calcium concentration of 0.39 M and an isotopic composition of -0.81(20) ‰ BSE measured via TIMS (see methods below). For growth solutions, both reagents were separately dissolved in double deionized (18.2 MΩ) water. Ultrapure KCl was added to all solutions as a background electrolyte at a concentration of 0.1 M. All calcium and carbonate solutions were separately pH adjusted to 8.5 ± 0.1, and pH measured in the fluid cell effluent was within error of the influent. High purity reagents were used in all experiments to prevent kink blocking by impurities. The geochemical modeling software PHREEQc was used to calculate the speciation of aqueous solutions and to determine reagent concentrations required for the supersaturations and solution stoichiometries of interest.

Flow rate optimization

The flow rate of aqueous solution through the fluid cell may affect the kinetics of calcite growth, so flow speed should be optimized prior to performing experiments. If the flow rate is too slow, heterogeneous nucleation of calcite will occur prior to fluid entry into the fluid cell, drawing down fluid supersaturation. If the flow rate is too fast, the mixed calcium and carbonate fluids will not be equilibrated prior to entering the cell. At intermediate flow rates, step velocity should level out and become relatively insensitive to small changes in flow.

We imaged calcite step velocity as a function of flow rate varied from 0.2 to 1.4 mL/min at fixed supersaturation. As expected, step velocity increased with flow rate at low flow rates

Table 3.1: Growth solution compositions, isotopic compositions and measured precipitation rates of calcite overgrowth experiments. All growth solutions were adjusted to pH 8.5 using NaOH and contained 0.1 M KCl. Step velocity and terrace width 1 s.d. uncertainties (listed in parentheses) were calculated from repeated AFM scans.

Exp.	$[CaCl_2]$	$[NaHCO_3]$	$\frac{a_{Ca^{2+}}}{a_{CO_3^{2-}}}$	σ	v_{st}	y_0	R	$\Delta^{44/40}$Ca	$\Delta^{44/40}$Ca
#	(M)	(M)			(nm/s)	(m)	(mol $m^{-2}s^{-1}$)	Avg. ‰	Min. ‰
7	6.03E-04	1.71E-02	1.00	2.53	8.94 (0.12)	30.11 (2.54)	2.51E-06	0.15	-0.18
8	5.12E-04	1.99E-02	1.14	2.72	-	-	-	0.91	-0.68
9	8.58E-04	2.25E-02	1.03	3.09	11.15 (0.65)	-	-	-0.22	-0.76
10	1.20E-03	3.04E-02	0.99	3.62	13.79 (0.34)	17.78 (3.27)	6.66E-06	-0.50	-1.78
12	2.50E-03	5.40E-02	0.99	4.72	42.30 (1.67)	27.73 (2.28)	1.29E-05	-0.41	-2.11
13	3.33E-04	1.00E-01	0.06	2.99	-	-	-	0.28	-0.02
14	3.70E-04	6.70E-02	0.12	2.90	-	-	-	8.43	8.10
15	6.03E-04	3.00E-02	0.54	2.90	-	-	-	0.67	0.35
18	2.17E-03	6.54E-03	11.33	2.90	-	-	-	-1.51	-1.87

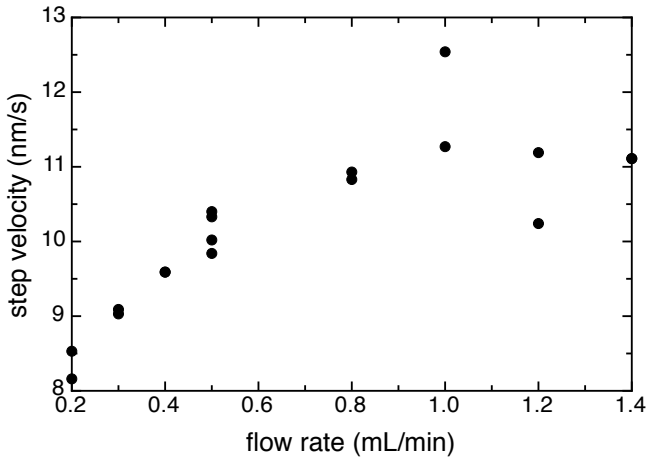

Figure 3.2: Calcite step velocity increases with increasing flow rate at low flow rates and levels off at high flow rates. Flow rates ranging from 0.8 - 1.0 mL/min were used for overgrowth experiments.

and leveled off at high flow rates (Fig. 3.2). Any flow rate between 0.8 and 1.4 mL/min produced approximately equal step velocities, so experiments were performed using flow rates in this range.

Contact AFM imaging and image processing

In situ AFM calcite precipitation experiments were performed using a Digital Instruments Nanoscope IIIa Scanning Probe Microscope in contact mode. Surfaces were scanned using silicon nitride cantilever tips with a gain of 0.3 and a deflection setpoint less than 0.5 to minimize the interaction of the tip with the calcite surface. Scan rates were varied from 3.05 to 10.2 Hz with 512 lines in each scan. The time required to complete a single scan is equal to the number of lines per scan divided by the scan rate (i.e. a 10.2 Hz scan requires $t_{scan} = 512/10.2$ Hz $= 50.2$ s for completion).

Images of growth surface topography were obtained by enabling the slow scan axis, while determinations of step velocity were made by disabling the slow scan axis. With the slow scan axis disabled, the cantilever tip scans back and forth across a fixed location perpendicular to the direction of step growth. The growing steps propagate diagonally across the scan image (Fig. 3.3). The distance traveled by a given step within a single scan is related to step velocity by the following expression:

$$v_{st} = d_{st}/t_{scan}. \tag{3.1}$$

Terrace widths may be measured directly from AFM images.

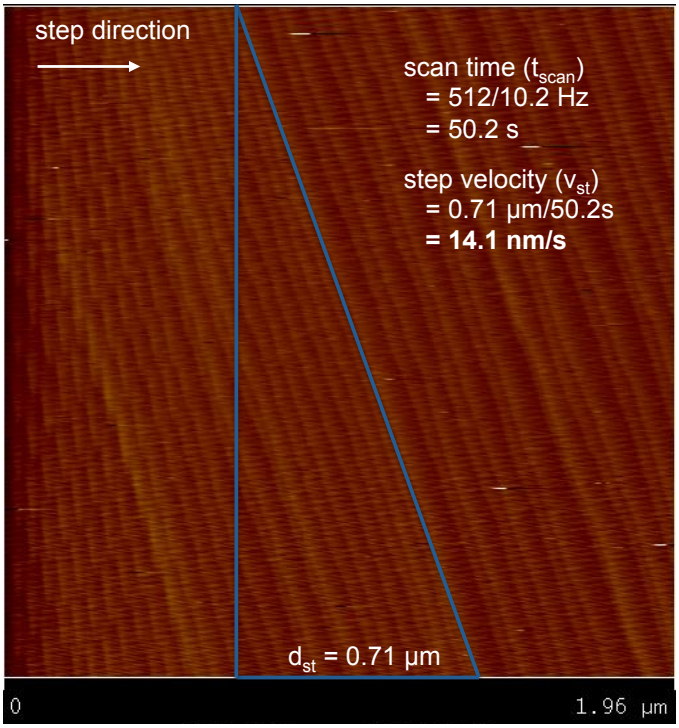

Figure 3.3: AFM deflection image of calcite step propagation with the slow scan axis disabled. Linear features in the figure are monomolecular step edges, each with a height of 3.1 Å. Step velocity is calculated from the measured distance of step propagation (d_{st}) and the scan time (t_{scan}).

3.3 TIMS methods for seed calcite standard analysis

The calcium isotopic composition of calcite internal laboratory (SIMS) standard calcite was analyzed using a Thermo-Finnigan Triton thermal ionization multi-collector mass spectrometer (TIMS) at the Center for Isotope Geochemistry, University of California-Berkeley Department of Earth and Planetary Science. Samples were prepared using ion chromatography to separate calcium. Chemical separation is important even in reasonably pure samples to minimize mass interferences from trace constituents such as ^{40}K and ^{88}Sr on the mass spectrometer. Aliquots of MEX and TT1 calcite were dissolved in ultrapure 3 N nitric acid and spiked with a ^{42}Ca-^{48}Ca tracer. The ^{42}Ca-^{48}Ca double spike method (Russell et al., 1978) was used to correct for instrumental mass fractionation and isotope discrimination during elemental separation. Spiked dissolved calcite was purified using calcium-specific cation exchange resin (DGA resin, Eichrom Technologies, normal variety). Purified calcium was loaded onto degassed, zone-refined Re double filaments with 20% H_3PO_4.

Simultaneous measurement of all Ca isotopic masses required for spike subtraction – 40,

Table 3.2: Stable Ca isotopic compositions of two calcite internal laboratory standard materials and Ca stock solution used in growth experiments analyzed via TIMS. Stock solution is 0.57(21) ‰ lighter than MEX standard calcite. Uncertainties are reported as 2 standard error (s.e.), and n is the number of replicate analyses

Sample	$\delta^{44/40}$Ca ‰ BSE	±2 s.e. ‰	n
MEX	-0.24	0.07	6
TT1	0.11	0.05	5
Stock Ca	-0.81	0.20	2

42, 43, 44 and 48 – is not possible on the Triton, which has a maximum relative mass range of 17%. A multi-step static cup configuration was used to span the range. Masses 40, 42, and 43 were measured in the first step, and masses 43, 44 and 40 were measured in the second step. Interferences from ^{40}K and ^{48}Ti were monitored in two subsequent steps by measuring ^{39}K and ^{49}Ti on the center cup. A single sample analysis was comprised of 100 cycles, each approximately 38 seconds in duration. Isotopic compositions and analytical uncertainty for each standard are listed in Table 3.2.

3.4 Development of a SIMS procedure for calcium isotope analysis

We developed a method to measure the calcium isotopic composition of calcites using the Cameca ims-1270 NanoSIMS ion microprobe located at the University of California-Los Angeles (Fig. 3.4). Only two prior studies have used SIMS to determine calcium isotopic composition of materials (Rollion-Bard et al., 2007; Kasemann et al., 2008). All growth experiments were performed on standard calcite MEX seed material, so sample standard bracketing was used to correct for instrumental mass fractionation and drift.

Sample preparation

To avoid significant instrumental fractionation due to surface topography, the surface of the calcite seed material was mounted in epoxy and polished prior to performing each overgrowth experiment. The small amount of topography caused by the precipitated overgrowth itself did not significantly influence mass fractionation. Cleaved calcite rhombs of approximately 1 cm × 1 cm were mounted in Buehler Epoxicure resin on non-magnetic metal discs. The mounts were made in 1 in cylindrical casts with cleaved MEX exposed to the surface and allowed to cure for several days. The cleaved calcite was placed at the center of the mount, because analyses of spots greater than 3500 μm from the center of the sample mount

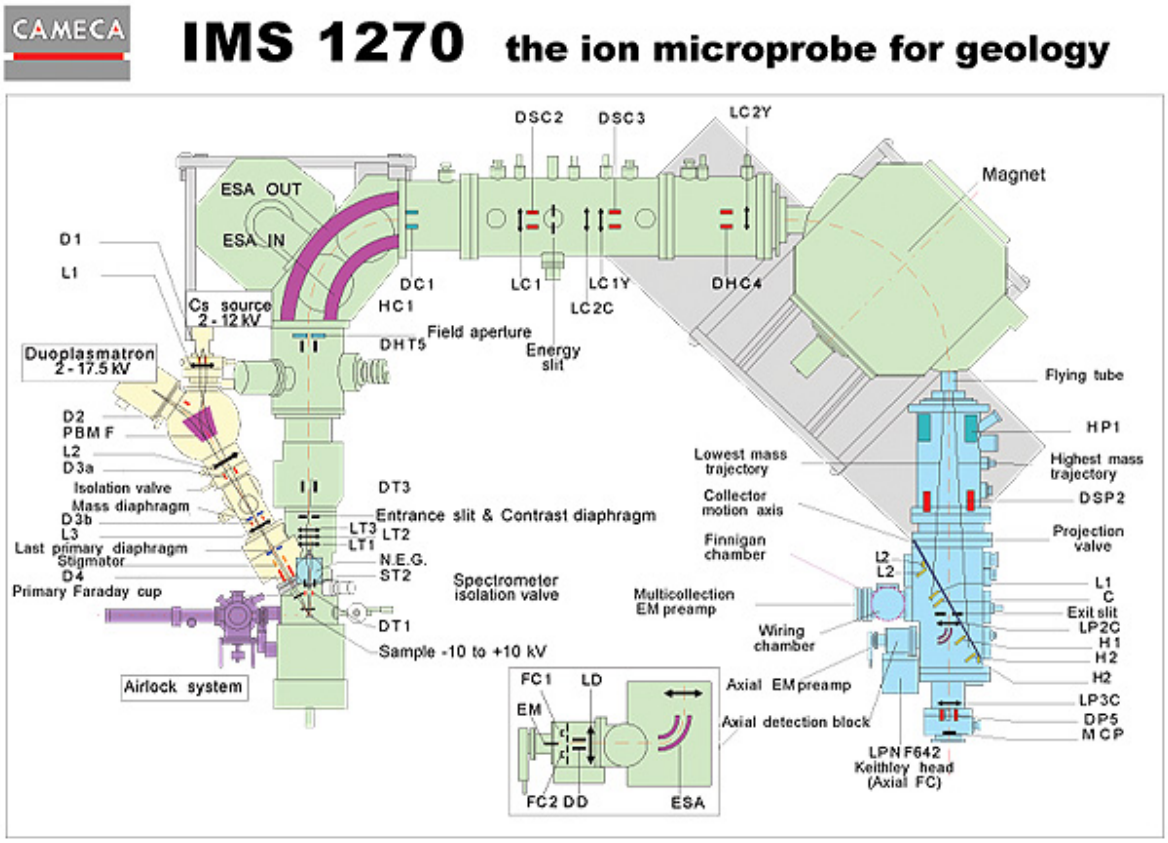

Figure 3.4: Schematic of the Cameca ims-1270 NanoSIMS ion microprobe.

produce analytical error. Once cured, the mounted samples were polished down to a final 0.06 μm Buehler Mastermet colloidal silica polish.

To minimize the formation deep scratches during the polishing procedure which would disturb precipitation of overgrowth material, the polishing procedure consisted of several steps, each as fine or finer in particle size than the one prior. The mounted sample was first ground with a coarse silicon nitride polish to remove macroscopic steps from the cleaved calcite surface. The sample was polished with 9 μm and then 3 μm Al_2O_3 powder in DI water on glass. Next a 3 μm Buehler MetaDi suspension and then a 1/4 μm Beta Diamond water soluble diamond paste were used to polish the sample on a Bueher Mastertex lap. To remove all final visible scratches from the surface, the sample was polished with a Buehler Mastermet colloidal silica suspension. The mount was quickly rinsed, soaked and sonicated in DDI water to prevent silica precipitation on the surface.

Once the overgrowth experiment was completed, the samples were coated with gold using Ar sputtering at UCLA.

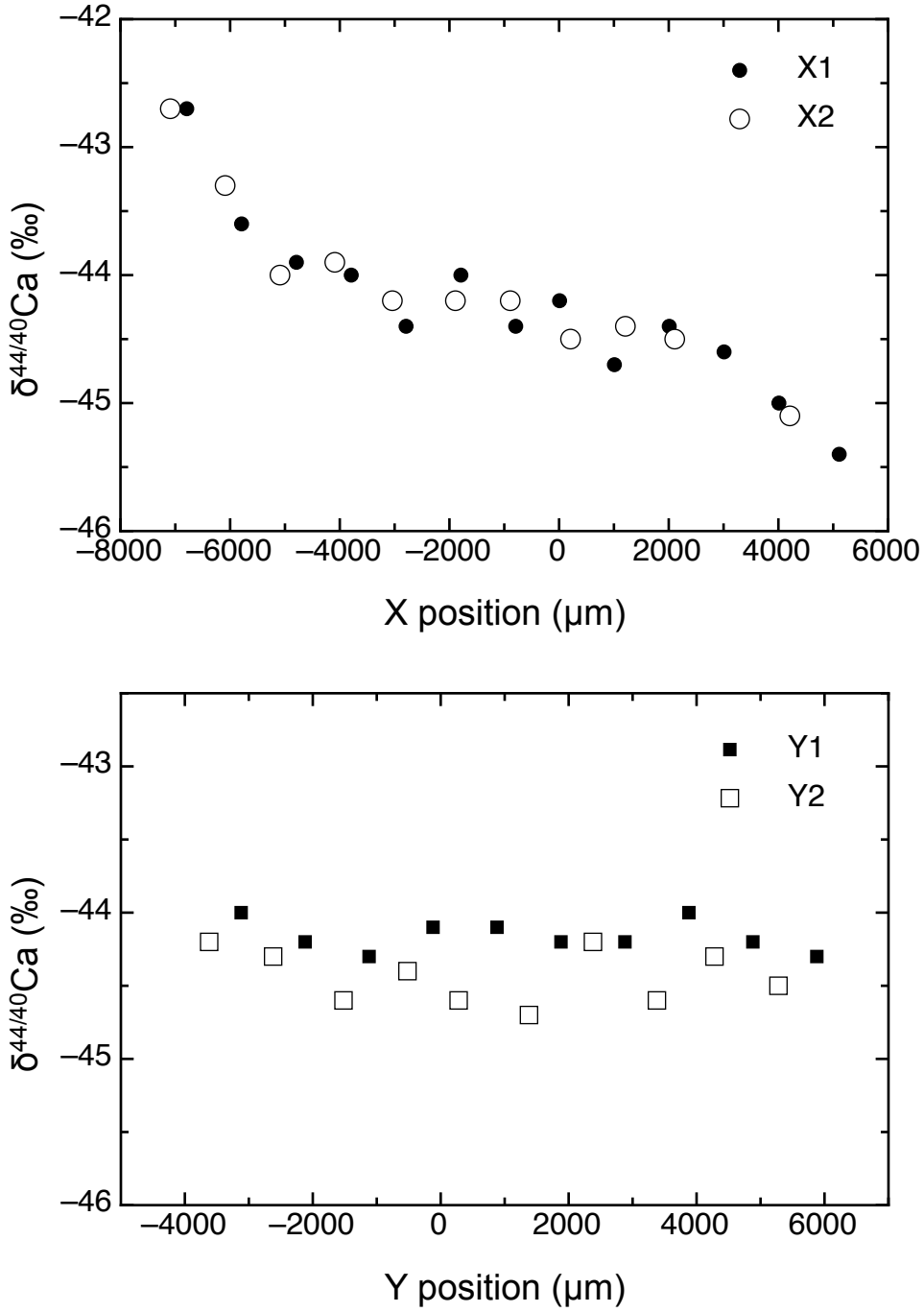

Figure 3.5: Transects of calcium isotopic composition as a function of distance along the X (top) and Y (bottom) directions. Vertical Y transects yielded the most reproducible isotopic compositions on MEX calcite.

Basic setup and measurement details

The Cameca ims-1270 was used in multicollector mode to measure Ca isotopic compositions of natural and experimentally grown calcite. Masses 40, 42 and 44 were placed in Faraday cups C, H1 and H2 respectively using slit setting 1 (500 μm) and field aperture at 4000μm. The sample mount was sputtered with a mass-filtered primary $^{16}O^{2-}$ beam at 15 nA, with oxygen flooding at 3e-5 torr. Secondary ions were collected with a 50 eV energy bandpass, and a sample high voltage offset of -10 V. The beam was focused to a size of 15 x 30 microns. An MRP greater than 2,500 was achieved using an entrance slit width of 200 μm.

After inserting a sample into the chamber, the z-axis was aligned manually to center the primary spot at the center of the mount. The beam was then manually aligned using L4, and the x and y deflectors to maximize counts at LT1, with x and y deflector settings close to 0. The entrance slit x position was centered prior to performing mass calibration and beam centering on the H1 cup. After calibration and centering, magnet NMR was turned on.

For each block of measurements, the pre-sputter time was set to 20 seconds to remove the gold coating. Once the sample was exposed, the field aperture centering procedure was used taking approximately 50 seconds. Each block consisted of 10 by 10 second cycles. Transects of polished MEX $\delta^{44/40}$Ca in the X and Y directions using these measurement settings are shown in Fig. 3.5. The measured calcium isotopic composition is reproducible with a large region of the sample surface. Transects in the Y direction yield a 2 standard error (s.e.) uncertainty of 0.10 ‰ and a 2 standard deviation (s.d.) uncertainty of 0.44 ‰ over the entire surface, while X transects yield a 2 s.e. uncertainty of 0.12 ‰ and a 2 s.d. uncertainty of 0.48‰ between -5000 and 2000 μm.

Fractionation between fluid calcium and overgrowth calcite was calculated from measured $\delta^{44/40}$Ca of MEX and overgrowth calcite using the following expression:

$$\Delta^{44/40}Ca = \delta^{44/40}Ca_{overgrowth} - \delta^{44/40}Ca_{Stock\,Ca}, \tag{3.2}$$

where $\delta^{44/40}\mathrm{Ca}_{Stock\,Ca} = \delta^{44/40}\mathrm{Ca}_{MEX} - 0.57$, because MEX calcite is 0.57 ‰ heavier than the aqueous calcium used in overgrowth precipitation experiments. Uncertainty in $\Delta^{44/40}$Ca is reported as 0.48 ‰, the 2 s.d. uncertainty of MEX.

Procedure optimization tests

Several tests were completed to optimize the procedure summarized in the previous section. The results of these tests were used to determine instrument settings that generated the most stable calcium isotope measurements with the least internal error.

Interference testing in EM mode

^{40}K interferences were ruled out based on a test of calcite sample GSD120710, which was grown in a 0.1 M KCl solution. Mass resolution was set to 12,000, and K was measured

on masses 39 and 41. A $^{39}K/^{41}K$ ratio of 10 was observed, indicating that postassim was present, with 348 counts per second (cps) on mass 41 and 3.08e4 cps on mass 39. These values yield $\sim$ 3 cps of ^{40}K in the 40 cup, which is negligible compared with the 2.5e8 cps signal from ^{40}Ca in the 40 cup. Interference by doubly ionized strontium ($^{88}Sr^{2+}$) on mass 44 was ruled out by analyzing the polished MEX calcite standard, which contains 232 ppm Sr. No counts of Sr were observed at mass 43.5.

Oxygen flooding

Oxygen flooding (3e-5 torr) improved in-run reproducibility to 0.29‰ (1 s.e.) relative to the 1 s.e. error of 0.36‰ obtained without O_2 flooding. Flooding with O_2 does not affect instrumental mass fractionation of $^{44}Ca/^{40}Ca$ at a vacuum range between 5.8e-7 and 6.4e-6. However, $\Delta^{44/40}Ca_{instr}$ is decreased by 2‰ when vacuum is increased from 6.4e-6 to 2.9e-5 torr (Fig. 3.6).

Energy offsets, oxygen flooding and automated charge control

Optimal energy offsets were determined by measuring $^{44}Ca/^{40}Ca$ for 30 $\times$ 10 second cycles over a range of -15 to 15 eV with and without O_2 flooding (Fig. 3.6).The optimal energy offset fell between -3 to -10 V during repeated sessions, and energy scans were performed in each session. The range of stable values where the isotope ratio did not change appreciably with the energy offset typically fell between -0 and -15 V. We observed no improvement in instrumental mass fractionation with automated HV charge control.

Cycle duration

Blocks of 150, 100, 30 and 10 cycle duration were tested to determine an optimal length. Short blocks of 10 cycles, with pre-sputtering (20 seconds) and field aperture alignment ($\sim$50 seconds) produced almost no in-run variability in $\delta^{44/40}Ca$ and provide the most reproducible results. Longer runs cause extreme drift, approximately 2.6‰/μm depth. Sputter rates are approximately 530 μm/sec/nA with O_2 flooding.

Crater depths and sputter rates

With pre-sputter and field alignment time excluded, secondary ion beam intensity and isotope ratios vary with cycle number. Initially an increase in secondary beam intensity is observed as the gold coating is removed and the crater is established. Intensity then decreases and eventually levels off, to a consistently decreasing value. With pre-sputtering, an analysis block of 10 cycles produces a crater depth of $\sim$ 800 $\pm$ 10 nm. Measured isotope ratios are steady from cycle to cycle.

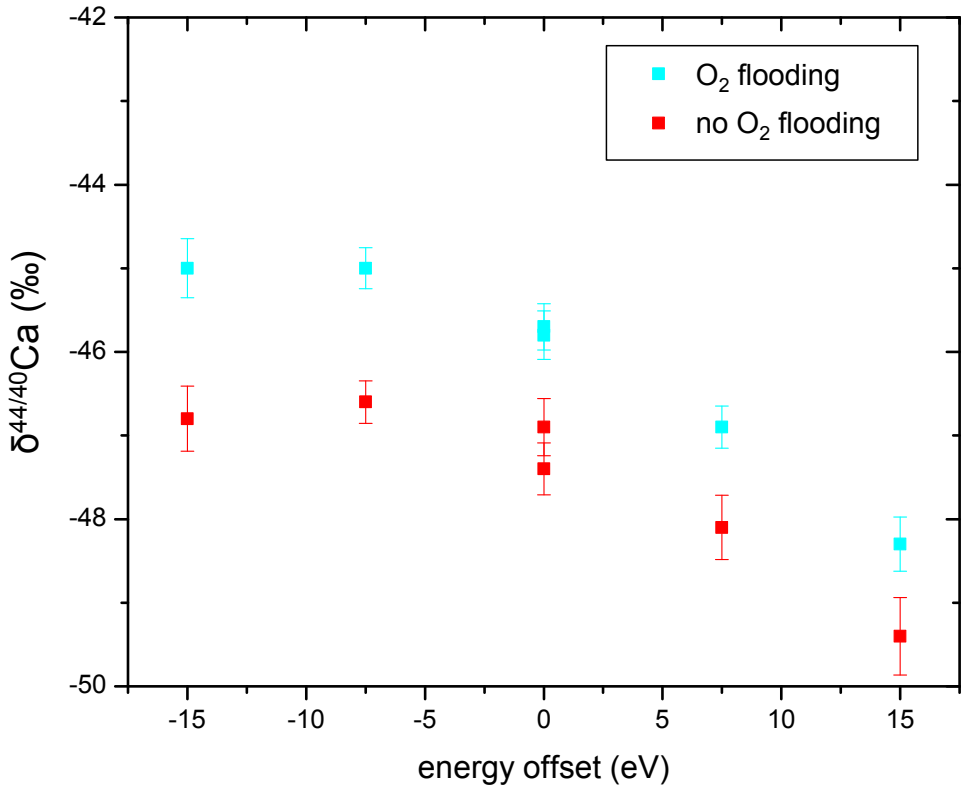

Figure 3.6: Test of measured $^{44}Ca/^{40}Ca$ isotope ratio as a function of energy offset with and without oxygen flooding on the NanoSIMS. An energy offset of -10 V was selected for analyses in this session, because this value is centered in the stable range.

Depth profiling

We performed long (60 cycle) runs with beam rastering (50 μm), 3500 field aperture and O_2 flooding to determine whether the calcite overgrowth could be internally differentiated from underlying MEX during the course of a run. Drift in mass fractionation during each block was on order 100 ‰ ($\delta^{44/40}$Ca), and no systematic offset between overgrowth and underlying MEX was apparent. The expected signal size (∼1-2 ‰) was considerably smaller than in-block variability.

Surface topography and beam deflection

To assess the effects of surface topography due to imperfect cleaving of calcite, we measured the calcium isotopic composition of an unpolished cleaved MEX sample in transects across the surface. A cleaved surface of MEX was mounted in epoxy, sonicated in ethanol and gold coated. Vertical (Y) and horizontal (X) transects of the rhomb $\delta^{44/40}$Ca were mea-

sured. Analysis position on the sample produced ∼10 ‰ variations in measured isotopic composition. A small ∼1000 μm region near the center of the sample mount yielded somewhat reproducible replicates. Large-scale sample topography observed in all natural cleaved rhombs produces irreproducible standard analyses. The same MEX rhomb was then polished following the procedure detailed above, recoated in gold, and transects were repeated. The flat, polished rhomb yielded very reproducible isotopic measurements with position (Fig. 3.5).

Interferometry of sputter pits and calcite overgrowth

After SIMS analysis of each sample, overgrowth thickness and sputter pit depths were imaged using the KLA-Tencor MicroXAM surface mapping microscope. Surface topography and linear profiles were obtained at the edge of the overgrowth from each experiment to determine overgrowth thickness. Sputter pit profiles were collected for the same samples, and overgrowth thickness was significantly greater than the sputter pit depth for each sample.

3.5 Results and Discussion

Calcite precipitation rate and growth mechanism were observed *in situ* using AFM for experiments 7, 8, 10, and 12. Experiment 12 was performed at the maximum supersaturation used in this study, so any transition in growth mechanism from low to high precipitation rates should have been captured. All calcite growth that we observed proceeded by a spiral growth mechanism, with growth hillocks emanating from dislocations at the calcite surface. Measurements of surface normal growth rate were obtained for experiments 8, 10 and 12 (Table 3.1). The observed growth rate as a function of supersaturation is consistent with a first order rate model (e.g. chapter 1)

Precipitated overgrowth material varied in texture on the calcite substrate (Fig. 3.7). Because the polishing procedure yielded flat surfaces slightly subparallel to the $\{10\bar{1}4\}$ face, most overgrowth structures consisted of stacked ledges of overgrowth instead of typical growth hillocks, although in some cases growth hillocks were still observed. For each sample, transects of $\delta^{44/40}$Ca were measured across the overgrowth, and sample analyses were bracketed with analyses of MEX standard on either side of the overgrowth.

Calcium isotopic composition varied with position on the overgrowth, indicating that the small size of the fluid reservoir in the flow cell affects the isotopic composition of the precipitate. In most samples, the position of the fluid cell influent opening was clearly visible due to the formation of thicker calcite deposits. The isotopic composition of overgrowth calcite was lightest at the center nearest the influent (Fig. 3.8). Depletion of light calcium due to calcite precipitation could cause precipitated calcite to become progressively heavier farther from the influent. Despite the relatively fast fluid flow rate through the fluid cell, a reservoir effect is apparent. The lightest measured $\delta^{44/40}$Ca values obtained from each sample are likely representative of the isotopic composition of the fastest growing calcite located at

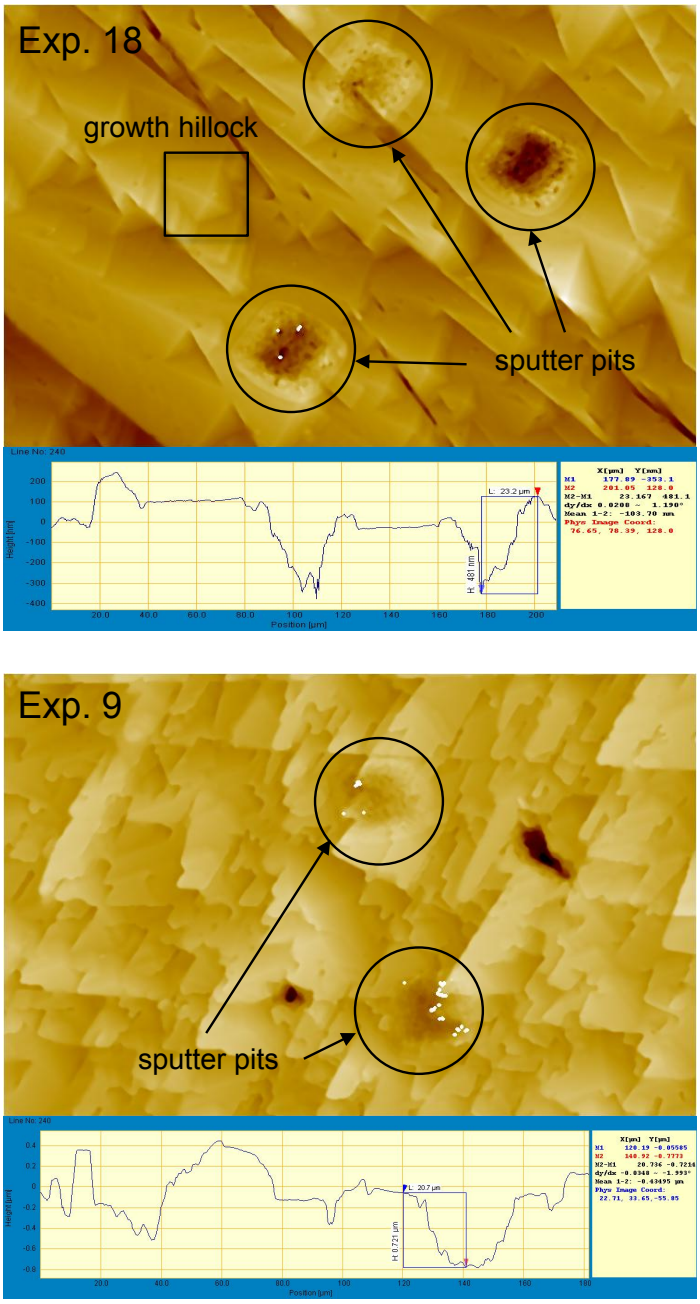

Figure 3.7: Topography and cross section of calcite overgrowth material from experiments 18 (top) and 9 (bottom). Experimentally precipitated calcite varied in texture from experiment to experiment, and growth hillocks are observed in Exp. 10, but not in Exp. 9. Individual sputter pit depths did not exceed 1 μm.

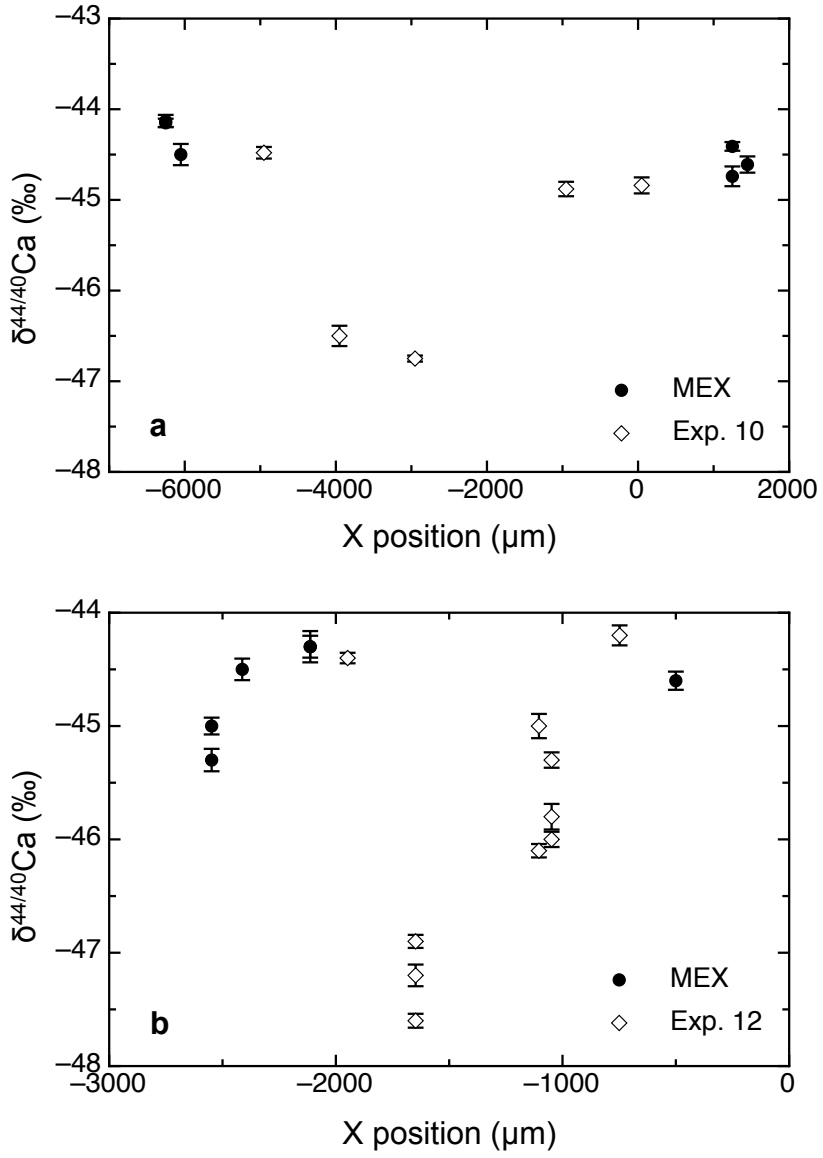

Figure 3.8: Variation in raw measured $\delta^{44/40}$Ca with distance across the overgrowth for experiments 10 (a) and 12 (b). The lightest calcite is observed towards the center of the overgrowth, nearest the fluid inlet (X $\sim$ -3500 (a) and X $\sim$ -1600 (b)). The calcium isotopic composition of each sample was measured relative to MEX standard calcite. Uncertainty reflects the internal error for each cycle.

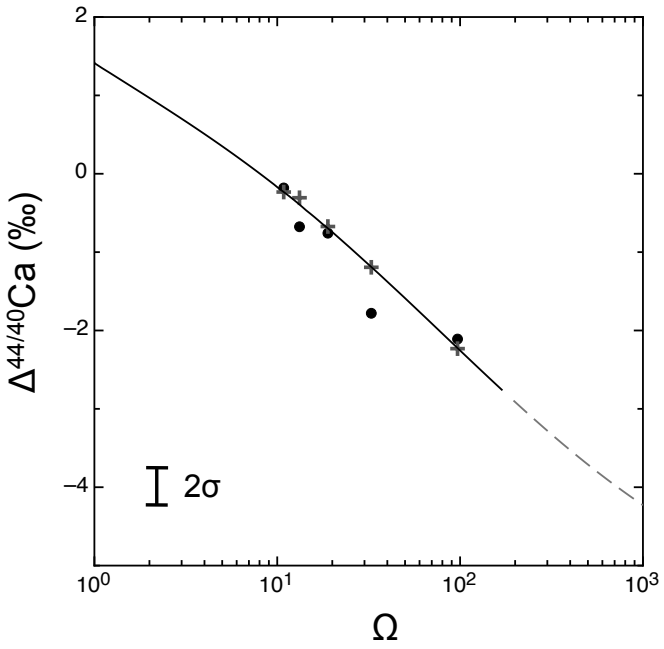

Figure 3.9: Calcium isotope fractionation as a function of calcite supersaturation ($\Omega = IAP/K_{sp}$) in stoichiometric growth solutions. The fractionation factor associated with *minimum* measured $\delta^{44/40}$Ca for a given overgrowth are displayed as filled circles (Table 3.1). The black line depicts modeled fractionation factors as a function of supersaturation (Eq. 2.13), which transitions to a dashed line above the threshold supersaturation of ACC (Clarkson et al., 1992). Model parameters include attachment and detachment rate coefficients fitted to Larsen et al. (2010) (–) step velocities (Table 2.2), an α_{eq} of 1.0015, and an α_f of 0.994. Modeled fractionation factors associated with the solution compositions from each experiment are shown as gray plus symbols. Uncertainty is reported as the 2 s.d. error of MEX X-transect analyses (0.48 ‰).

the fluid inlet. Minimum measured and average isotopic compositions of overgrowths are listed in Table 3.1, and the complete set of analyses for a given sample is listed in Appendix C.

For the fixed solution stoichiometry experiments (Exp. 7-12; Table 3.1), calcium isotopic fractionation between the solid precipitate and aqueous solution varied systematically with supersaturation. Increasing supersaturation led to faster growth and the formation of increasingly light calcite overgrowth material, consistent with the findings of Tang et al. (2008a) and Reynard et al. (2011). The highest supersaturation experiment had the lightest minimum calcium isotopic composition corresponding to a $\Delta^{44/40}$Ca of -2.1 ‰, of similar magnitude as the largest fractionation factor observed during an inorganic calcite precipitation experiment (Reynard et al., 2011). The isotopic fractionation factors were modeled

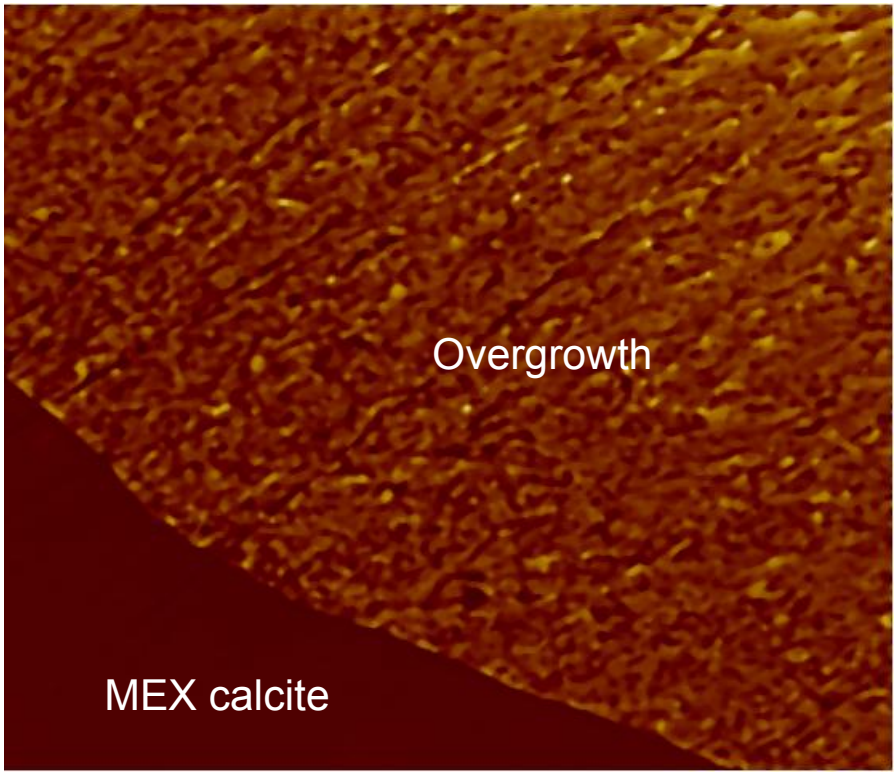

Figure 3.10: Topography of experiment 13 overgrowth material adjacent to standard polished MEX calcite, imaged using a surface mapping microscope. The overgrowth texture is uneven and porous, with relief of approximately 1.19 μm.

using equation 2.13, using attachment and detachment rate coefficients from the fit to (Larsen et al., 2010) acute step velocity data listed in Table 2.2 (Figure 3.9). The fitted equilibrium and kinetic endmember fractionation factors were $\alpha_{eq} = 1.0015$ and $\alpha_f = 0.996$ respectively. This equilibrium fractionation factor is considerably higher than fits to Tang et al. (2008a) precipitation data presented in chapter 2. Our SIMS analyses of overgrowth calcite may have missed the lightest calcite in any given sample, so the values presented and fitted here should be considered upper limits to $\Delta^{44/40}$Ca for a given supersaturaion.

Varied solution stoichiometry experiments generated overgrowth calcite with highly variable $\Delta^{44/40}$Ca. Measured isotopic compositions did not vary systematically with the calcium to carbonate ion activity ratio in solution. Several of the measured values were unreasonable (calculated $\Delta^{44/40}$Ca of up to + 8 ‰). In experiments performed at low $a_{Ca^{2+}}$:$a_{CO_3^{2-}}$, reservoir effects due to small amounts of calcite precipitation in the tubing prior to entering the fluid cell could have significantly affected the calcium isotopic composition of the overgrowth. Overgrowth textures for experiments performed at low $a_{Ca^{2+}}$:$a_{CO_3^{2-}}$ were irregular and porous (Fig. 3.10). These textures suggests that the overgrowth material from low

stoichiometry experiments could have ionized differently than the MEX standard material. This would cause the sample material to experience different instrumental mass fractionation than the standard, leading to erroneous $\Delta^{44/40}$Ca values.

3.6 Conclusion

We performed a series of calcite overgrowth experiments to confirm the relationship between reaction mechanism, growth kinetics and calcium isotope fractionation examined theoretically in chapters 1 and 2. Calcite growth was observed using *in situ* AFM, allowing us to ensure that calcite was precipitating via a spiral growth mechanism for our experimental conditions. The calcium isotopic composition of precipitated calcite was analyzed using a novel SIMS method, which provides a means to reproducibly quantify the $\delta^{44/40}$Ca of polished material at high spatial resolution.

The calcium isotopic composition of overgrowth calcite decreased systematically with increasing supersaturation, in agreement with the experiments of Tang et al. (2008a). The decrease in ^{44}Ca enrichment with increasing calcite supersaturation and growth rate is likely controlled by the rates of calcium dehydration and attachment to kink sites at the mineral surface. For varied solution stoichiometry experiments, it was not possible to obtain viable calcite overgrowth $\delta^{44/40}$Ca values. We hypothesize that the measured values were strongly affected by instrumental mass fractionation and by reservoir effects. These issues may not be possible to avoid using a fluid flow apparatus, so fluid reactor style experiments may be better suited to evaluate the effects of solution stoichiometry on calcium isotope fractionation during calcite growth. Extreme variability in solution stoichiometry can also be found in natural systems such as alkaline lakes, so these may be potential model systems for testing the hypothesis that $a_{Ca^{2+}}$:$a_{CO_3^{2-}}$ can affect isotope partitioning.

Chapter 4

Ca isotope fractionation in a high-alkalinity lake system: Mono Lake, California

4.1 Introduction

Experimental and field investigations of Ca isotope fractionation during calcium carbonate precipitation have largely focused on aqueous solutions with seawater-like compositions, where the calcium ion activity greatly exceeds the carbonate ion activity $a_{Ca^{2+}} >> a_{CO_3^{2-}}$, and near-neutral pH (Gussone et al., 2003a, 2004; Lemarchand et al., 2004; Gussone et al., 2005; Böhm et al., 2006; Tang et al., 2008a). In such solutions mineral precipitation may be limited by carbonate ion delivery to the growing mineral, but it is unlikely that aqueous diffusive transport limits the delivery of Ca or affects the Ca isotope composition of the growing mineral. For this reason it is likely that the observed Ca isotope fractionations are strongly affected by surface reaction kinetics (DePaolo, 2011), but the extent of observed fractionation will likely not reflect the true kinetic endmember fractionation factor (chapter 2; Nielsen et al., 2012). For aqueous solutions where $a_{Ca^{2+}} << a_{CO_3^{2-}}$, such as in alkaline lakes or CO_2-rich springs, it is possible that diffusive aqueous transport could be important and could mask surface reaction effects. The magnitude of surface controlled isotope fractionation would likely come closer to the kinetic endmember value in the absence of transport effects.

In situ atomic force microscope (AFM) observations of calcite precipitation reveal a significant solution stoichiometry dependence of calcite growth kinetics (chapter 2; Larsen et al., 2010). Using a kinetic steady state approach, the solution stoichiometry dependence of surface-controlled precipitation kinetics and kinetic isotope fractionation may be simultaneously modeled. Although no experiments have explicitly demonstrated the dependence of calcium isotope fractionation factor on $a_{Ca^{2+}}$:$a_{CO_3^{2-}}$, natural laboratories exist for which the model may be tested. Precipitation of calcium carbonate from alkaline lakes, where mixing

of calcium-rich springs and carbonate-rich lake water drives mineral precipitation, provides one such proving ground.

In this chapter I measured the Ca isotopic composition of calcium carbonate precipitated from an alkaline lake. The primary objectives were to determine if there is evidence that solution stoichiometry contributes significantly to carbonate formation in alkaline solutions, and to characterize Ca isotope fractionation in this environment. More generally, the alkaline lake environment is a microcosm of the global Ca cycle (cf. Rocha and DePaolo, 2000), but one that can be more fully characterized, so it presents an opportunity to test models for Ca isotope fractionation in the weathering cycle.

Mono Lake is a highly alkaline closed-basin lake east of the Sierra Nevada in eastern central California (Fig. 4.1). Fresh water and Ca are delivered to the lake by streams and springs. Evaporation concentrates the dissolved constituents leading to precipitation of abundant calcium carbonate, both in sediments at the lake bottom and near the shore where spring water enters (Russell, 1889; Cloud and LaJoie, 1980). In the near-shore environment, calcite, aragonite and magnesian calcite precipitate where spring water mixes with the high-pH, high CO_3^{2-}(aq) lake water, producing tufa towers that grow upward from the lake bottom. Tufa calcium is typically assumed to be solely derived from the spring waters entering the lake, with little to no contribution from lake water (e.g. Bischoff et al., 1993), although our findings dispute this view. The precipitation of tufa is believed to be primarily an inorganic process (Dunn, 1953), despite the abundance of organisms embedded in tufa (Scholl and Taft, 1964). However, the role of organic matter in tufa formation has yet to be fully established. The modern lake maintains a high ($\Omega > 10$) oversaturation with respect to calcium carbonate (Bischoff et al., 1993), probably due to inhibition of carbonate precipitation by phosphate.

4.2 Methods

Sampling

I collected samples of carbonate tufa and Mono Basin waters during the summers of 2009 and 2010. GPS coordinates for collection locations were recorded at the time of sampling. For each water sample, pH, temperature and conductivity were measured on a Thermo Scientific Orion StarTM Series pH and conductivity meter. Conductivity measurements were field calibrated with a 1413 μS/cm conductivity standard, and pH 4, 7 and 10 buffers were used to calibrate pH prior to each measurement. All water samples were filtered through a 0.2 μm mesh to remove particulates and acidified on-site. Acidification of high alkalinity samples caused the evolution of carbon dioxide gas; however, this should not alter the cation composition of the samples. Mono Lake water samples 9, 10, 11 and 12 were collected offshore at varied depths using a deep-water sampler, while the other lake water samples were collected from near-shore surface waters (Table 4.2). This sampling device was composed of a jug and rubber stopper lowered via a cord to the desired depth. Once at depth, the plug was pulled, and the sample was then raised to the surface. The top few inches of water were

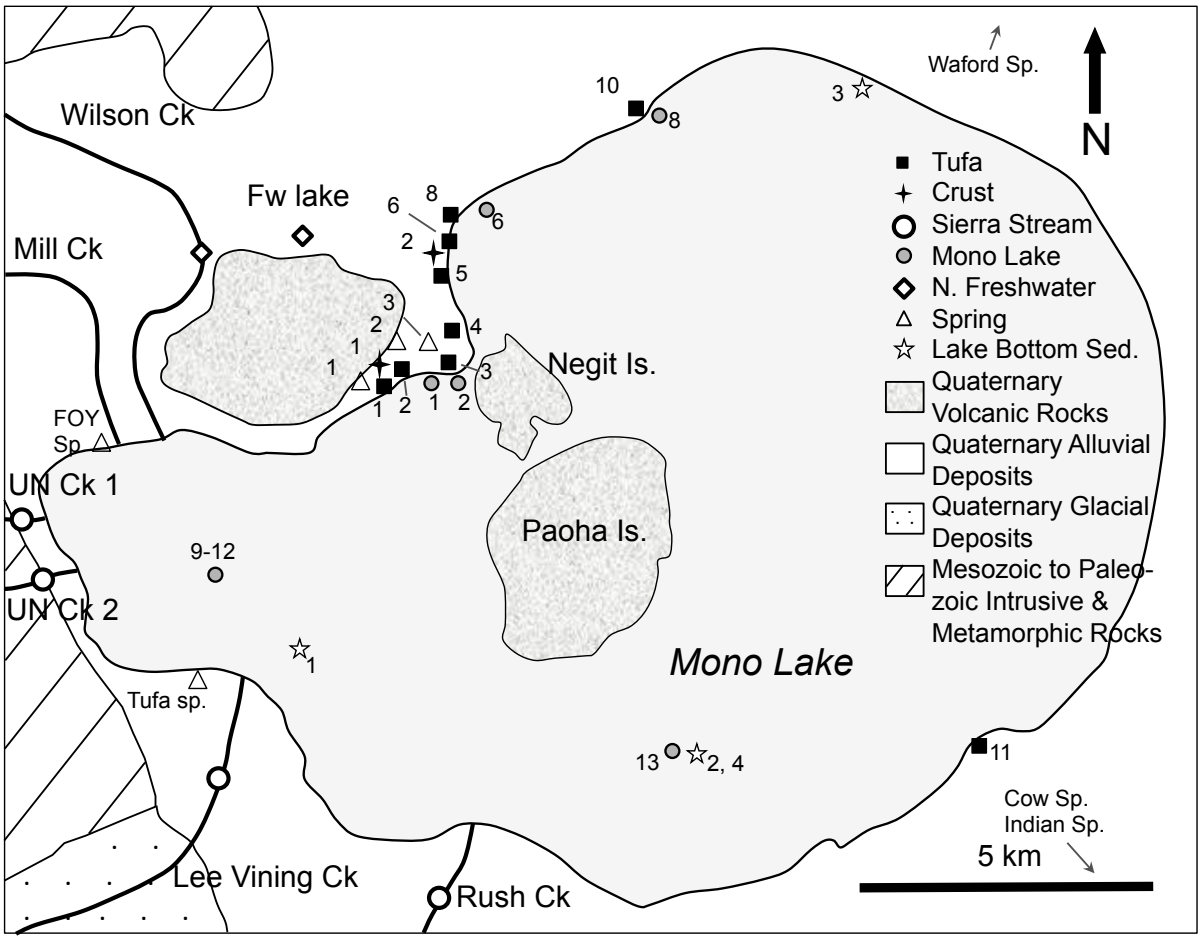

Figure 4.1: Map of sampling locations in the Mono Basin (geology based on Tomascak et al. (2003)). Strontium isotopic compositions of spring and stream waters vary significantly with location due to the effects of underlying lithology (Table 4.2). Details of solid sample position and mineralogy can be found in Table 4.7. The location of the freshwater lake is indicated by an open diamond labeled "Fw lake." Northern depleted springs referred to in the text include springs (open triangles) labeled 1, 2 and 3. Abbreviations "Ck," "Is," "Fw," and "Sp." refer to creek, island, fresh water, and spring respectively.

discarded to prevent contamination by shallower water. A single Mono Lake water sample collected in 2010 was filtered, refrigerated and not acidified for alkalinity and anion analysis. Lake bottom sediment (LBS) samples 1 and 2 were collected via Ekman grab and coring, respectively. These methods sample the top 1-2 cm of accumulated sediment. Sample LBS 3 was obtained from the top few centimeters of a shoreline push core. Solid tufa samples were chipped off of tufa towers either above the lake surface or shallowly submerged. No actively precipitating towers were observed at the time of sampling.

Archived lake and spring water samples were also obtained. These samples were all acidified prior to analysis to ensure that any secondary phases formed since collection were incorporated into the sample aliquot.

Geochemical calculations

To evaluate the driving forces for carbonate precipitation, equilibrium speciation of lake and spring water was calculated using CrunchFlow 2007 (Steefel, 2009). The original thermodynamic database does not contain magnesian calcite, a major constituent of tufa precipitated at Mono Lake. High (15 mol% Mg) and low (7 mol% Mg) magnesian calcite ($Mg_xCa_{1-x}CO_3$) were added to the database to account for these phases. The mol% $MgCO_3$ in Mono Lakes high magnesium calcite was previously determined to be 17.2% (Scholl and Taft, 1964), which is close to the value chosen for entry into the thermodynamic database. The form of high- and low- magnesian calcite precipitation reactions incorporated in the database is as follows:

$$xMg^{2+} + (1-x)Ca^{2+} + CO_3^{2-} \rightarrow Mg_xCa_{1-x}CO_3. \tag{4.1}$$

Magnesian calcite ion activity product (IAP) values were taken from Bertram et al. (1991), where the product is expressed as:

$$IAP = a_{Ca^{2+}}^{1-x} a_{Mg^{2+}}^{x} a_{CO_3^{2-}}. \tag{4.2}$$

The a values represent ionic activities, and x represents the mole fraction of Mg^{2+} incorporated into the solid. Stoichiometry and IAP values for high-Mg and low-Mg calcite reactions at 25°C included in the database are presented in Table 4.1 (Bischoff et al., 1987; Bertram et al., 1991). The molar volume of magnesian calcite was assumed to be the same as that of calcite, 36.9340 cm^3/mol. Speciation calculations predict supersaturation with respect to dolomite, but no dolomite is observed, probably because of kinetic limitations to significant Mg incorporation and dolomite precipitation (cf. Morse et al., 2007).

Isotopic analyses

Calcium and strontium concentrations and isotope compositions were measured via the double-spike method in the Center for Isotope Geochemistry, University of California-Berkeley.

Table 4.1: Stoichiometry and solubility data for high and low magnesian calcite added to the CrunchFlow(2007) thermodynamic database for this study. The stoichiometric coefficient of magnesium for each of the magnesian calcite phases is listed under X.

Species	**X**	**-log(K_{sp})**	**Molecular Mass**
High Mg Calcite	0.15	8.40 (Bischoff et al., 1987)	97.7209
Low Mg Calcite	0.07	8.48 (Bertram et al., 1991)	98.9828

Solid tufa and crust samples were dissolved in 3 N HNO_3 and alkaline lake waters were reacted with 3 N HNO_3 prior to spiking with a ^{42}Ca-^{48}Ca double spike for calcium, and an ^{84}Sr tracer for strontium. Fresh waters were spiked directly. Lake bottom sediment was rinsed with 18 MΩ doubly deionized (DI) water, centrifuged, and leached with acetic acid to extract calcium and strontium from the carbonate fraction. The leached sample was spiked and processed with tufa and water samples.

Ca separation was performed using Ca-specific Eichrom DGA resin on acid-washed Teflon columns with a resin volume of 250-300 μL and a reservoir volume of 1 mL. The DGA resin was suspended in DI water, and approximately 250 μL were pipetted into each column. The columns were rinsed thee times with 1 mL of DI water, once with 1 mL of 3N HNO_3 and once with DI water followed by a final 0.5 mL rinse with 3N HNO_3. Spiked samples were dried and redissolved in 100 μL 3N HNO_3, which was pipetted directly onto the clean resin. Loaded columns were then sequentially rinsed with 100, 300 and 500 μL of 3N HNO_3. Calcium was collected using a final rinse of 1 mL DI water.

Approximately 3 μg of spiked and separated calcium was loaded with 20 % H_3PO_4 onto zone-refined Re double filaments and loaded onto a Finnigan Triton multicollector thermal ionization mass spectrometer (TIMS) for analysis. For details on the analytical procedure see Nielsen et al. (2011). Calcium isotopic compositions are reported relative to bulk silicate Earth (BSE; Simon and DePaolo, 2010; Nielsen et al., 2011) in the standard delta notation (‰):

$$\delta^{44/40}\mathrm{Ca} = \left(\frac{([^{44}\mathrm{Ca}]/[^{40}\mathrm{Ca}])_{sample}}{([^{44}\mathrm{Ca}]/[^{40}\mathrm{Ca}])_{BSE}} - 1 \right) \times 1000. \tag{4.3}$$

The NIST SRM 915a standard is used as laboratory standard and has a $\delta^{44/40}$Ca of -0.97(04) relative to BSE (Simon and DePaolo, 2010). The 2 standard deviation (2 s.d.) external reproducibility associated with all $\delta^{44/40}$Ca measurements is 0.15 ‰. Each reported $\delta^{44/40}$Ca is the average of at least two replicate analyses. Isotope dilution measurements of calcium concentration yield uncertainties of within ± 2%.

Sr isotope separations were performed on cation exchange columns using Eichrom Sr Spec resin following the procedure detailed in Fantle and DePaolo (2006). Each lake water sample was run twice through column chemistry to separate the small amount of Sr from the large total dissolved solids. Aliquots of ∼30 ng Sr were loaded onto Re single filaments for isotopic analysis, with TaCl added to enhance ionization, and measured using the same

instrument as calcium analyses. Measurement details may be found in Fantle and DePaolo (2006). Strontium isotopic compositions are reported with 2 s. e. internal errors, and uncertainties on Sr isotope dilution concentration measurements have been estimated to be within ± 2%.

Samples containing about 10 to 100 μg of calcite or aragonite were used for both carbon and oxygen isotope analyses, which were determined using a GV IsoPrime mass spectrometer with Dual-Inlet and MultiCarb systems in the Laboratory for Environmental and Sedimentary Isotope Geochemistry (LESIG) at the Department of Earth and Planetary Science, University of California-Berkeley. Several replicates of two international standards, NBS18 and NBS19, and one lab standard were measured along with samples for each batch run. The overall external analytical precision is 0.04‰ for δ^{13}C and 0.07 ‰ for δ^{18}O.

Major and trace element concentrations

Trace metal concentrations were measured on water samples via ICP-MS at the Lawrence Berkeley National Laboratory. Before analysis, samples were acidified to 2 % by volume HNO_3 using ultra high purity (BDH Aristar Seastar) nitric acid diluted with 18.3 MΩ high purity water. Samples were then spiked with internal standards. All preparations were done by mass. Samples were then analyzed on a PerkinElmer Elan DRCII ICP-MS using a multi-element method with ^{6}Li, ^{71}Ga, ^{115}In, ^{169}Tm and ^{193}Ir as internal standards. To eliminate interferences, K and Ca were analyzed with NH_3 as a reaction gas. NIST SRM 1643e was used to validate the method. Reproducibility of analyses is better than ± 5 % RSD.

Total dissolved inorganic carbon was measured using a Shimadzu TOC-VCSH. Fluid samples were injected into the IC reaction vessel containing a continually sparged phosphoric acid solution. Volatilized CO_2 was measured by a non-dispersive infrared gas analyzer (NDIR) using TOC-Control V software. Anions were analyzed using a Dionex ICS-2100 with AS-DV autosampler and KOH (potassium hydroxide) eluent. Sample fluid was injected into the column and analyzed using Chromeleon 7 software.

4.3 Mono Basin Sr and Ca isotopic compositions

Our objective was to evaluate the Ca isotopic fractionation associated with aragonite and calcite precipitation from Mono Lake water, and to constrain the calcium budget of Mono Basin in the recent past. The lake is a dynamic system with water and dissolved constituents continuously being added from streams and springs. Carbonate can be precipitated from incompletely mixed lake and fresh waters, so it is necessary to have a tracer that can provide information on the components of the waters from which carbonate minerals precipitated. We used Sr isotopes for this purpose, because there is substantial variability in the Sr isotopic composition of water inputs to the lake due to the heterogeneous lithology of Mono Basin. The Sr and Ca isotopic composition of lake, stream, spring, tufa, crust and lake bottom sediment samples from the Mono Basin are listed in Table 4.2. Sample locations

corresponding to Ca isotopic results are shown in Fig. 4.1, and isotopic data are plotted in Fig. 4.2.

Table 4.2: Calcium and strontium isotopic composition and concentration analyses of water and solid samples from the Mono Basin. Abbreviation "FW" for stands for fresh water, "LBS" for lake bottom sediment, and "UN" for unnamed. Mono Lake water samples Lk. 2009 9-12 are a depth profile of the lake at 3 m, 10 m, 15 m and 17.5 m (lake bottom). Ca isotopic compositions are averaged from duplicate analyses on all samples. Uncertainty is 0.15 ‰ (2 s.d.) for Ca isotope analyses and less than 5×10^{-6} for Sr isotope ratios with error reported as (0). Concentrations of Sr and Ca have an uncertainty of ± 2 %. Samples are categorized into 8 types: depleted spring (DS), spring (Sp), Mono Lake water (ML), Northern freshwater (NF), shoreline crust (CR), tufa tower (TF), lake bottom sediment (LBS), and Sierra Nevada stream (SNS). Archived samples are denoted by *.

Sample	**Type**	$\delta^{44/40}$**Ca (‰ BSE)**	**[Ca] (ppm)**	^{87}**Sr/**^{86}**Sr**	**[Sr] (ppm)**	**[Sr]/[Ca] (× 10^3)**
Spring 1	DS	0.77	1.61	0.708466(7)	7.59e-3	4.71
Spring 2 FW	DS	0.66	1.21	0.708410(26)	1.52e-3	1.26
Spring 3	DS	1.09	2.06	0.708139(99)	7.96e-3	3.86
Waford Sp.*	SP	-0.04	1.62	0.707502(4)	1.17e-2	7.23
Indian Sp.*	SP	-0.07	18.5	0.706456(5)	2.31e-1	12.5
Tufa Sp.*	SP	-0.48	23.4	0.709709(3)	8.13e-2	3.47
FOY Sp.*	SP	-0.42	20.3	0.709758(3)	7.22e-2	3.56
Cow Sp.*	SP	-0.52	4.71	0.706404(3)	4.89e-2	1.04
Lk. 1996*	ML	2.46	2.54	-	-	-
Lk. 2004-1*	ML	0.25	12.9	-	-	-
Lk. 2004-2*	ML	0.05	12.0	-	-	-
Lk. 2005*	ML	1.12	4.24	0.70917(1)	3.20e-2	7.55
Lk. 2009-1	ML	0.8	7.37	-	-	-
Lk. 2009-2	ML	0.57	7.66	0.709080(27)	1.27e-2	1.66
Lk. 2009-6	ML	0.92	7.09	0.709123(15)	2.11e-2	2.97
Lk. 2009-8	ML	0.75	7.77	0.708919(102)	2.94e-2	3.78
Lk. 2009-9	ML	0.48	8.10	0.709161(56)	3.15e-2	3.88
Lk. 2009-10	ML	0.64	8.09	0.709221(28)	3.13e-2	3.87
Lk. 2009-11	ML	0.63	7.95	-	3.15e-2	3.96
Lk. 2009-12	ML	0.48	7.82	0.709023(43)	3.17e-2	4.05
Lk. 2010	ML	0.57	8.34	0.708963(9)	2.98e-2	3.58
Freshwat. Lk	NF	0.13	10.9	0.708247(3)	8.21e-2	7.55
Wilson Ck	NF	-0.12	8.41	0.709714(3)	2.51e-2	2.99
Crust 1	CR	-0.26	3.01e3	0.708531(9)	1.97e1	6.55
Crust 3	CR	-0.26	1.09e5	0.708762(3)	6.91e2	6.32
Tufa 1	TF	-0.08	2.89e5	0.708907(13)	2.42e3	7.36

Continued on Next Page...

Sample	Type	$\delta^{44/40}$Ca (‰ BSE)	[Ca] (ppm)	^{87}Sr/^{86}Sr	[Sr] (ppm)	[Sr]/[Ca] ($\times$ 10^3)
Tufa 2	TF	-0.41	3.46e5	0.708930(8)	2.13e3	6.15
Tufa 3	TF	-0.39	3.46e5	0.708947(3)	1.99e3	5.76
Tufa 4	TF	-0.33	3.88e5	0.708997(3)	2.62e3	7.38
Tufa 5	TF	-0.25	3.66e5	0.709016(5)	2.20e3	6.02
Tufa 6	TF	-0.23	1.45e5	0.708982(6)	8.00e2	5.53
Tufa 8	TF	-0.37	1.72e5	0.708932(3)	7.77e2	4.52
Tufa 10	TF	-0.37	3.39e5	0.708991(3)	2.09e3	6.17
Tufa 11	TF	-0.33	3.25e5	0.708990(5)	1.91e3	5.87
LBS 1	LBS	0.02	-	0.709044(5)	-	-
LBS 2	LBS	-0.08	-	0.709047(8)	-	-
LBS 3	LBS	-0.46	-	0.708832(5)	-	-
LBS 4	LBS	-0.63	-	0.708887(5)	-	-
Lee Vining Ck.	SNS	-0.37	3.97	0.709762(3)	1.50e-2	3.78
Rush Ck.	SNS	-0.51	6.02	0.709709(4)	1.89e-2	3.15
UN Ck. 1	SNS	-0.47	12.8	0.711532(3)	3.40e-2	2.66
UN Ck. 2	SNS	-0.45	5.95	0.708821(3)	4.66e-2	7.83

Compositions of stream waters

Stream waters flowing from the Sierra Nevada constitute the main flux of water and chemical constituents to the lake (Garrels and Mackenzie, 1967) and have ^{87}Sr/^{86}Sr values between 0.708821(3) and 0.711532(3). The observed variability in Sr isotope ratios reflects the wide range of values measured in Mono Basin bedrock (Neumann and Dreiss, 1995). The highest values are radiogenic compared with bulk bedrock Sr isotope ratios. The two largest streams flowing into Mono Lake, Rush Creek (Neumann and Dreiss, 1995) and Lee Vining Creek, have a more limited range of isotopic values; ^{87}Sr/^{86}Sr of 0.709762(3) and 0.709709(4), and $\delta^{44/40}$Ca of -0.51 and -0.37 respectively. The average $\delta^{44/40}$Ca of streams flowing into Mono Lake from the Sierra Nevada is -0.45(13) (2 s.d., n = 4). Wilson Creek, which flows directly into the northern lake region where the majority of tufa samples in this study were collected, has a similar ^{87}Sr/^{86}Sr of 0.709714(3), but its $\delta^{44/40}$Ca is 0.25(21) ‰ heavier than Vining Creek. The fresh water lake just North of the sampled tufa has an ^{87}Sr/^{86}Sr of 0.708247(3) and a $\delta^{44/40}$Ca of 0.13, 0.25(21) ‰ heavier again than Wilson Creek water (Table 4.2). We classify the Wilson Creek and freshwater lake samples as Northern Freshwater in Fig. 4.2, because they are distinctly heavier in Ca isotopic composition than the Sierra Nevada stream waters (Rush Ck, Lee Vining Ck, UN Ck 1 and UN Ck 2) flowing into the western lakeshore.

The variability of the ^{87}Sr/^{86}Sr in Sierran stream waters may be explained by selective mineral weathering of source rocks (e.g. Blum et al., 1993; Neumann and Dreiss, 1995) as

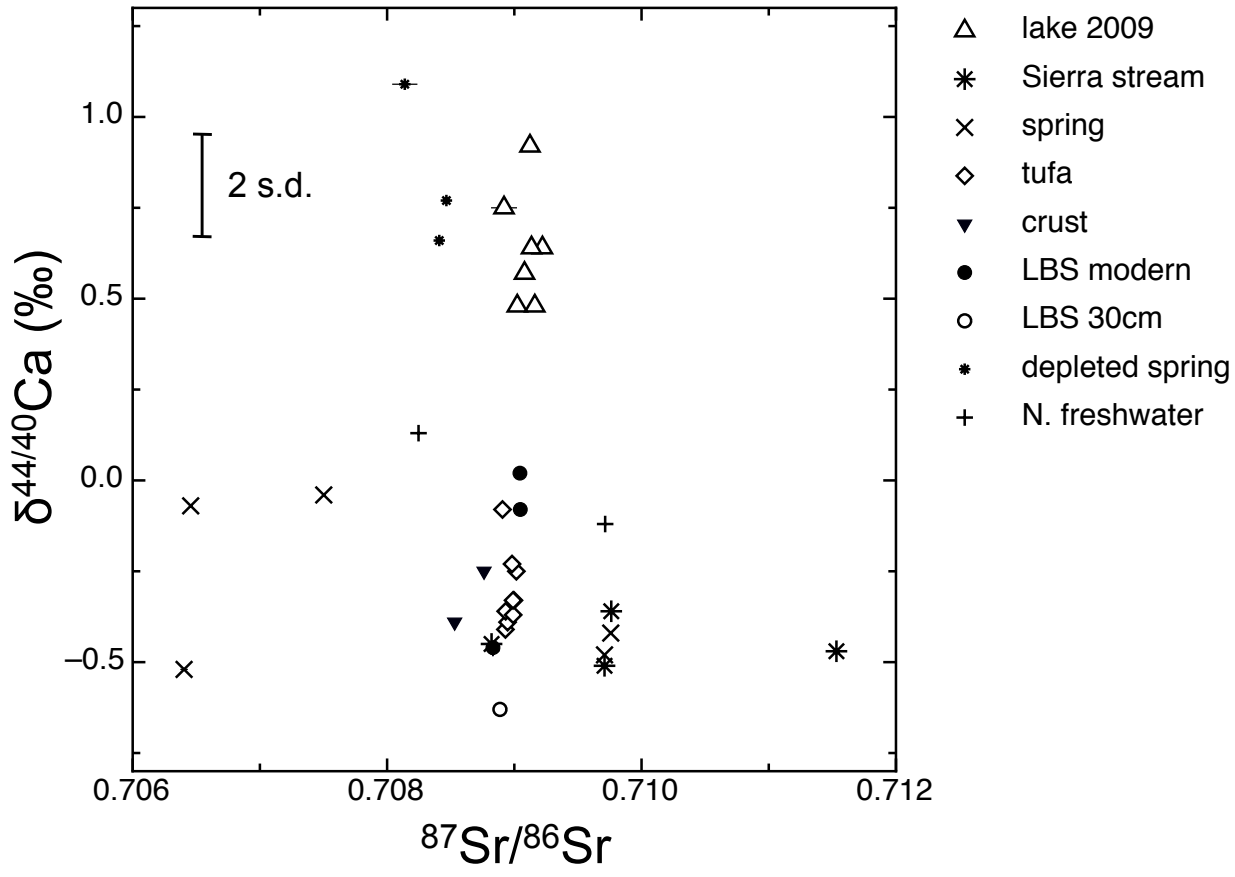

Figure 4.2: Sr and Ca (BSE) isotopic compositions of Mono Basin samples. Standard errors for $^{87}Sr/^{86}Sr$ are marked for each sample and are smaller than marker size if not visible. The label LBS represents lake bottom sediment.

well as by lithologic heterogeneity in the stream drainage basins. Each stream samples a distinct subset of intrusive rocks with different Rb/Sr and initial $^{87}Sr/^{86}Sr$ ratios as well as different proportions of metamorphic roof pendant rocks. Roof pendant rocks vary widely in proportion of siliceous and carbonate components and are generally early Paleozoic in age. There is evidence that prior to 300 Ma, seawater (and limestone) had $\delta^{44/40}Ca$ about 0.5 ‰ lower than today (Farkaš et al., 2007), which is consistent with observed light stream water $\delta^{44/40}Ca$ values.

Compositions of spring waters

High-Ca spring water samples (> 5 ppm) span a "wide" range of strontium isotopic compositions (0.706456(5)-0.709758(3)), similar in magnitude to stream water variability. These springs are associated with light calcium isotopic compositions (-0.07 to -0.48 ‰), which also resemble the Sierran stream waters. The majority of Ca entering the lake by way of springs is likely sourced by the same lithologies as stream water and is therefore similar in Sr and Ca isotopic composition.

Low-calcium spring water sampled directly adjacent to tufa towers along the northern shore (Fig. 4.2 and 4.6) had an average $^{87}Sr/^{86}Sr$ value of 0.70834(35), which falls within the range of non-western-shoreline spring Sr isotopic compositions presented by Neumann and Dreiss (1995). This range indicates that the springs represent the low-$^{87}Sr/^{86}Sr$ groundwater typical of the areas dominated by Miocene and younger volcanic rocks (Neumann and Dreiss, 1995). The calcium isotopic compositions of low-Ca (< 2.1 ppm) springs are heavy, with $\delta^{44/40}Ca$ between 0.66 and 1.09. It is possible that these heavy compositions result from precipitation of isotopically light calcium-bearing minerals *en route* to the surface, forming calcium-depleted spring waters. Depleted spring waters are not thought to contribute significantly to tufa formation.

Composition of Mono Lake water

Mono Lake water is spatially variable in both Ca and Sr isotopic composition. The $^{87}Sr/^{86}Sr$ of the lake falls between 0.708919(102) and 0.709221(28), and $\delta^{44/40}Ca$ of lake water sampled on a single day varies from 0.48 to 0.92. The average $\delta^{44/40}Ca$ of 2009 Mono Lake water was 0.65(14) (1 s.d., n = 10) and the average $^{87}Sr/^{86}Sr$ is 0.70908(21). Samples 2009 9-12 represent a depth profile of the lake sampled at 3, 10, 15 and 17.5 m (bottom), respectively. Neither Sr nor Ca isotopic compositions of lake water are correlated with depth; however, there is a slight increase in Ca concentration towards the lake bottom.

The concentration and calcium isotopic composition of Mono Lake water changes dramatically with time (Figs. 4.3 and 4.4), while the strontium isotopic composition remains steady. Between 1950 and the mid-1990s, most reported lake water calcium concentrations are approximately 4 ± 2 ppm (Jones and Stokes, 1993; Bischoff et al., 1993; Jellison et al., 1993; Neumann and Dreiss, 1995). Between 1996 and 2010, the concentration has varied between 2.5 and 12.5 ppm, indicating variability in the lake water calcium budget. Concentration is strongly correlated with $\delta^{44/40}Ca$ in lake water; calcium-rich (12.5 ppm) lake water is light (0.12), while calcium-poor (2.5 ppm) lake water is extremely heavy (2.46). The rapid changes in calcium isotope composition are unsurprising considering the short (5-25 yr) residence time of calcium in Mono Lake, but unusual considering the apparently stable calcium concentration prior to 2003 (Fig. 4.4). The isotopic composition of 4 ppm Mono Lake water – 1.12 ‰ – likely reflects the steady state composition of the lake.

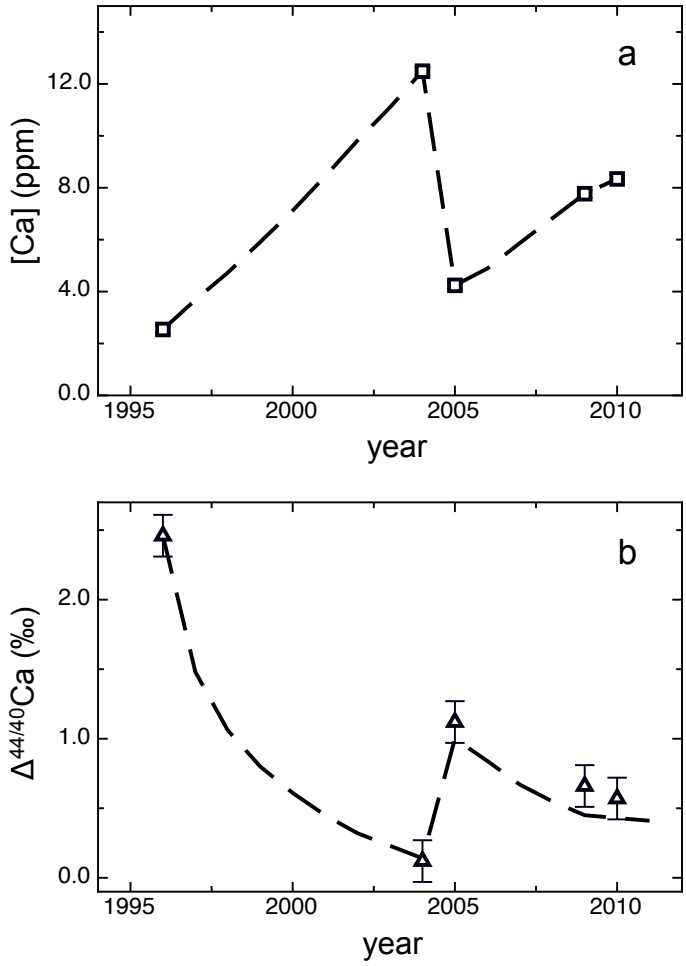

Figure 4.3: (a) Calcium concentrations and (b) isotopic compositions of Mono Lake water analyzed in this study. The dashed line in both figures represents the fitted Mono Lake calcium budget based on Eq. 4. The abrupt decrease in calcium concentration between 2004-2005 coincides with the breakdown of meromixis recorded in 2003.

Compositions of precipitated carbonate minerals

Tufa sampled from the northern lakeshore falls within a narrow range of $^{87}Sr/^{86}Sr$, 0.708907(13)-709016(5) (Table 4.2). The average $^{87}Sr/^{86}Sr$ of calcium-depleted shoreline springs located adjacent to sampled tufa, 0.70834(35), is lower than tufa, 0.70896(27), with a probability (p) of the null hypothesis equal to 3e-6 from the two-sample equal variance student's t test. The average $^{87}Sr/^{86}Sr$ of Mono Lake water is higher than tufa, and this difference is also statistically significant ($p = 0.01$). The tufa Sr isotopic composition is a measure of the proportions of water from different sources. Assuming a reasonably constant

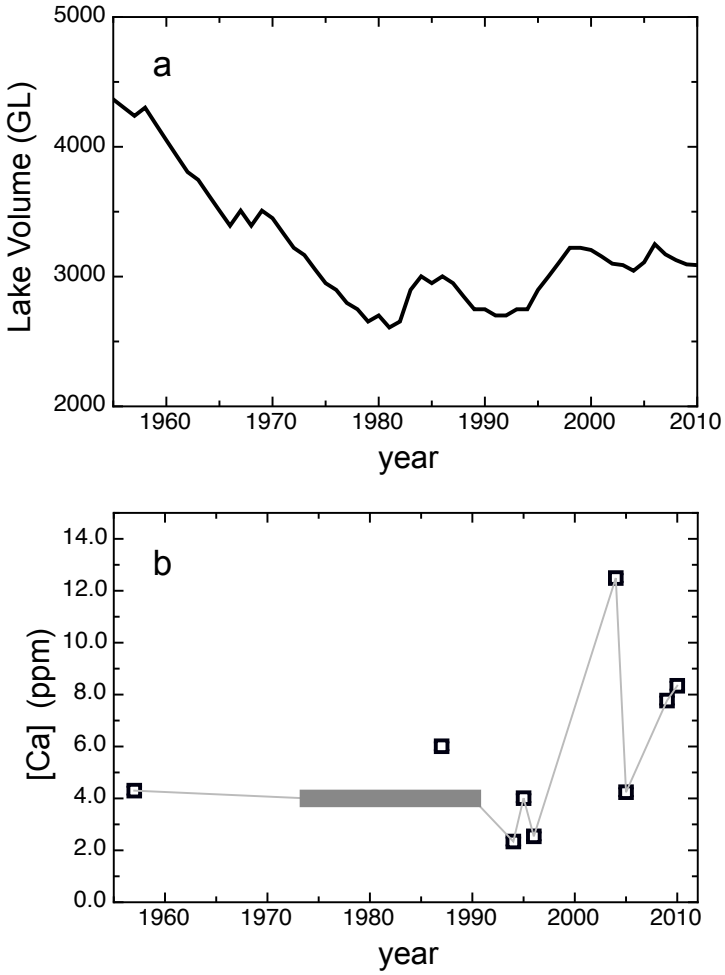

Figure 4.4: (a) Mono Lake volume in billions of liters (GL) and (bottom) calcium concentration between 1955 and 2010. Lake volume decreased dramatically between 1940 until 1980 due to stream water diversions by the LADWP. (b) The calcium concentration of Mono Lake water had a median value of 4 ppm between 1974 and 1990 (Jones and Stokes, 1993), represented by the solid gray bar.

Mono Lake water Sr isotopic composition, the measured ranges and values indicate that the Sr isotopic composition of tufa is controlled primarily by Mono Lake water, but with a minor spring water contribution.

The $\delta^{44/40}$Ca values of tufa towers sampled in this study are between -0.41 and -0.08 ‰. The calcium isotopic composition of tufa collected from Navy Beach along the southern lakeshore (Tufa 11; $\delta^{44/40}$Ca = -0.33) is identical in $\delta^{44/40}$Ca to the average calcium isotopic composition of northern tufa, -0.30(21). Tufa samples were crushed and homogenized prior to analysis, so each represents the composition averaged over many years of growth. Sampled tufa towers likely formed at different times, so the minimal isotopic variability suggests that the long-term Mono Lake Ca isotope budget is not highly variable.

Recently precipitated salt crusts coat the northern shoreline of Mono Lake. These crusts are likely formed due to evaporation of lake water accompanied by mixing with spring water. Sodium carbonate and chloride minerals including trona and halite make up the bulk of these crusts. Minor carbonate minerals present in the crusts have $\delta^{44/40}$Ca values of -0.26, in the middle of the range found for tufa. The $^{87}Sr/^{86}Sr$ ratios of the crust carbonate are substantially lower than those of tufa, which indicates that the water they precipitated from had a significant proportion of low-$^{87}Sr/^{86}Sr$ spring water.

The $\delta^{44/40}$Ca of contemporary lake bottom sediment collected far from shore varied from -0.46 to 0.02 (Table 4.2). A single sample of down-core sediment has a significantly lighter calcium isotopic composition, -0.63, indicating that the lake bottom sediments may reflect recent changes to the lake water isotopic composition. The lake bottom sediment carbonate mineral fraction precipitates directly from the water column and is therefore not affected by mixing with spring waters along the shoreline. Lake bottom carbonate is a significant component of the Mono Basin Ca budget.

4.4 Discussion

Mono Lake Ca isotope budget

The Ca budget of Mono Lake is schematically portrayed in Fig. 4.5. Most calcium enters the basin via streams from the Sierra Nevada (Jones and Stokes, 1993; Tomascak et al., 2003), which contain dissolved mineral weathering products (e.g. Garrels and Mackenzie, 1967). Silicate mineral weathering is supplemented by the dissolution of small amounts of secondary calcium carbonate and marble during water transport to the lake. Water flowing from the Sierra Nevada constitutes the greatest influx of Ca to Mono Lake (denoted F_{SN}), so the Ca isotopic composition of Sierra streams and springs is approximately equal to the isotopic composition of the Ca supply to the lake. A recent estimate of the total Ca flux to Mono Lake is 2.21×10^6 kg Ca/yr, with contributions from streams (1.75×10^6 kg Ca/yr), groundwater (4.5×10^5 kg Ca/yr), and springs (1.25×10^4 kg Ca/yr) (Tomascak et al., 2003). The total stream runoff reported by Tomascak et al. (2003) is close to the total average

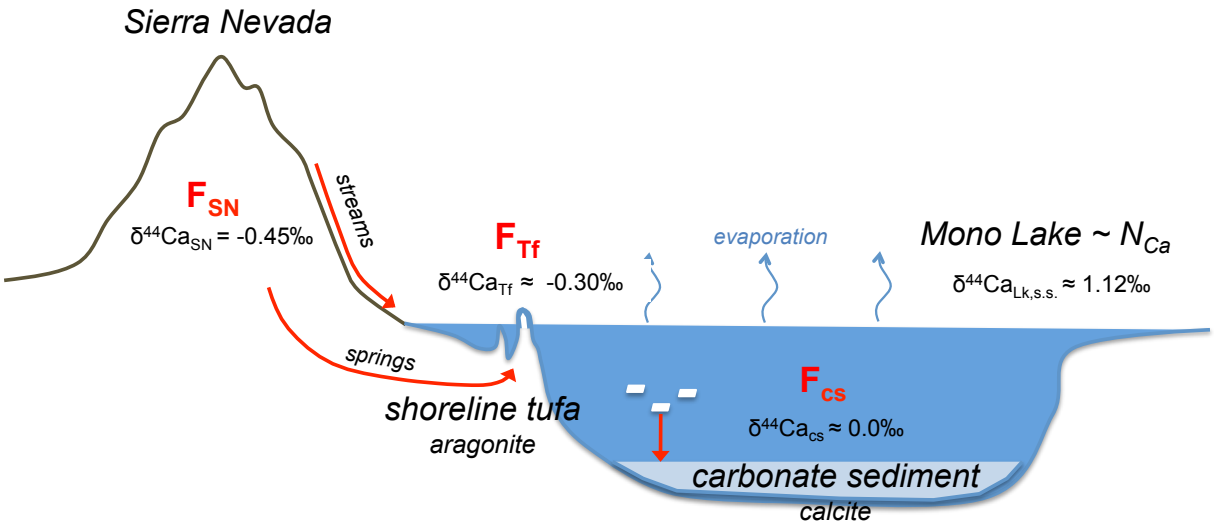

Figure 4.5: Ca budget for Mono Basin. The primary Ca flux into Mono Lake (F_{SN}) results from chemical weathering of minerals in the Sierra Nevada, with a low average $\delta^{44/40}$Ca. The primary flux of Ca out of Mono Lake is via calcareous tufa precipitation (F_{Tf}) and flux of carbonate to lake bottom sediment (F_{cs}). Total moles of dissolved Ca in Mono Lake are N_{Ca}, and Ca isotope fractionation during tufa precipitation is $\Delta^{44/40}Ca_{Tf}$.

tributary inflow based on an assessment of stream runoff entering Mono Lake between 1940 and 1989 (1.532×10^{11} L/yr) (Jones and Stokes, 1993).

Precipitation of carbonate minerals is the primary mode of calcium removal from the lake. The flux of Ca into carbonate minerals at the shoreline (into tufa) is denoted by F_{Tf}, while the flux of Ca from the water column to sediments on the modern lake bottom as aragonite and calcite particles is denoted by F_{cs}. Inorganic $CaCO_3$ makes up $\sim$ 4% of the lake bottom sediment fraction, and sediment accumulates at an average rate of 0.59 kg m^{-2} yr^{-1} (Li, 1995). Using the current lake area of $\sim 1.8\times10^8$ m^2, the rate of Ca sedimentation at the lake bottom is $F_{cs} = 1.72\times10^6$ kg Ca/yr. When the lake is at steady state with respect to calcium supply and removal ($F_{SN} = F_{cs} + F_{Tf}$), tufa precipitation must account for $\sim$ 22% of the Ca flux from Mono Lake.

We use isotopic mass balance to model the total calcium isotope variability of Mono Lake water between 1996 and 2010 following DePaolo (2004). The rate of change of $\delta^{44/40}Ca_{Lk}$ can be written as:

$$N_{Ca}\frac{d\delta^{44/40}Ca_{Lk}}{dt} = F_{SN}(\delta^{44/40}Ca_{SN} - \delta^{44/40}Ca_{Lk}) - F_{Tf}\Delta^{44/40}Ca_{Tf} - F_{cs}\Delta^{44/40}Ca_{cs}, \quad (4.4)$$

where N_{Ca} is the total moles of calcium in Mono Lake, and $\delta^{44/40}Ca_{Lk}$ and $\delta^{44/40}Ca_{SN}$ represent the calcium isotopic compositions of of Mono Lake water and Sierra Nevada stream water. Isotopic fractionation between tufa and lake water and between carbonate sediment and lake water are defined: $\Delta^{44/40}Ca_{Tf} = \delta^{44/40}Ca_{Tf}$ - $\delta^{44/40}Ca_{Lk}$, and $\Delta^{44/40}Ca_{cs} = \delta^{44/40}Ca_{cs}$ - $\delta^{44/40}Ca_{Lk}$. The variability of lake volume (LADWP, 2010) and concentration are known, so N_{Ca} may be determined as a function of time. For simplicity, the carbonate precipitation flux terms ($F_{Tf}\Delta^{44/40}Ca_{Tf}$ - $F_{cs}\Delta^{44/40}Ca_{cs}$) may be grouped into a single term ($F_C\Delta^{44/40}Ca_C$), which does not account for the various compositions of mixed lake and spring waters from which individual carbonates precipitate. The magnitude of the fractionation factor due to precipitation was assumed to be constant and representative of all carbonate mineral growth.

We modeled the recent calcium budget for Mono Lake by accounting for observed changes in lake water volume and calcium concentration (Fig. 4.3). To calculate the rate of change in calcium isotopic composition in a given year, calcium fluxes to and from the lake must be determined (Eq. 4.4). Assuming stream flow and evaporation constitute the primary influx and outflow of water to Mono Lake, the flux of stream water to the lake (F_s) may be determined from the expression,

$$\frac{dV}{dt} = F_s - F_{EV}, \tag{4.5}$$

where F_{EV} is the evaporative flux of water from the lake. The basin is assumed to maintain a constant F_{EV} of 1.7×10^{11} L/yr, which equates to 1.2 m of evaporation from the lake annually at its current volume. Estimates of evaporative flux from the lake range between 0.89 - 1.2 m/yr (Jones and Stokes, 1993). Change in lake volume with time is calculated from annual lake volumes reported by the LADWP. The fluxes of calcium to (F_{SN}) and from (F_C) the lake may be calculated from,

$$\frac{dN}{dt} = F_s c_s - F_C, \tag{4.6}$$

where c_s is the average concentration of calcium in stream water ($\sim$ 10 ppm; Tomascak et al., 2003) and $F_{SN} = F_s c_s$. The change in moles of calcium in lake water with time was determined from measured lake water calcium concentrations and reported lake volumes for each interval between concentration data points, and $\frac{dN}{dt}$ was assumed to be constant within each interval. The model fit was optimized using a $\Delta^{44/40}Ca_C$ value of -1.2 and a $\delta^{44/40}Ca_{SN}$ of 0.10 ‰. The fitted $\delta^{44/40}Ca_{SN}$ is somewhat higher than the calcium isotopic compositions of stream water reported in this study (Table 4.2), but it is considered reasonable given the simplicity and low temporal resolution of this model.

Between 2004 and 2005, the concentration of Ca in the lake abruptly plummeted. This distinctive event and the corresponding increase in $\delta^{44/40}$Ca of the lake may be explained by an abrupt carbonate mineral precipitation event. A rapid precipitation event occurring around 2004 is consistent with the breakdown of meromixis – persistent chemostratification of lake water – in 2003. Prior to 2003, the lake had not mixed since 1995 (Jellison and Roll, 2003), before our Ca isotope record begins. Breakdown of meromixis can promote a rapid precipitation event by mixing Ca-rich surface waters with Ca-depleted alkaline bottom waters

Table 4.3: Endmember spring and lake water isotopic compositions used to calculate the proportion of lake and spring water in solutions from which tufa precipitated. Steady state lake water was assumed to have an isotopic composition equal to the value measured in lake water with 4 ppm Ca. Endmember spring water was assumed to have a calcium concentration and isotopic composition identical to Tufa spring, and a strontium isotopic composition similar to northern spring water.

	[Ca] (ppm)	**[Sr]** (ppm)	$\delta^{44/40}$**Ca** (‰ BSE)	^{87}**Sr**/^{86}**Sr**
Lake water	4.20	0.032	1.12	0.70908(21)
Spring water	23.67	0.081	-0.48	0.70834(35)

and has been invoked to explain $CaCO_3$-rich horizons in lake bottom sediment (Newton, 1994).

In the absence of major stream flow variability or the onset of meromixis, the lake water should return to a steady state composition within 10 years, the current residence time of calcium in the lake.

Geochemistry of carbonate precipitation

Mixing and Fractionation

As noted above, the isotopic composition of Mono Lake water at the steady state Ca concentration of ∼4 ppm is 1.12 and $^{87}Sr/^{86}Sr$ = 0.70908(21) (1 s.d.). The average isotopic composition of tufa is $\delta^{44/40}$Ca = -0.30(21)and $^{87}Sr/^{86}Sr$ =0.70896(27). The $^{87}Sr/^{86}Sr$ of tufa samples is displaced by a small but significant amount from that of steady-state lake water, and in the direction of spring waters sampled near the tufa (Fig. 4.4). This accords with the inference that tufa forms in mixing zones between lake and spring waters.

Assuming tufa precipitation is driven by the mixing of lake water with un-depleted, Ca-rich spring water such as Tufa spring (Table 4.3), with a strontium isotopic composition representative of springs upwelling at the northern tufa (i.e. "depleted springs" with average $^{87}Sr/^{86}Sr$ = 0.70834(35)), the proportion of lake water in the mixed growth solution is approximately 90 % (Table 4.4; Fig. 4.6). The majority of strontium and calcium found in tufa, then, are likely derived directly from lake water. In addition, carbon and oxygen isotope analyses of tufa demonstrate that tufa CO_3^{2-} is derived entirely from lake water when compared with reported stream and lake water isotopic compositions (Li and Ku, 1997). The δ^{13}C and δ^{18}O of calcium carbonate in equilibrium with 2009 Mono lake water is nearly identical in composition to that of tufa, while that of stream water is vastly different (Table 4.5). The large variability of δ^{13}C throughout the lakes recent history (Li and Ku, 1997) can easily account for the large spread in δ^{13}C values of the tufa. Thus mixing between lake water and a small amount of spring water generates the Ca, Sr, C and O isotopic compositions of the tufa that we observe. This view contrasts the prevailing model for tufa genesis, which

Table 4.4: Ca isotope fractionation for a given solution stoichiometry during Mono Basin carbonate growth from mixed spring-lake water, using endmember compositions listed in Table 4.3. $\Delta^{44/40}$Ca values calculated assuming a lake water calcium isotopic composition equal to the 2009 average value (0.65(14)) and assuming a lake water calcium isotopic composition equal to the 1996 value (2.46) were also calculated and are the first and second values respectively listed in parentheses. Propagation of uncertainty for the isotopic compositions of the endmember fluids and carbonate minerals (0.15 ‰) yields an overall uncertainty for each $\Delta^{44/40}$Ca of 0.21 ‰ for a given endmember lake water calcium isotope composition.

Sample	**Fraction lake water**[a] (x)	**2 s.d.**	$a_{Ca^{2+}} : a_{CO_3^{2-}}$	**2 s.d.**	$\Delta^{44/40}$**Ca** [b] (‰)
Crust 1	0.470	0.031	1.326	0.142	-0.12 (-0.06, -0.31)
Crust 3	0.775	0.012	0.273	0.025	-0.38 (-0.20, -0.88)
Tufa 1	0.895	0.044	0.074	0.042	-0.56 (-0.29, -1.37)
Tufa 2	0.915	0.028	0.053	0.024	-0.98 (-0.67, -1.83)
Tufa 3	0.925	0.012	0.044	0.010	-1.01 (-0.69, -1.91)
Tufa 4	0.955	0.012	0.021	0.007	-1.11 (-0.75, -2.17)
Tufa 5	0.965	0.017	0.015	0.008	-1.09 (-0.72, -2.21)
Tufa 6	0.945	0.020	0.028	0.013	-0.96 (-0.61, -1.97)
Tufa 8	0.913	0.011	0.055	0.010	-0.92 (-0.63, -1.79)
Tufa 10	0.950	0.011	0.024	0.007	-1.13 (-0.78, -2.18)
Tufa 11	0.950	0.016	0.024	0.010	-1.08 (-0.73, -2.12)
LBS 1	1.000	0.003	0.001	0.001	-1.10 (-0.64, -2.44)
LBS 2	1.000	0.005	0.001	0.001	-1.20 (-0.74, -2.54)
LBS 3	0.835	0.003	0.158	0.004	-0.74 (-0.53, -1.38)
LBS 4	1.000	0.002	0.001	0.001	-1.75 (-1.29, -3.09)

(a) Calculated from the intersection of solid $^{87}Sr/^{86}Sr$ and the spring-Mono Lake water mixing line (Fig. 4.4).
(b) Calculated by difference between $\delta^{44/40}$Ca of solid and mixed water for a given strontium isotopic composition (Fig. 4.6).

Table 4.5: Carbon and oxygen isotopic compositions of Tufa and Crust carbonate. Mono Lake and Mono Basin stream water δ^{13}C compositions were taken from Li and Ku (1997). Reported δ^{18}O values for Mono lake and streams are Li and Ku (1997) water oxygen isotopic compositions equilibrated with calcite at 24°C.

Sample	δ^{18}**O** (‰ VPDB)	δ^{13}**C** (‰ VPDB)
Crust 3	-2.11	5.14
Tufa 3	-2.18	6.83
Tufa 4	-1.73	7.99
Tufa 5	-1.79	7.15
Tufa 6	-1.73	5.06
Tufa 8	-1.56	6.13
Tufa 10	-2.18	6
Mono Lake	-1.84	2
Streams	-15.91	-14

describes spring waters as the primary calcium source for $CaCO_3$ precipitation (e.g. Bischoff et al., 1993) .

To obtain a refined estimate of the Ca isotopic fractionation associated with the formation of tufa, we use the $^{87}Sr/^{86}Sr$ of each tufa sample to estimate the fraction of spring water present in the water from which it precipitated, and then calculate the $\delta^{44/40}$Ca of the mixed water. Endmember spring and lake water Sr and Ca compositions used in the isotopic budget are listed in Table 4.6. The calcium isotopic composition of a calcium-rich spring, Tufa spring, was used as the endmember spring $\delta^{44/40}$Ca with a value of -0.48 ‰. The $^{87}Sr/^{86}Sr$ representative of northern springs adjacent to sampled tufa, 0.70834(35), was used as the endmember spring strontium isotopic composition. Endmember lake water calcium has $\delta^{44/40}$Ca = 1.12 – the isotopic composition of steady state (4 ppm) lake water – and $^{87}Sr/^{86}Sr$ equal to the current lake water average value of 0.70908(21). We calculate the isotopic compositions of water mixtures from:

$$\delta_{tufa} = \frac{x_{spr} C_{spr} \delta_{spr} + (1 - x_{spr}) C_{Lk} \delta_{Lk}}{x_{spr} C_{spr} + (1 - x_{spr}) C_{Lk}}. \tag{4.7}$$

In this equation, C is concentration, δ is the isotopic composition ($^{87}Sr/^{86}Sr$ or $\delta^{44/40}$Ca), and x_{spr} is the mass fraction of spring water in the mixture.. A mixing line based on solutions of Eq. 4.7 for Sr and Ca is depicted as a dashed line in Fig. 4.6. The $\delta^{44/40}$Ca value of the water from which the tufa samples precipitated is estimated from the value given by this line for the $^{87}Sr/^{86}Sr$ value of the tufa. Fraction of lake water may also be calculated using this mixing relationship (Table 4.4). In general the water mixtures have lighter calcium isotopic compositions than lake water.

Calculated fractionation factors associated with tufa precipitation from mixed lake and spring water are presented in Table 4.4. The calcium isotopic composition of endmember

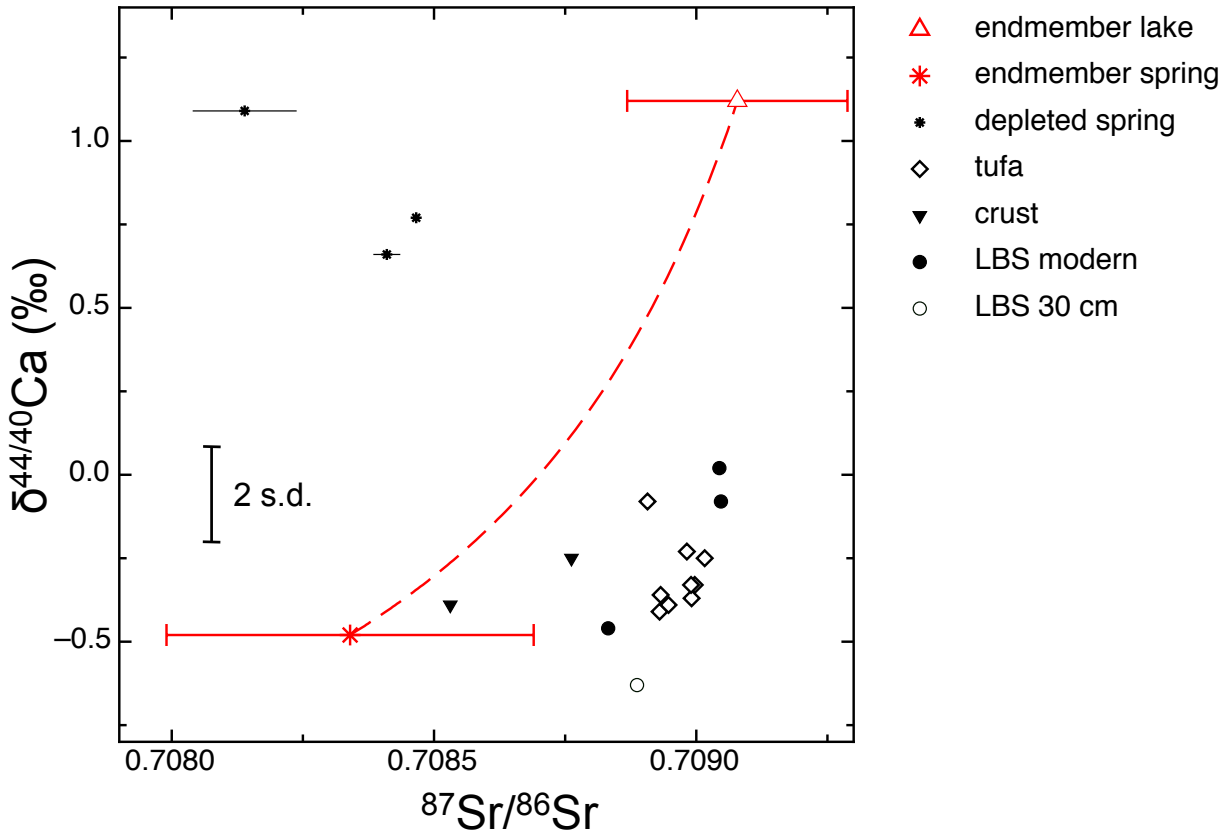

Figure 4.6: Detail of spring-lake water mixing to produce solid tufa carbonates and crusts. Endmember lake water has an average Sr isotopic composition of all lake waters analyzed (1996-2010), and the Ca isotopic composition of 4 ppm lake water (2005), which is thought to represent the steady state composition. Endmember spring water has an average Sr isotopic composition of depleted springs, which were sampled adjacent to tufa and therefore has an isotopic composition representative of local spring water. The Ca isotopic composition and concentration of Tufa spring, the highest Ca spring water analyzed, was assigned to the endmember spring water composition. Fractionation factors of tufa and crusts were calculated by subtracting the mixed isotopic composition at the appropriate $^{87}Sr/^{86}Sr$ from the measured solid $\delta^{44/40}Ca$.

Table 4.6: Concentrations of major dissolved constituents of Mono Basin fluids. Lake water composition reported here was sampled in the summer of 2010 at the same locale as LBS 2 listed above.

	Mono Lake (ppm)	**High-Ca Spring**[a] (ppm)
T (°C)	18.9	15
pH	9.8	6.5
Na	27273	132
K	1455	12
Ca[b]	4	23
Mg	37	37
Alkalinity[c]	30361	845
Cl	17345	44
SO_4	9885	36
SiO_2	16	81
PO_3	51	0

(a) Spring water composition from Bischoff et al. (1993), Table 4.1, Spring 3.
(b) Calcium concentration of lake water is assumed steady state value. Spring water is assumed to have the same concentration as Tufa spring.
(c) Alkalinity as ppm HCO_3.

lake water has a large influence on the calculated fractionation factor, so calculated $\Delta^{44/40}$Ca values for solid carbonates for alternate $\delta^{44/40}Ca_{Lk}$ are also given (Table 4.4). Although we believe the 2005 lake water calcium isotopic composition ($\delta^{44/40}Ca_{Lk}$ = 1.12) likely reflects the steady state value, alternate $\Delta^{44/40}$Ca values are presented to demonstrate the possible range of values. These were calculated based on the average 2009 (0.65(14)) and the 1996 (2.46) $\delta^{44/40}Ca_{Lk}$ values .

Assuming a $\delta^{44/40}Ca_{Lk}$ of 1.12, the water mixtures for lake water fractions relevant to tufa have $\delta^{44/40}$Ca values of $\sim$ 0.7, while the average tufa $\delta^{44/40}$Ca is $\sim$ -0.30(21). The calculated range of fractionation factors for precipitated tufa is $\Delta^{44/40}$Ca = -0.56(21) to -1.11(21). Shoreline crusts have a fractionation factor of $\Delta^{44/40}$Ca $\sim$ -0.12(21) to -0.38(21) relative to mixtures of lake and spring water. Aragonite in intermediate depth (15 m) lake bottom sediment (LBS 1) is 1.10(21) ‰ lighter than steady-state lake water, and the presence of a purely aragonitic sediment fraction is consistent with the sediment mineralogy reported by Li (1995). Calcite and aragonite from a deeper-water (36 m depth) lake bottom sediment sample (LBS 2) were slightly more fractionated than LBS 1 ($\Delta^{44/40}$Ca = -1.20(21)). The calculated fractionation factors are similar in magnitude to those found for both inorganic and biogenic calcium carbonate precipitation in natural and experimental settings (Gussone et al., 2003a; DePaolo, 2004; Lemarchand et al., 2004; Gussone et al., 2005; Tang et al., 2008a). The larger magnitude fractionation of the lake bottom carbonates is consistent

with the assumption that they precipitated directly from very low $a_{Ca^{2+}}$:$a_{CO_3^{2-}}$ lake water, inhibiting isotopic equilibration between the growing mineral surface and solution.

Phosphate inhibition and growth rate

Since the bulk of our Ca isotope data comes from measurements of tufa, tufa precipitation mechanisms must be assessed. Tufa accumulations are associated with the emergence of groundwater in the lake, hence the waters that they precipitate from are mixtures of high salinity lake water and low-salinity groundwater.

X-Ray diffraction of solid tufa samples and shoreline crusts reveal that tufa is primarily composed of aragonite, with lesser amounts of high- and low- magnesian calcite (Table 4.7). The saturation indices of these minerals were calculated as a function of water composition for mixtures of lake and high-Ca spring water (Table 4.6). The spring composition used in geochemical calculations was given the calcium concentration of Tufa spring, while the concentrations of all other major aqueous species were taken from Bischoff et al. (1993) (spring 3). The high Ca concentrations reported for the spring waters by Bischoff et al. (1993) are similar to those measured in shoreline springs by Neumann and Dreiss (1995) but were only observed in archived spring samples analyzed in this study (Table 4.2).

Calculations of solution speciation and saturation index (SI) were performed in CrunchFlow (Steefel, 2009). Saturation index is defined as $\log(\mathrm{IAP}/\mathrm{K}_{sp})$, where IAP is the ion activity product of constituent mineral ions defined above, and K_{sp} is the mineral solubility product. Calculated SI values demonstrate that the saturation index with respect to all constituent tufa calcium carbonate minerals decreases monotonically with the fraction of fresh water added to the lake water, even when Ca-rich waters enter the lake (Fig. 4.7a). This calculation demonstrates that the addition of Ca-rich groundwater does not significantly promote tufa precipitation, because the process does not increase SI. Although lake water is also supersaturated with respect to dolomite, dolomite is not observed in these samples possibly due to kinetic limitations.

Bischoff et al. (1993) invoke spring CO_2 degassing as the mechanism of raising mixed water saturation indices, but this mechanism is inconsistent with the discovery of carbonate mineral structures embedded in littoral sands many meters beneath the lake bed (Cloud and LaJoie, 1980). Degassing of freshwater is also inconsistent with the carbon and oxygen isotopic compositions of tufa compared with that of stream water (Table 4.5). Deposits of calcium carbonate crusts along the lakeshore, however, may be produced by CO_2 degassing resulting from wave action.

Using the same speciation calculations, the stoichiometry or $a_{Ca^{2+}}$:$a_{CO_3^{2-}}$ of mixed lake-spring solutions may be calculated. Carbonate mineral growth solutions with a large proportion of spring water (i.e. those forming shoreline crusts) have correspondingly high calcium to carbonate activity ratios, ranging from $\sim$1.3 to 0.3. Growth solution compositions calculated for tufa samples have intermediate solution stoichiometries from 0.02 to 0.07. Lake bottom sediment samples precipitated directly from lake water, with an extremely low $a_{Ca^{2+}}$:$a_{CO_3^{2-}}$

Table 4.7: Mineralogy of solid samples collected along the northern shore of Mono Lake, determined via x-ray diffraction. Most tufa samples are primarily aragonite with lesser magnesian calcite, calcite, quartz and evaporite minerals. Minerals are listed in order of decreasing abundance.

Sample	**Easting (m)**	**Northing (m)**	**Type**	**Mineralogy**
Crust 1	317300	4210496	Salt crust	Trona, Burkeite
Crust 3	318663	4212644	Salt crust	Calcite, Aragonite, Quartz, Halite
Tufa 1	317300	4210496	Tufa	Aragonite, Magnesian Calcite, Quartz
Tufa 2	317389	4210453	Tufa	Aragonite, Magnesian Calcite, Quartz
Tufa 3	317478	4210568	Tufa	Aragonite, Magnesian Calcite, Quartz
Tufa 4	317543	4210716	Tufa	Aragonite
Tufa 5	318705	4212994	Tufa	Aragonite, Halite
Tufa 6	318674	4212785	Tufa	Aragonite, Trona, Burkeite
Tufa 7	318714	4212789	Tufa	Aragonite
Tufa 8	318675	4212657	Tufa	Aragonite, Burkeite
Tufa 9	321800	4214941	Tufa	Magnesian Calcite, Halite
Tufa 10	321900	4214934	Tufa	Aragonite, Trona, Quartz, Calcite
LBS 1			Sediment	Quartz, Aragonite, Halite, Muscovite, Anorthite
LBS 2	323202	4203334	Sediment	Quartz, Albite, Calcite, Microcline, Aragonite
LBS 3	325380	4215900	Sediment	Quartz, Albite, Halite, Magnesian Calcite, Aragonite

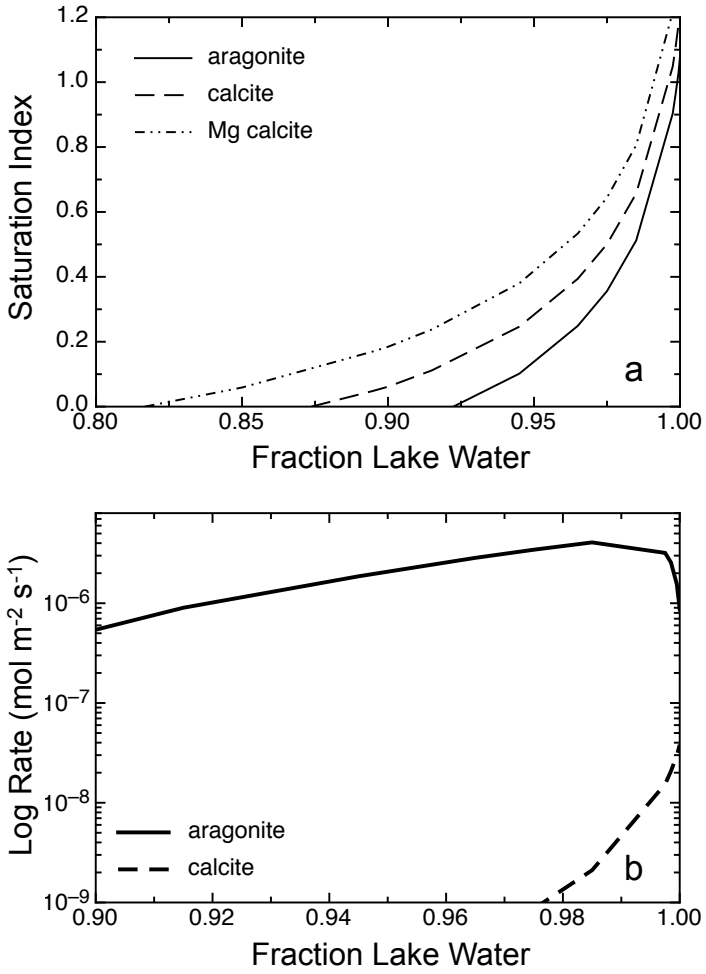

Figure 4.7: (a) Saturation index with increasing lake water fraction during mixing with Ca-rich spring water. Saturation index increases monotonically with % lake water, but observations indicate precipitation occurs during mixing of Mono Lake and spring water. (b) Precipitation rate calculated as a function of fraction lake water during mixing with typical high-Ca shoreline spring water. Spring water composition is based on Bischoff et al. (1993) with a calcium concentration equal to Tufa spring. Spring water addition negates the effects of phosphate inhibition on pure Mono Lake water.

of 0.001. Calculated calcium to carbonate activity ratios associated with each sample are listed in Table 4.4.

Orthophosphate inhibition is likely to be responsible for limiting carbonate precipitation directly from lake water. Phosphate is known to inhibit the precipitation of calcium carbonate minerals by forming inner-sphere complexes on actively precipitating surface sites (e.g. kinks) of nascent calcium carbonate nuclei and of growing layers (Dove and Hochella, 1993; Lin and Singer, 2006). The preservation of high lake water carbonate mineral supersaturation has been attributed to the high concentration of orthophosphate in Mono Lake (60 mg/L Bischoff et al., 1993). However, the effect of the changing orthophosphate concentrations associated with mixing between lake and spring water has not previously been considered. In the remainder of this section we evaluate the role of orthophosphate in tufa formation.

Burton and Walter (1990) derived an empirical relationship between phosphate concentration and speciation and calcium carbonate precipitation rate, from seawater. For aragonite,

$$log(R_p) = -6.96 - 1.19log([PO_4^{3-}]) + 1.63log(\Omega_c - 1), \tag{4.8}$$

Where R_p is precipitation rate in units of μmol m^{-2} h^{-1}, brackets denote aqueous concentration (mol/kg), and Ω_c is the oversaturation defined in terms of concentration ($[Ca^{2+}][CO_3^{2-}]/K_{sp}$). For calcite, the expression is:

$$log(R_p) = -6.50 - 1.18log(0.85[PO_4^{3-}] + 0.15[HPO_4^{2-}]) + 1.90log(\Omega_c - 1). \tag{4.9}$$

For our analysis, we use concentrations and water temperatures based on Bischoff et al. (1993), and account for the temperature difference of 5° versus 15°C between typical lake water and spring water, respectively. As a high ionic strength system, Mono Lake water is in many ways analogous to seawater, so we assume that the Burton and Walter empirical model is applicable here. The pH and solution chemistry dependence of precipitation rate, however, add additional uncertainty to the calculations (e.g. Zhang and Dawe, 1998).

The precipitation rates of aragonite and magnesian calcite calculated from Eqs. 3 and 4 are shown in Fig. 4.7b plotted against the fraction of lake water in a mixture of lake and spring water. The maximum aragonite precipitation rate is obtained for mixtures with 98% lake water. The calculated calcite precipitation rate is highest for pure lake water and decreases markedly with addition of spring water to rates that are about 1000 times slower than those for aragonite. This calculation shows clearly that aragonite is the preferred precipitate, which is consistent with the predominance of aragonite in tufa. In pure lake water, however, the calculation predicts that both calcite and aragonite should precipitate, although somewhat slowly. This latter result suggests that carbonate in the lake bottom sediments, which presumably does not precipitate in response to spring water addition, should have a larger proportion of calcite relative to aragonite in comparison with tufa. The carbonate mineralogy of Holocene lake bottom sediments deposited at water depths greater than 7 m is predominantly calcite, while aragonite dominates the carbonate fraction of shallow water core samples (Newton, 1994). In modern surface sediments, aragonite is

most abundant in sediments collected from water depths less than 18 m and is virtually absent from samples collected from depths greater than 20 m (Li, 1995). We propose that aragonite precipitates primarily in shallow lake waters due to mixing with fresh stream and spring water that spreads at the lake surface and then mixes downward.

Solution stoichiometry dependence of tufa fractionation

Currently, all previously reported Ca isotope fractionation between carbonate minerals and aqueous solution involve precipitation under conditions where $a_{Ca^{2+}} \gg a_{CO_3^{2-}}$. Mono Lake is different in that $a_{Ca^{2+}} \ll a_{CO_3^{2-}}$. The kinetics of calcite precipitation are strongly affected by $a_{Ca^{2+}}$:$a_{CO_3^{2-}}$ (Larsen et al., 2010), so it might be expected that Ca isotope fractionation could also depend on solution stoichiometry (Nielsen et al., 2012, chapter 2). When Ca ions predominate, as in ocean water where $a_{Ca^{2+}}$:$a_{CO_3^{2-}} \approx 200$, $CaCO_3$ growth rate could potentially be limited by transport of carbonate ions to the mineral surface, but probably not by transport of Ca ions. In high $a_{Ca^{2+}}$:$a_{CO_3^{2-}}$, kink sites at the $CaCO_3$ surface are predominantly occupied by calcium ions, facilitating exchange and isotopic equilibration with solution (Nielsen et al., 2012).

For Mono Lake, where $a_{Ca^{2+}}$:$a_{CO_3^{2-}} \approx 0.001$, it might be expected that transport of Ca ions could be limiting or that the kink composition of the growing mineral surface might affect calcium isotope partitioning. If diffusive transport of Ca in solution were rate-limiting for calcite or aragonite growth, the observed $\Delta^{44/40}$Ca would not be expected to exceed -0.45 ‰, the diffusive isotope separation of $^{44}Ca^{2+}$ and $^{40}Ca^{2+}$ ions (Bourg et al., 2010). Because the calculated fractionation factor of most carbonate minerals reported in this study exceeds this threshold value, we propose that the observed kinetic isotope fractionation is primarily surface-controlled.

Mono Basin carbonate mineral $\Delta^{44/40}$Ca and associated growth solution stoichiometry is plotted in Fig. 4.8. Carbonate crusts grown from solutions with a large proportion of spring water based on Sr isotopes, and a correspondingly high $a_{Ca^{2+}}$:$a_{CO_3^{2-}}$, have small-magnitude fractionation factors. Lake bottom sediments precipitated from pure lake water with a very low $a_{Ca^{2+}}$:$a_{CO_3^{2-}}$have the largest magnitude fractionation factors observed in this study. Tufa samples span a large intermediate range of lake-spring water mixing proportions, and these are consistent with a decreasing magnitude fractionation factor with increasing proportion of low $^{87}Sr/^{86}Sr$ spring water. By invoking a solution-stoichiometry dependent surface controlled carbonate mineral precipitation, the relationship between calcium isotope fractionation and solution stoichiometry may be modeled.

A model for solution composition-dependent Ca isotope fractionation during calcite precipitation was presented in chapter 2, that accounts for the effects of both supersaturation and solution stoichiometry. Assuming ion i (Ca^{2+} or CO_3^{2-}) with solution activity a_i attaches to the mineral surface at kink sites with attachment frequency $k_i a_i$ and detachment frequency ν_i, growth rate may be expressed in terms of the activities of Ca^{2+} and CO_3^{2-} in solution and elementary coefficients of attachment and detachment k_i and ν_i. Net isotopic fractionation factor α_p the calcium isotopic fractionation factor during precipitation may

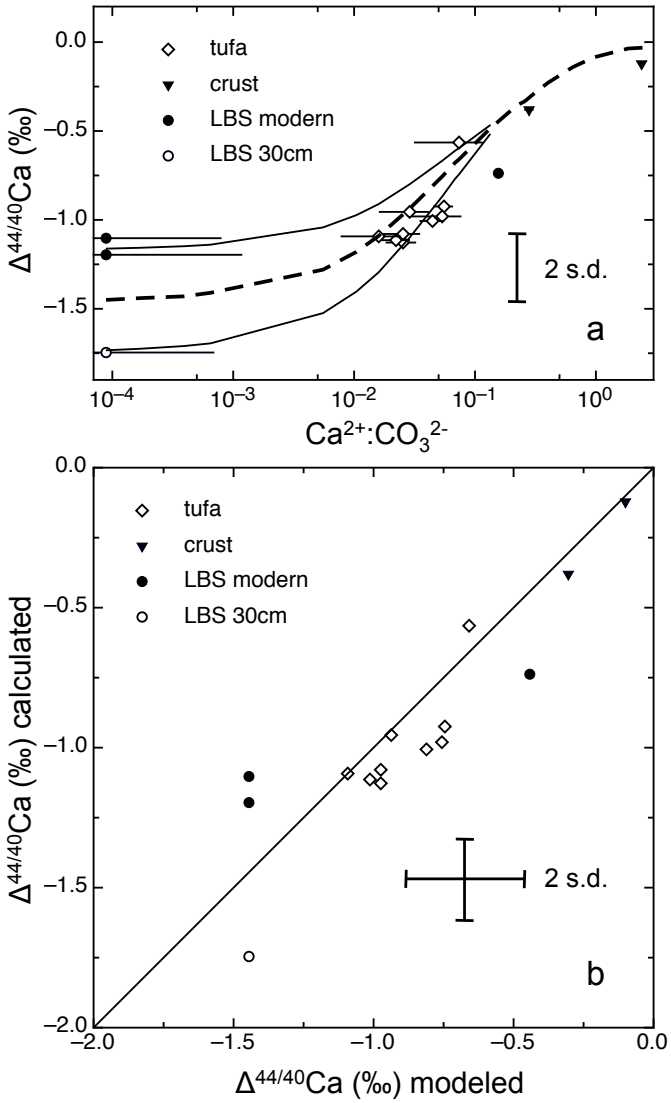

Figure 4.8: (a) Model fit to Mono carbonate $\Delta^{44/40}$Ca calculated from Eq. 4.10 using $k_{Ca^{2+}}$, $k_{CO_3^{2-}}$, $\nu_{Ca^{2+}}$, and $\nu_{CO_3^{2-}}$ fitted to Larsen et al. (2010) step velocities in Nielsen et al. (2012). Activities of calcium and carbonate were calculated based on mixing of endmember spring and lake water compositions (Table 4.3) at varied proportions. The $a_{Ca^{2+}}$:$a_{CO_3^{2-}}$ dependence of Ca isotope fractionation of carbonate precipitation assuming a -0.4 ‰ equilibrium fractionation factor and -1.5 ‰ (dashed line), -1.2 ‰ (top solid line) and -1.8 ‰ (bottom solid line) kinetic fractionation factors for precipitation (dashed line). Solution stoichiometry for each sample was determined from the fraction lake water extracted from the Sr-Ca mixing line (Figure 4). LBS modern and LBS 30cm were taken from the same core and correspond to samples LBS 2 and LBS 4 in Table 4.2. (b) Modeled vs. calculated fractionation factor during precipitation corresponding to the -1.5 ‰ kinetic endmember fractionation factor, with the 1:1 line drawn to guide the eye.

be expressed:

$$\alpha_p = \frac{\alpha_f k_{Ca^{2+}} a_{Ca^{2+}} P_{CO_3^{2-}}}{k_{Ca^{2+}} a_{Ca^{2+}} P_{CO_3^{2-}} + \nu_{Ca^{2+}} P_{Ca^{2+}} (\frac{\alpha_f}{\alpha_{eq}} - 1)} \tag{4.10}$$

where α_f is the kinetic endmember fractionation factor, α_{eq} is the equilibrium calcium isotope fractionation factor between $CaCO_3$ and solution, P_{Ca} is the probability that a given kink site is occupied by calcium, and P_{CO_3} is the probability that a kink site is occupied by carbonate. Fractionation factor α_p is equivalent to the ratio of $^{44}Ca/^{40}Ca$ in the solid divided by the ratio of $^{44}Ca/^{40}Ca$ in the fluid. Kink site probabilities may be expressed in terms of elementary exchange coefficients and the activities of calcium and carbonate in solution:

$$P_{Ca^{2+}} = \frac{k_{Ca^{2+}} a_{Ca^{2+}} + \nu_{CO_3^{2-}}}{k_{Ca^{2+}} a_{Ca^{2+}} + \nu_{CO_3^{2-}} + k_{CO_3^{2-}} a_{CO_3^{2-}} + \nu_{Ca^{2+}}} \tag{4.11}$$

and

$$P_{CO_3^{2-}} = \frac{k_{CO_3^{2-}} a_{CO_3^{2-}} + \nu_{Ca^{2+}}}{k_{Ca^{2+}} a_{Ca^{2+}} + \nu_{CO_3^{2-}} + k_{CO_3^{2-}} a_{CO_3^{2-}} + \nu_{Ca^{2+}}} \tag{4.12}$$

We modeled calcium isotope fractionation corresponding to the range in calcium and carbonate activities obtained by mixing endmember lake and spring waters (Tables 4.3 & 4.6) using elementary exchange coefficients fitted to Larsen et al. (2010) obtuse step velocities (Nielsen et al., 2012), an equilibrium fractionation factor of -0.4 ‰ and a kinetic endmember fractionation factor of -1.50 ‰. Isotope fractionation as a function of solution stoichiometry of Mono Basin carbonate minerals is plotted in Fig. 4.8, alongside the fitted model curve. The magnitude of fractionation factor calculated for Mono Basin carbonates decreases with increasing $a_{Ca^{2+}}$:$a_{CO_3^{2-}}$, in good agreement with the modeled trend.

The $\Delta^{44/40}Ca$ values measured in the Mono Lake system exceed the limiting fractionation factor characteristic of diffusive transport limit by about 0.5 ‰, so transport cannot be the sole controlling factor determining the Ca isotope fractionation factor. However, the relatively slower diffusive transport of ^{44}Ca to the mineral surface could cause the surface aqueous $^{44}Ca/^{40}Ca$ to be lower than in bulk solution. This affect would tend to increase α_p, decreasing the magnitude of $\Delta^{44/40}Ca$, so that the full fractionation that would apply in a well-stirred or rapidly flowing fluid would not be observed. Overall, considering the likely uncertainties in our estimates of growth solution composition, the Mono Lake data conform to the model well, and the tentative conclusion is that the theoretically-predicted solution stoichiometry dependence of Ca isotope fractionation is in fact observed in this natural system. Nevertheless, because our calculated aragonite fractionation factors (-0.56 to -1.13 ‰; Table 4.4) are smaller than previously-measured values from experiments (-1.4 to -1.8 ‰; Gussone et al., 2003a, 2005), there is a possibility that Mono Basin carbonate mineral growth is partially diffusion limited.

4.5 Summary and conclusions

The Mono Lake carbonate cycle contrasts with the marine cycle in that it has high pH, low aqueous Ca concentration, and very low $a_{Ca^{2+}}$:$a_{CO_3^{2-}}$. We investigated the Ca isotope composition of Mono Lake waters, inflowing streams and springs, and precipitated carbonate minerals to determine whether $a_{Ca^{2+}}$:$a_{CO_3^{2-}}$ affects the Ca isotope fractionation during carbonate mineral precipitation. The carbonate system in Mono Lake, which is a closed basin lake, works much like the marine cycle in that the $\delta^{44/40}$Ca of the dissolved Ca in the lake is displaced to higher values relative to that of the dissolved Ca in streams supplying the lake, due to the influence of Ca isotope fractionation during removal of dissolved Ca by carbonate mineral precipitation.

The isotopic fractionation of Ca during precipitation, $\Delta^{44/40}$Ca, can be estimated by comparing the $\delta^{44/40}$Ca of tufa and lake bottom sedimentary carbonate to the average $\delta^{44/40}$Ca of Mono Lake water. There is uncertainty associated with this comparison because the lake is a dynamic system that is subject to both natural variations and human disturbances, and the ages of tufa and lake bottom sediment samples are not known precisely. The residence time of Ca in the lake is only about 10 years, and there is spatial variation in the calcium isotopic composition of Mono Lake water of about 0.4 ‰, and temporal variation of about 2.5 ‰. Nevertheless, we observe that the $\delta^{44/40}$Ca of carbonate minerals is consistently lower than that of the lake water by up to 1.75(21) ‰. This observation, combined with the observation that the lake water $\delta^{44/40}$Ca is higher than the average stream $\delta^{44/40}$Ca by about 1.11(21) ‰, indicates that the average value of $\Delta^{44/40}$Ca for carbonate precipitation in Mono Lake must be about -1.1 ‰ to reach a steady state, which is consistent with the $\Delta^{44/40}Ca_{Tf}$ values calculated from mixing (Table 4.4). Diffusive Ca transport to the mineral-aqueous interface does not appear to control Ca isotope incorporation into the bulk mineral, because the fractionation factor exceeds the diffusive transport limit of $\sim$ 0.5 ‰.

The observed $\Delta^{44/40}Ca_{Tf}$ falls within the range of isotopic fractionation factors observed in natural marine aragonite and inorganically precipitated carbonates at similar temperatures. Our results show that the magnitude of isotopic fractionation depends strongly on the ratio of Ca^{2+} to CO_3^{2-} of the mixed growth solution from which the carbonates grew. Carbonates precipitated near-shore from Ca-rich solutions with Sr isotopic compositions similar to spring water have small magnitude $\Delta^{44/40}$Ca values, while carbonates that precipitated directly from high alkalinity, low-Ca lake water have the largest magnitude $\Delta^{44/40}$Ca values. The observed relationship between calcium isotope fractionation and solution stoichiometry may be modeled using the theory developed in chapter 2.

Our results support the hypothesis that Ca isotope fractionation during precipitation of carbonate minerals from aqueous solution is controlled by the kinetics of ion attachment and detachment fluxes at the mineral aqueous interface and depends on $a_{Ca^{2+}}$:$a_{CO_3^{2-}}$. Because kinetic processes affect isotopic and trace element incorporation into precipitated carbonate minerals, using Ca isotopes to reconstruct paleo-seawater isotopic composition (e.g. Farkaš et al., 2007; Fantle and DePaolo, 2007) in general requires knowledge of precipitation rate, the stoichiometry of the growth solution and potentially other factors as well. This clearly

complicates the application of isotopes for seawater reconstruction, but this type of complication is not new – it is well known that non-equilibrium effects (i.e. kinetic or vital effects) are important and large and must be accounted for in paleo-environmental reconstructions with C and O isotopes (e.g. Zachos et al., 2001). Understanding the controls on Ca isotope fractionation will bring new insights about kinetic processes controlling the isotopic composition of carbonate minerals.

Chapter 5

Co-dependent calcite growth kinetics, inhibition and impurity uptake

5.1 Introduction

Impurity ions and ionic molecules are widely known to inhibit the growth and alter the composition of carbonate minerals precipitating from aqueous solution (Meyer, 1984; Burton and Walter, 1990; Cabrera and Vermilyea, 1958; Davis et al., 2000b; Reddy and Hoch, 2000; Wasylenki et al., 2005b,a; Lin and Singer, 2006). Interpretation and use of trace element signatures for paleoclimate reconstruction, retardation of contaminant transport (Lukashev, 1993), and preventing pipe scaling require an understanding of controls on impurity incorporation during carbonate mineral growth. Despite the widespread use of trace element signatures, the nonlinear effects of certain trace elements, such as strontium, on calcite precipitation rate have largely eluded explanation (Wasylenki et al., 2005b). No single theory has described growth inhibition by both the kink pinning and incorporation inhibition mechanisms simultaneously. Although significant advances have been made in atomic-scale understanding of growth (Zhang and Nancollas, 1990; Teng et al., 1998; Zhang and Nancollas, 1998; Teng et al., 1999, 2000), crude rate equation and trace element partitioning models are still empirically based. While most rate equation based analyses ignore the feedbacks between ion incorporation and mineral growth kinetics, impurity uptake affects subsequent growth kinetics and should therefore be treated explicitly.

By accounting for the molecular mechanisms of growth inhibition at the mineral aqueous interface, we derive widely-applicable expressions relating solution composition to precipitation rate and crystal composition. In the case of non-incorporating impurities, these may be solved analytically, while in the nonlinear case of trace element incorporation, numerical solution is required.

5.2 Underlying mechanisms and governing equations

The net flux of ions to the mineral surface governs the composition and growth kinetics of precipitating minerals. At ambient temperature and supersaturations not exceeding the solubility of amorphous calcium carbonate (ACC), ion incorporation into calcite occurs primarily at kink sites along step edges at the mineral aqueous interface (DeYoreo et al., 2009; Larsen et al., 2010; Nielsen et al., 2012). Overall growth occurs when the net rate of ion attachment at kink sites exceeds the net rate of ion detachment, and the relative rates of constituent ion and trace element incorporation control the bulk mineral composition (DePaolo, 2011; Nielsen et al., 2012). Calcite precipitation from aqueous solution may be described by the creation-propagation-collision (CPC) model, where kink sites are created by the formation of stable 1D nuclei along the step, and propagate parallel to the step until they are annihilated by collision with a kink moving in the opposite direction (Zhang and Nancollas, 1990, 1998; Larsen et al., 2010).

Inhibition of calcite growth may be caused by either 1) blocking of kink sites by an ion or molecule (Elhadj et al., 2006; Harstad and Stipp, 2007), or 2) incorporation of trace ions or molecules which alter the mineral solubility via solid solution formation (Davis et al., 2000a,b). Kink blocking by strong-adsorbing aqueous species will cause an exponential decrease in mineral precipitation rate with increasing impurity concentration, consistent with classical growth inhibition theory (Cabrera and Vermilyea, 1958) and with Langmuir-type inhibitor adsorption (Weaver et al., 2010). Growth inhibition by the incorporation of trace species into the bulk lattice may vary in functional form, depending on the thermodynamics of solid solution formation and the rates of trace ion incorporation relative to the constituent ions. Divalent cations of Fe, Cu, Mg, Sr, Mn are known to be incorporated into the calcite structure, and all inhibit growth at sufficiently high concentrations.

Governing equations

The net rate of ion attachment to kink sites (s^{-1}) is defined by

$$u_i = k_i(i)P_j - \nu_i P_i \tag{5.1}$$

for ion i attaching to a j-type kink site, where (i) is the ion activity in solution, k and ν are the ion attachment ($s^{-1}M^{-1}$) and detachment (s^{-1}) rate coefficients respectively, and P_i is the probability of a given kink site being an i site Zhang and Nancollas (1990). We note that rate coefficients of attachment and detachment can be cast in terms of fluxes following,

$$k_i = \phi e^{-E_A/k_b T}, \tag{5.2}$$

where ϕ represents a flux due to Brownian collisions, E_A is the activation energy barrier for reaction (J/mol), k_b is the Boltzmann constant (J mol^{-1} K^{-1}), and T is temperature (K). However, this level of detail is not currently useful given our limited understanding of the energy landscape of relevant reactions. It is thought that coefficients of attachment are

dominantly controlled by the kinetics of ion or kink site desolvation, and to some extent by steric effects. Attachment of calcium ions to carbonate kink sites is likely limited by the rate of calcium desolvation, while the rate of carbonate ion attachment may be limited by the rate of calcium kink dehydration (Larsen et al., 2010). Detachment rate coefficients are controlled by the affinity of ions for the crystal surface, which is independent of site type along the step (Zhang and Nancollas, 1990, 1998; Elhadj et al., 2006).

In the case of a trace impurity interacting with the growing calcite surface, the attachment kinetics of calcium ion (denoted by A), carbonate ion (denoted by B), and impurity (denoted by M) ions control growth rate. To determine net ion attachment fluxes and therefore growth rate and overgrowth composition, the proportion of kink sites (P_A, P_B, and P_M) must be known. Three constraint equations are required to solve for the probabilities of A, B and M kink sites, where M is assumed to attach to carbonate ions and substitute for calcium ions. To preserve crystal stoichiometry, one B ion must attach for each A and M ion. It follows that:

$$u_A = u_{B-A}, \tag{5.3}$$

and

$$u_P = u_{B-M}, \tag{5.4}$$

where u_{B-i} is the net frequency of B attachment to i. Three types of kink sites are defined, so

$$P_A + P_B + P_M = 1. \tag{5.5}$$

Once kink probabilities and ion attachment frequencies have been determined, the overall growth rate may be calculated from the net ion attachment frequency ($u_{net} = u_A + u_B + u_P$) following

$$R = \frac{\rho u_{net} hbd}{2y_0} = \frac{v_{st} bd}{y_0} \tag{5.6}$$

where ρ is the kink density, h is the step height (m), b is kink depth (m), d is mineral density (mol/m^3), y_0 is terrace width, and v_{st} (m/s) is the step velocity (chapter 1; Teng et al., 1998; Zhang and Nancollas, 1998; Nielsen et al., 2012). Terrace width may be written,

$$y_0 = \frac{8\Gamma hab\alpha}{k_b T\sigma}, \tag{5.7}$$

where a (m) is molecular unit width along the step, Γ is approximately 1 for calcite, σ is supersaturation ($= \ln(\mathrm{IAP}/\mathrm{K}_{sp})$, α (J/m^2) is step edge free energy per unit step height, k_b (J/mol) is the Boltzmann constant, and T (K) is temperature (Teng et al., 1998).

Kink density, ρ, is given by the expression,

$$\rho = \sqrt{\frac{2I}{u_{net}}}, \tag{5.8}$$

where I is the stable 1D nucleation rate. I may be approximated by,

$$I = P_0\left(\frac{k_A(A)}{\Omega_A} + \frac{k_B(B)}{\Omega_B}\right), \tag{5.9}$$

where Ω_A and Ω_B represent resistance to A and B kink nucleation, and P_0 is the probability that a given site along the step is a non-kink site ($P_0 = 1 - \rho$), and the two terms in parentheses are the rates of stable nucleation for A and B ions (Zhang and Nancollas, 1998). Assuming stable 1D nuclei ultimately grow to infinite length, resistance to A nucleation may be expressed,

$$\Omega_A = 2 + \left(\frac{\nu''_A}{k_B(B)} + \frac{\nu''_A}{k_A(A)} \frac{\nu_B}{k_B(B)} \right) \times \left(1 - \frac{\nu_A \nu_B}{k_A(A) k_B(B)} \right)^{-1}, \tag{5.10}$$

where the detachment frequencies of single ions adsorbed to the step with kink formation energy ϵ (J mol^{-1} K^{-1}) may be expressed $\nu''_A = \nu_A e^{2\epsilon/kT}$ and $\nu''_B = \nu_B^{2\epsilon/kT}$ (Zhang and Nancollas, 1998). Upon substitution of Eq. 5.9, Eq. 5.8 simplifies to

$$\rho = \sqrt{(1-\rho) \times C}, \tag{5.11}$$

where

$$C = \frac{2}{u_{net}} \left(\frac{k_A(A)}{\Omega_A} + \frac{k_B(B)}{\Omega_B} \right). \tag{5.12}$$

Kink probability ρ may be determined by solving Eq. 5.11 using the quadratic equation.

To calculate precipitation rate, kink formation energy (ϵ/k_bT) must be known. The value of this parameter may be obtained from measurements of equilibrium kink spacing. DeYoreo et al. (2009) determined a near-equilibrium kink spacing for calcite of ∼5-7 molecular unit widths. Equilibrium kink spacing (L_{eq}= $1/\rho_{eq}$) for a given value of kink formation energy may be calculated by substituting the 1D nucleation rate (Eq. 5.9) and net kink propagation rate into Eq. 5.8, setting (A) and (B) equal to the equilibrium activities of calcium and carbonate ions in solution ($\sqrt{K_{sp}}$). In this calculation, we use the attachment and detachment rate coefficients fitted to Larsen et al. (2010) obtuse step velocities , which may be found in Nielsen et al. (2012). An ϵ/k_bT corresponding to the observed spacing is approximately equal to 2.8. The calcite kink formation energy may also be estimated using the BCF expression for equilibrium kink spacing:

$$L_{eq} = 1 + (1/2)e^{\epsilon/k_bT} \tag{5.13}$$

(Burton et al., 1951; Chernov et al., 2004). If we assume that $L_{eq} = 7$, we find that ϵ/k_bT estimated in this way is equal to 2.5, which is similar to our calculated value. These estimates of kink formation energy factor are significantly smaller than a prior estimate of ϵ/k_bT = 7.775 (Larsen et al., 2010) based on molecular simulation (Kristensen et al., 2004), which corresponds to an equilibrium kink spacing of 842 molecular unit widths.

Non-incorporating impurities

The strong specific adsorption of ions to kink sites on the calcite surface may inhibit growth by preventing the subsequent attachment of constituent calcium or carbonate ions.

This class of inhibitors presumably includes large molecules such as polyaspartate (Elhadj et al., 2006) and citrate (DeYoreo et al., 2009) that bind strongly to kink sites but do not fit into the calcite lattice. In this case, the net impurity attachment rate is negligible ($u_M = u_{B-M} = 0$), so kink probabilities may be determined analytically by solving Eqs. 5.3-5.5 using Eq. 5.1. The kink site probabilities are given by

$$P_A = \frac{\nu_M[k_A(A) + \nu_B]}{\nu_M[k_A(A) + k_B(B) + \nu_A + \nu_B] + k_M(M)[k_B(B) + \nu_A]}, \tag{5.14}$$

$$P_B = \frac{\nu_M[k_B(B) + \nu_A]}{\nu_M[k_A(A) + k_B(B) + \nu_A + \nu_B] + k_M(M)[k_B(B) + \nu_A]}, \tag{5.15}$$

and

$$P_M = \frac{k_M(M)[k_B(B) + \nu_A]}{\nu_M[k_A(A) + k_B(B) + \nu_A + \nu_B] + k_M(M)[k_B(B) + \nu_A]}, \tag{5.16}$$

which depend solely on the rate coefficients for ion attachment and detachment frequencies (k and ν) and ion activities in solution. The affinity of impurity ions for kink sites will control the kinetics of impurity ion detachment (Elhadj et al., 2006) and thus the efficiency of kink blocking.

Rate coefficients of ion exchange at kink sites k and ν control net ion attachment fluxes and thus the overall precipitation rate. For pure calcite growing in the presence of a kink-blocking impurity, the values for k_A, k_B, ν_A and ν_B may be constrained by the solubility of calcite. At equilibrium, the net attachment fluxes of A and B must be zero. Setting u_A and $u_B = 0$, from 5.1 we find,

$$(A)_{eq} = \frac{\nu_A P_A}{k_A P_B}, \tag{5.17}$$

and

$$(B)_{eq} = \frac{\nu_B P_B}{k_B P_A}. \tag{5.18}$$

The solubility of an AB mineral is equal to the product of equilibrium ion activities, $K_{AB} = (A)_{eq}(B)_{eq}$, so

$$K_{AB} = \frac{\nu_A \nu_B}{k_A k_B}. \tag{5.19}$$

If the rate coefficients of attachment and detachment are equal for ions A and B ($k_A = k_B = k$ and $\nu_A = \nu_B = \nu$), only one fitted parameter is sufficient to determine both k and ν

$$\nu = \sqrt{K_{AB} k^2}. \tag{5.20}$$

The dependence of calcite growth rate on non-incorporating impurity concentration may be solved following the procedure detailed in Appendix D.1.

Incorporation inhibition

Precipitation of calcite from natural aqueous fluids leads to the incorporation of trace, non-constituent ions, which affect mineral growth kinetics and composition. Divalent ions of metals including iron (Katz et al., 1993), copper (Parsiegla and Katz, 1999), cadmium, barium (Tesoriero and Pankow, 1996), magnesium (Plummer and Busenberg, 1987; Davis et al., 2000a,b), strontium (Tesoriero and Pankow, 1996; Gabitov and Watson, 2006), and manganese have been shown to co-precipitate with calcite and to subsequently affect growth rate. Anions including sulphate (Flaathen et al., 2011), phosphate, and uranyl may also be sparingly incorporated into the calcite lattice. In general, increased impurity loading and uptake leads to decreased growth rate (e.g. Meyer, 1984), but in some cases, small amounts of impurity may speed crystallization kinetics (Wasylenki et al., 2005b).

Several models have been proposed to describe the relationship between growth rate and impurity uptake in calcite. Decreased precipitation rate with increasing tracer concentration is generally attributed to a kink blocking mechanism (Wasylenki et al., 2005b) or to increased mineral solubility (Davis et al., 2000) or a combination of both. In the latter case, the overall solubility of the $M_xCa_{1-x}CO_3$ solid solution is invoked to explain the decrease in growth rate. No model has successfully captured the effect of strontium incorporation on calcite precipitation rate (Wasylenki et al., 2005b), and most models describe qualitative behavior without allowing direct calculation of predicted growth rates and partition coefficients as a function of solution composition.

We model calcite growth kinetics and composition during precipitation in the presence of impurities using a CPC approach. Net ion attachment rates are determined numerically based on the constraint equations 5.3-5.5. Following Eq. 5.1, the net rate of B ion attachment to A kink sites is expressed,

$$u_{B-A} = k_B(B)P_A - \nu_B P_{B-A}, \tag{5.21}$$

where $P_{B-A} = P_B(1-x)$ is the probability that a carbonate kink site sits adjacent to a calcium along the step, with mole fraction $CaCO_3$ in the solid solution of $(1-x)$. An analogous expression may be written for the net rate of B ion attachment to kink sites occupied by impurities,

$$u_{B-M} = k_{B-M}(B)P_M - \nu_{B-M}P_{B-M}, \tag{5.22}$$

where $P_{B-M} = P_B x$. Carbonate ions may attach to and detach from calcium and impurity kink sites with different frequencies, so the rate coefficients of B ion reaction with A sites may not equal those of B ion reaction with M sites ($k_{B-M} \neq k_B$ & $\nu_{B-M} \neq \nu_B$). The ratio of impurity to calcium in the crystal (r_x) during steady state crystal growth is equal to the ratio of net impurity and calcium ion attachment rates,

$$r_x = u_M/u_A, \tag{5.23}$$

which is related to the mole fraction of the impurity carbonate by the following relation,

$$x = \frac{r_x}{1+r_x}. \tag{5.24}$$

Thermodynamics of metal carbonate solid solutions

During the formation of a solid solution between impurity carbonate and calcite, the affinity of ions for kink sites imposes a control on the rate of ion detachment from those sites. The solubility of each solid solution component constitutes a measure of this affinity and may therefore be used to calculate ion detachment frequency ν. Specifically, the detachment frequency of a given ion will depend upon the ion activity of the corresponding endmember component in equilibrium with the specific solid solution phase, $M_xA_{1-x}B$, where x is the impurity carbonate mole fraction in the solid solution.

The thermodynamics of metal carbonate solid solution formation is effectively captured by Lippmann diagrams, which portray the thermodynamic relationship between a specific solid solution phase and aqueous solution. We refer the reader to Glynn and Reardon (1990) and Gamsjäger et al. (2000) for a comprehensive discussion of Lippmann diagrams.

In the Lippmann construct, the total solubility of a solid solution phase with mole fraction of the impurity carbonate equal to x is defined by the "solidus" equation, which for a metal impurity (M) calcium carbonate, $M_xA_{1-x}B$, may be expressed:

$$\Sigma\Pi = K_{AB}a_{AB} + K_{MB}a_{MB}, \tag{5.25}$$

where $a_{AB} = \gamma_{AB}(1-x)$ and $a_{MB} = \gamma_{MB}x$ are the solid endmember activities with activity coefficients γ, and K_{AB} and K_{MB} are the AB and MB solubilities (Glynn and Reardon, 1990). For a given solution, total solubility is equivalent to the sum of endmember component equilibrium ion activity products,

$$\Sigma\Pi = (A)_{eq}(B)_{eq} + (M)_{eq}(B)_{eq}. \tag{5.26}$$

The composition of the aqueous solution at equilibrium with this solid solution phase, y, may be determined from the solutus equation for non-ideal solid solutions (Glynn and Reardon, 1990):

$$\Sigma\Pi = \left(\frac{y}{K_{MB}\gamma_{MB}} + \frac{1-y}{K_{AB}\gamma_{AB}}\right)^{-1}, \tag{5.27}$$

where y is related to equilibrium aqueous solution composition by:

$$y = \frac{(M)_{eq}(B)_{eq}}{(M)_{eq}(B)_{eq} + (A)_{eq}(B)_{eq}}. \tag{5.28}$$

At equilibrium, the ion activity products of AB and MB may be expressed in terms of solid activities or in terms of total solubility ($\Sigma\Pi$) and y,

$$(A)_{eq}(B)_{eq} = (1-x)K_{AB}\gamma_{AB} = \Sigma\Pi \times (1-y), \tag{5.29}$$

and

$$(M)_{eq}(B)_{eq} = xK_{MB}\gamma_{MB} = \Sigma\Pi \times y. \tag{5.30}$$

If the relationship between γ_{AB}, γ_{MB} and the mole fraction of MB in the solid solution (x) is known, the equilibrium activities of A, B and M (calcium, carbonate, and trace metal) ions may be calculated.

Solubility controls on detachment kinetics

The net attachment fluxes of A, B and M must equal zero at equilibrium, so equations for u_A, u_B, u_{B-A} and u_{B-M} (Eqs. 5.1, 5.21, and 5.22) may be reorganized to solve for $(A)_{eq}$, $(B)_{eq}$ and $(M)_{eq}$. Combining these expressions with Eqs. 5.29 and 5.30, the product of ion detachment frequencies for solubilities as a function of the equilibrium ion activity becomes,

$$\nu_A \nu_B = \frac{(A)_{eq}(B)_{eq} k_A k_B}{1 - x}, \tag{5.31}$$

and

$$\nu_M \nu_{B-M} = \frac{(M)_{eq}(B)_{eq} k_M k_{B-M}}{x}. \tag{5.32}$$

The exact form of solid activity coefficients varies among trace elements, so the effect of impurity incorporation on detachment frequencies and overall growth kinetics may differ. Increasing the activity coefficient of either solid solution endmember component will result in an increased frequency of detachment for its ionic constituents. Variation in ion detachment frequencies is mechanistically related to the effects of lattice strain on bond strength during the incorporation of ions of different sizes. Increasing detachment frequency reflects decreasing affinity of an ion for its kink site.

To minimize the number of parameters, we have assumed that impurity ions in positions other than the currently propagating step do not affect attachment frequencies. Astilleros et al. (2010) observed that the steps propagating across the original, pure calcite substrate maintained higher step velocities than those propagating across the magnesian calcite overgrowth, so this assumption is not strictly valid. However, this affect is transient, and the step velocities reach steady state within a few minutes. The model in its current form captures the primary co-dependencies of growth rate and trace element incorporation; it would be straightforward to add additional complexity once the rate coefficients of ion attachment to and detachment from different types of kink sites are experimentally or computationally accessible.

Partition coefficients

The steady state growth rate and solid solution composition corresponding to a given (A), (B) and (M) may be determined by numerically solving the nonlinear system of equations 5.3-5.5 and 5.21-5.24 (see Appendix D.2 for further detail). With r_x it is trivial to calculate the observed partition coefficient,

$$K_p = \frac{r_x}{r_s}, \tag{5.33}$$

where $r_s = [M]/[A]$, the concentration ratio of impurity to calcium in solution. If growth occurred at near equilibrium supersaturation, the measured partition coefficient may be related to a thermodynamic equilibrium constant for the ion exchange reaction:

$$M + AB \rightarrow A + MB. \tag{5.34}$$

The equilibrium constant for this reaction may be expressed as the ratio of impurity to calcium carbonate activities divided by the ratio of impurity to calcium activities in solution,

$$K_{p,eq} = \frac{a_{MB}/a_{AB}}{(M)/(A)} = \frac{K_{AB}}{K_{MB}}, \tag{5.35}$$

which follows from $(\mathrm{A})_{eq}(\mathrm{B})_{eq} = \mathrm{K}_{AB}a_{AB}$ and $(\mathrm{M})_{eq}(\mathrm{B})_{eq} = \mathrm{K}_{MB}a_{MB}$. This expression may be related to the measured partition coefficient by solid and aqueous activity coefficients, such that

$$K_{p,eq} = K_p \frac{\gamma_{MB}/\gamma_{AB}}{\gamma_P/\gamma_A}, \tag{5.36}$$

where γ_i is the activity coefficient for solid or aqueous species i (Morse and Bender, 1990; Rimstidt et al., 1998).

5.3 Examples of model application

In the following section, the equations presented above will be used to model calcite growth from aqueous solutions containing three types of impurities: the non-incorporating impurity, polyaspartate, and two key trace constituents of calcite, strontium and magnesium. These impurities were selected because of the availability of high quality atomic force microscope (AFM) step velocity data. Divalent cations of strontium and magnesium also bracket Ca^{2+} in size, illustrating the effects of large and small cation substitution on calcite growth kinetics.

Kink inhibition by polyaspartate

Elhadj et al. (2006) performed a series of calcite precipitation experiments varying the concentrations of several polyaspartates with varying affinity to kink sites on the calcite surface. Polyaspartates are protein components found in biomineralizing organisms, which are thought to control crystal morphology through specific interactions with the calcite surface (Elhadj et al., 2006). With an exponential increase in polyaspartate concentration, the rate of calcite precipitation remains relatively constant (polyaspartate-1 and -2) or increases slightly (polyaspartate-4, -5 and -6) until a certain threshold concentration is reached. Above this threshold, step velocity plummets until steps are pinned. Figure 5.1 illustrates the observed dependence of obtuse step velocity on polyaspartate-1 and -2 concentrations with the corresponding model curve using parameters listed in Table 5.1.

Two significant effects of polyaspartate on calcite obtuse step velocity are not captured by the model in its most basic form: 1) increasing step velocity with increasing polyaspartate concentration and 2) complete step stoppage at sufficiently high [Asp]. The increased step velocity with increasing [Asp] cannot be modeled when the rate coefficients for calcium and carbonate attachment are assumed to be constant. However, disruption of the mineral surface solvation structure by adsorbed polyaspartate molecules could promote desolvation

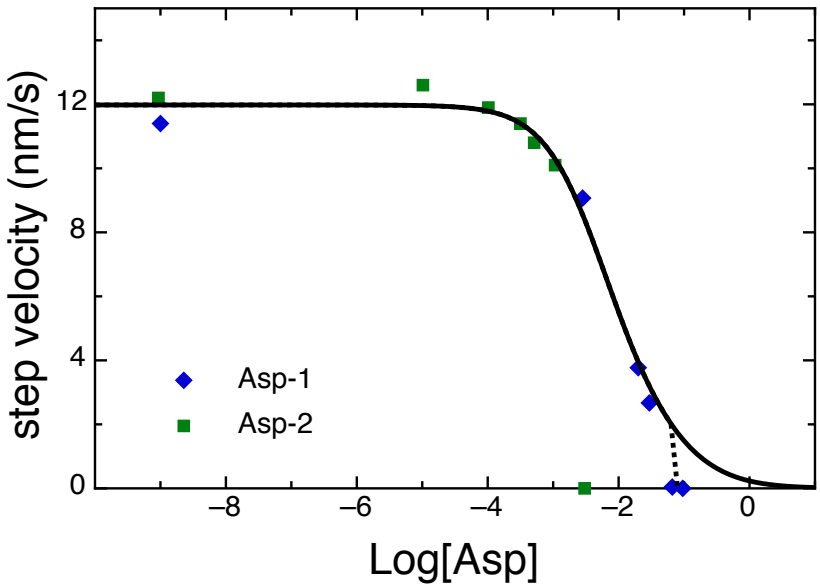

Figure 5.1: Calcite precipitation rate decreases exponentially as a function of the concentration of polyaspartate. The solid line represents a model fit to the experimental data from Elhadj et al. (2006) using parameters listed in Table 5.1. Step velocity was calculated based on Eq. 5.6 using kink propagation rates determined by substituting Eqs. 5.14-5.16 into Eq. 5.1. Dashed line assumes that 1D nucleation terminates when the kink spacing is less than 2 molecular units, the approximate step width occupied by Asp-1.

of ions at the surface, thereby accelerating ion attachment and growth (Elhadj et al., 2006; Piana et al., 2007; Chen et al., 2011).

It is possible to model complete step growth inhibition by assuming that the rate of 1D nucleation (I) goes to zero when the average distance between kinks is less than the width of the footprint of a given polyaspartate molecule along the step (Fig. 5.1, dotted line), at which point the entire step is effectively coated with the impurity. For slowly adsorbing impurities including certain peptides (Friddle et al., 2010; Weaver et al., 2010), terrace lifetime may not

Table 5.1: Optimized fit parameters to obtuse step velocities from Elhadj et al. (2006) experimental data, assuming $k_{Ca^{2+}} = k_{CO_3^{2-}} = k$ and $\nu_{Ca^{2+}} = \nu_{CO_3^{2-}} = \sqrt{K_{CaCO_3} k^2}$.

Asp	k $(s^{-1}M^{-1})$	k_{Asp}/ν_{Asp} (M^{-1})
1, 2	1.8e7	6.0e2

exceed the time to equilibrate the adsorbed impurity concentration. Disequilibrium impurity adsorption can lead to highly nonlinear step dynamics (Friddle et al., 2010; Weaver et al., 2010), which will not be captured by the model presented here. Polyaspartate adsorption to calcite appears to equilibrate sufficiently quickly to be modeled using the expressions presented here.

Strontium

Strontium occurs as a trace element at typically low abundance in near-surface terrestrial fluids. Its uptake in calcite is of interest to the scientific community as a potential reservoir for the radioactive contaminant ^{90}Sr (Lukashev, 1993), and the thermodynamics of the calcite-$SrCO_3$ solid solution is well-studied (e.g. Kulik et al., 2010, and references therein). The partitioning of strontium into calcite is rate dependent (Lorens, 1981; Tesoriero and Pankow, 1996; Gabitov and Watson, 2006), and the rate dependence has been attributed to aqueous (Rimstidt et al., 1998) and solid state diffusion (Gabitov and Watson, 2006) effects. Although strontium carbonate forms an aragonitic-type structure at low temperatures, and rhombohedral $SrCO_3$ does not exist in nature, Sr^{2+} substituted into calcite is 6-fold coordinated with oxygen (Pingitore et al., 1992). Thus, the thermodynamics of $Sr_xCa_{1-x}CO_3$ solid solutions relies upon determinations of the hypothetical rhombohedral $SrCO_3$ solubility (Böttcher, 1997; Kulik et al., 2010). The proposed equilibrium solubility of this phase ranges from $10^{-6.1}$ to $10^{-8.2}$, with most estimates being close to $10^{-7.6}$.

To calculate detachment frequencies of strontium and calcium ions during $Sr_xCa_{1-x}CO_3$ solid solution formation, the equilibrium ion activity products $(Sr^{2+})_{eq}(CO_3^{2-})_{eq}$ and $(Ca^{2+})_{eq}$ $(CO_3^{2-})_{eq}$ must be determined. For the strontium-calcite rhombohedral solid solution, these ion activity products may be equated to the product of endmember solubilities with endmember component activities in solution following Eqs. 5.29 and 5.30:

$$(Ca^{2+})_{eq}(CO_3^{2-})_{eq} = (1-x)\gamma_{CaCO_3}K_{CaCO_3}, \tag{5.37}$$

and

$$(Sr^{2+})_{eq}(CO_3^{2-})_{eq} = x\gamma_{SrCO_3}K_{SrCO_3}, \tag{5.38}$$

where γ_{CaCO_3}, γ_{SrCO_3}, K_{CaCO_3} and K_{SrCO_3} are the activity coefficients and solubilities of the calcite and rhombohedral $SrCO_3$ endmembers respectively (Plummer and Busenberg, 1987; Astilleros et al., 2003). The rhombohedral $SrCO_3$-calcite solid solution may be modeled as a regular solution, with mixing parameter (a_0) ranging from 1.1 to 3.2 (Kulik et al., 2010). The activity coefficient of each solid component in a regular solution between endmember components i and j may be approximated by the following expressions:

$$\gamma_i = exp(a_0 x_j^2), \tag{5.39}$$

and,

$$\gamma_j = exp(a_0 x_i^2), \tag{5.40}$$

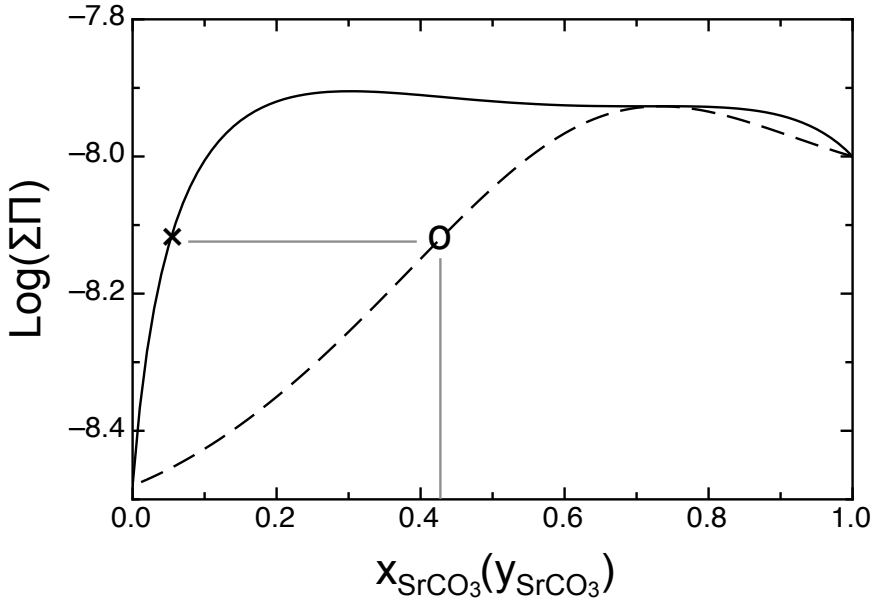

Figure 5.2: Lippmann diagram for the $Sr_xCa_{1-x}CO_3$ solid solution. The solid solution solidus is depicted as a solid line, and the solutus line is dashed. The solid mole fraction (x_{SrCO_3}) corresponding to point $\times$ has an equilibrium solution composition (y_{SrCO_3}) equal to the abscissa of point $\circ$.

where x_i and x_j are the mole fractions of components i and j in the solid solution.

A Lippmann diagram depicting the solidus (Eq. 5.25) and solutus (Eq. 5.27) of rhombohedral strontian calcite for a given mole fraction Sr (x) is shown in Figure 5.2. With small amounts of Sr incorporation, the total solubility of the $Sr_xCa_{1-x}CO_3$ solid solution increases substantially. The steeply rising solutus indicates that the increase in solubility is due in large part to enhanced solubility of the $CaCO_3$ endmember. The increasing detachment frequency of Ca^{2+} ions with increasing mole fraction $SrCO_3$ indicates that Sr uptake weakens Ca bonds with the calcite lattice (Figure 5.10). With sufficiently large amounts of Sr incorporation, the net rate of calcium and carbonate ion attachment will approach 0,

Table 5.2: Optimized fit parameters to obtuse step velocities from Wasylenki et al. (2005b) experimental data.

a0	$k_{Ca^{2+}} = k_{CO_3^{2-}}$ $s^{-1}M^{-1}$	$k_{Sr^{2+}}$ $s^{-1}M^{-1}$	$k_{CO_3^{2-}-Sr^{2+}}$ $s^{-1}M^{-1}$	$\nu_{CO_3^{2-}-Sr^{2+}}/\nu_{Sr^{2+}}$	R^2
2.37	1.22e7	3.7e6	1.65e8	0.621	0.78

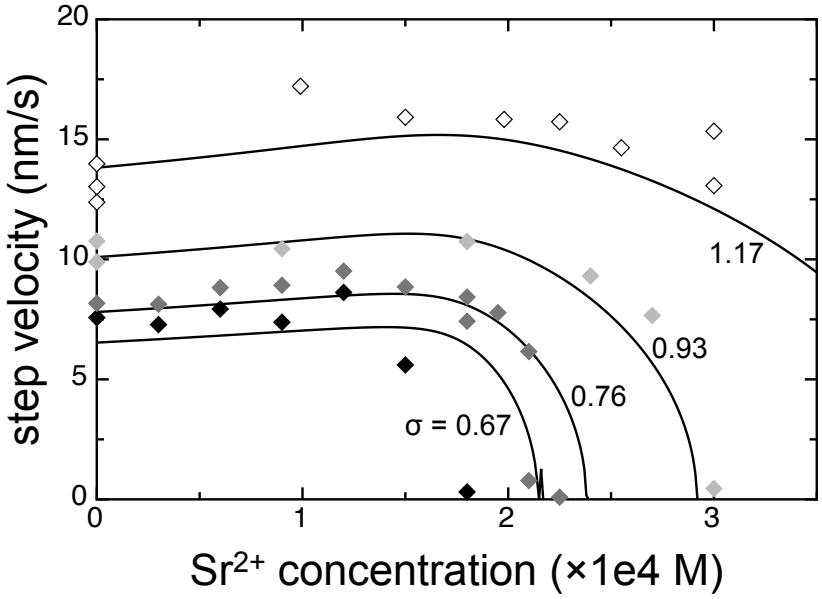

Figure 5.3: Obtuse step velocities optimized for a kinetic endmember fractionation factor of 0.3. The fit was optimized using the Levanburg-Marquardt algorithm, with a final R^2 value of 0.78.

causing an abrupt drop in mineral precipitation rate with increasing aqueous strontium.

We present the first model to successfully fit step velocity data observed by Wasylenki et al. (2005b). Step velocities (Figure 5.3) and partition coefficients (Figure 5.4) were fitted for $Sr_xCa_{1-x}CO_3$ precipitating from aqueous solutions of varied supersaturation and Sr/Ca ratios in solution. Strontium step velocities were calculated for a given solution composition from Eq. 5.6 using net kink propagation rates calculated by numerically solving for u_{Sr}, u_{Ca}, and u_{CO_3} (Eqs. 5.3-5.5 and 5.21-5.22). Details of the numerical methods can be found in Appendix D.2. Detachment rate coefficients were recalculated based on Eqs. 5.31 and 5.32 for each solution and corresponding steady state solid composition. Partition coefficients were calculated from the steady state solid composition for a given fluid composition based on Eq. 5.23 and 5.33.

Data fitting was optimized using the method of steepest descent. Fitted values for thermodynamic parameters a_0 and K_{SrCO_3} (rhombohedral) were limited to the range of values reported in Kulik et al. (2010). No constraints on kinetic parameters for strontium attachment to kink sites exist in the literature, so we allowed them to vary. The highest observed Sr distribution coefficient at 25 °C is approximately 0.3 (Gabitov and Watson, 2006), so we assigned this value to the kinetic endmember partition coefficient, $k_{Sr^{2+}}/k_{Ca^{2+}}$, the fast growth rate limit of the partition coefficient. It is possible that this threshold value could represent a transport limitation, where strontium diffuses more slowly than calcium to the

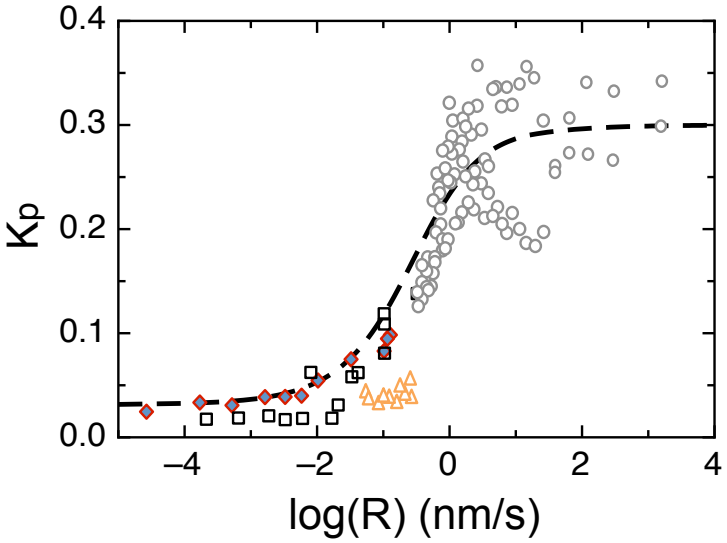

Figure 5.4: Partition coefficients optimized for a kinetic endmember partition coefficient of 0.3 modeled as a function of surface normal precipitation rate (nm/s). Literature data are compiled from (Gabitov and Watson, 2006, circles and triangles), (Lorens, 1981, diamonds), (Tesoriero and Pankow, 1996, squares)

mineral surface, instead of limitation by ion attachment rates to kinks. Because Sr^{2+} is weakly hydrated (relative to Ca^{2+}) in solution, it is expected that $k_{Sr^{2+}}$ might approach or even exceed $k_{Ca^{2+}}$, but this is not supported by observed Sr partitioning into rapidly precipitated calcite (Gabitov and Watson, 2006). Further experiments may be necessary to constrain the absolute kinetic endmember partition coefficient for strontium. Fitted solubility, attachment, and detachment rate coefficient parameters are listed in Table 5.2. Fits to step velocity data from Wasylenki et al. (2005b) and to strontium partitioning data compiled by Gabitov and Watson (2006) are displayed in Figures 5.3 and 5.4 respectively.

By reducing solid solution precipitation to its constituent reactions, we are able to identify the mechanisms controlling the nonlinear relationship between step velocity and aqueous strontium concentration. Carbonate ions attach readily to kink sites occupied by strontium ions, so strontium ions do not inhibit growth via a kink blocking mechanism. Strontium incorporation enhances the detachment kinetics of calcium and carbonate ions – likely by causing strain on the crystal lattice – inhibiting growth at relatively low Sr concentrations. Furthermore, strontium uptake decreases the detachment rate coefficient for Sr ions, suggesting that the lattice strain promotes the stability of the $SrCO_3$ solid solution endmember. These effects combined cause runaway Sr uptake and an abrupt decline in growth rate with increasing strontium activity in solution.

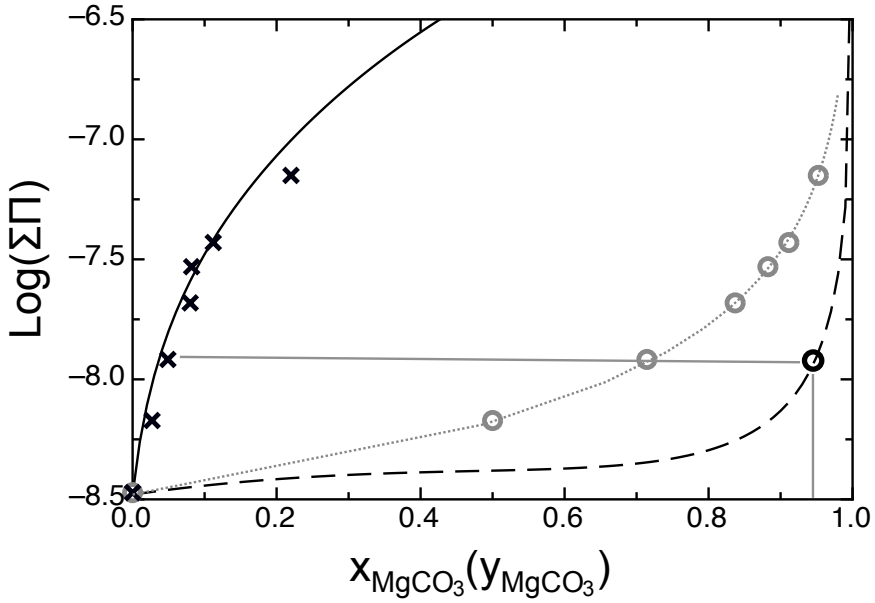

Figure 5.5: Lippmann diagram of magnesian calcite total solubility as a function of mole fraction of $MgCO_3$ in the solid solution (x_{MgCO_3}), which is represented by the solidus line (solid line), and mole fraction of aqueous magnesium in solution (y_{MgCO_3}), which is represented by the solutus line (dashed). The equilibrium solution with the composition denoted by the black ∘ is tied (gray horizontal line) to the corresponding equilibrium solid x_{MgCO_3}. Experimentally precipitated solid $Mg_xCa_{1-x}CO_3$ compositions and corresponding solution compositions from Mucci and Morse (1984) are represented by black × and gray ∘ symbols. The modeled total solubilities of solid and aqueous solution compositions marked as solid black and dotted gray lines respectively. Modeled total solubility for a given x_{MgCO_3} is the same as the equilibrium solidus line, while the modeled (and experimental) solution compositions do not correspond with the solutus line. Modeled solution compositions diverge from the solutus line, because precipitation does not occur at equilibrium.

Magnesium

Magnesian calcite is ubiquitous in terrestrial settings, and magnesium partitioning into calcite is a key paleotemperature proxy. Numerous experimental studies of magnesium partitioning into calcite have revealed that there is apparently no growth rate dependence over a wide range of supersaturations (Mucci and Morse, 1984; Mucci et al., 1985; Morse and Bender, 1990; Hartley and Mucci, 1996), from near equilibrium ($\sigma = 0.18$) to high supersaturation ($\sigma = 2.8$). It has been proposed that this occurs because Mg reaches exchange equilibrium with calcium at the surface (Mucci et al., 1985). This theory contrasts with the notion that the formation of high-magnesian calcite and dolomite are kinetically inhibited

(cf. Morse et al., 2007). Magnesium partitions into bulk calcite from seawater with $K_p \sim 0.016$. The lack of a growth rate effect indicates that the ratio of detachment rate coefficients ($\nu_{Mg^{2+}}/\nu_{Ca^{2+}}$) is constant with solid composition, because equilibrium partitioning is controlled by the ratio of forward to backward rates (DePaolo, 2011; Nielsen et al., 2012, chapter 2). Attachment rate coefficients are controlled primarily by ion desolvation kinetics, and the Mg^{2+} ion is widely thought to desolvate much more slowly than Ca^{2+} in aqueous solution, thus $k_{Mg^{2+}}/k_{Ca^{2+}}$ is probably significantly less than 1.

The thermodynamics of the Mg-calcite solid solution has been widely studied, and Lippmann diagrams effectively capture the relationship between equilibrium solid and aqueous compositions for magnesian calcite (Königsberger and Gamsjäger, 1992). Solid compositions obtained during precipitation experiments correspond exactly to the modeled solidus equation (Eq. 5.25) using the following activity coefficients:

$$\gamma_{CaCO_3} = e^{(-\epsilon'/2)x^2}, \tag{5.41}$$

and

$$\gamma_{MgCO_3} = e^{ln(\gamma_\infty)+\epsilon' x-(\epsilon'/2)x^2}. \tag{5.42}$$

Thermodynamic parameters for the Lippmann diagram of the Mg-calcite system used in Figure 5.5 are listed in Table 5.3. Experimentally determined solution compositions corresponding to a given total solubility do not correspond to the solutus curve (Figure 5.5).

We have modeled the dependence of magnesian calcite growth rate (Figures 5.6 and 5.7) and magnesium partitioning (Figure 5.8) on Mg concentration in solution following the procedure detailed in Appendix D.2 and fitted kinetic parameters listed in Table 5.4. Detachment rate coefficients were calculated by inserting γ_{CaCO_3} and γ_{MgCO_3} into Eqs. 5.31 and 5.32. Varying γ_∞ affects the calculated Mg partition coefficient at low supersaturations (Fig. 5.8). Using a value of γ_∞ of 1.2 yields a nearly constant ratio of Mg and Ca detachment

Table 5.3: Mg thermodynamic solid solution parameters. Endmember solubilities and ϵ' were taken from Königsberger and Gamsjäger (1992), while γ_∞ was fitted to observed solution compositions (black ∘ symbols in Fig. 5.5).

K_{CaCO_3}	K_{MgCO_3}	ϵ'	γ_∞
$10^{-8.48}$	$10^{-6.75}$	3.69	1.2

Table 5.4: Fit parameters to step velocities from Astilleros (2010) experimental data, total solubility compiled in Davis et al. (2000a,b), etc.

$k_{Ca^{2+}} = k_{CO_3^{2-}}$ $(s^{-1}M^{-1})$	$k_{Mg^{2+}}$ $(s^{-1}M^{-1})$	$k_{CO_3^{2-}-Mg^{2+}}$ $(s^{-1}M^{-1})$	$\nu_{CO_3^{2-}-Mg^{2+}}/\nu_{Mg^{2+}}$
3.0e6	5.1e4	1.53e3	1.0e3

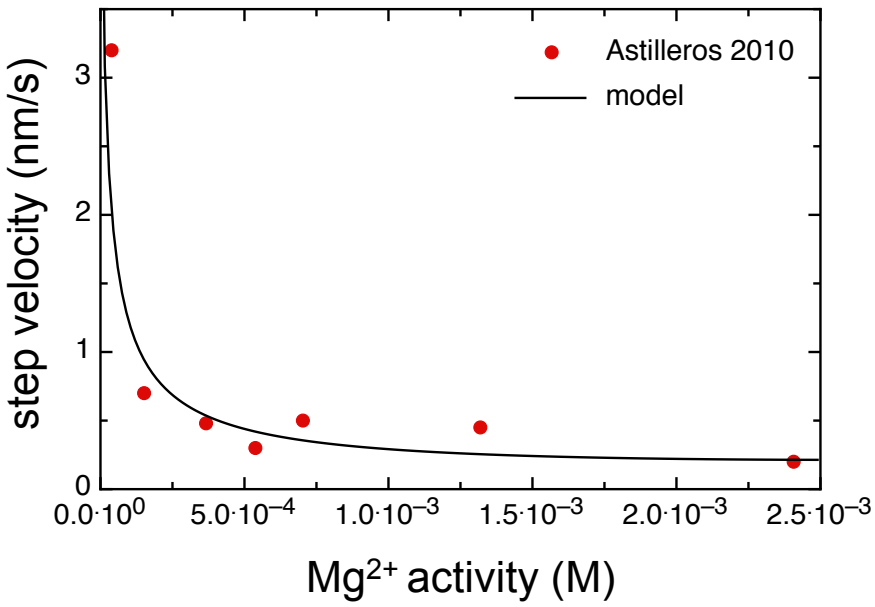

Figure 5.6: Modeled step velocity as a function of magnesium activity during calcite precipitation from oversaturated solution ($\sigma = 1.6$) with Ca^{2+}:$CO_3^{2-} = 1$ from Astilleros et al. (2010). Fitted kinetic coefficients are listed in Table 5.4 and thermodynamic data are listed in Table 5.3.

rate coefficients and consequently results in partition coefficients with little supersaturation dependence. In any case, Mg partition coefficients likely reflect kinetic endmember partitioning, where magnesium uptake is limited by desolvation kinetics. The observed T dependence of magnesium partitioning, then, may be due to changes in the relative rates of Ca^{2+} and Mg^{2+} ion desolvation. Higher temperature will promote magnesium desolvation and thus Mg uptake at kink sites.

Fitting the step velocity data of Astilleros et al. (2010) required that the rate coefficient of carbonate ion attachment to Mg be much smaller than the coefficient of Mg attachment (Table 5.4). The exponential drop in precipitation rate with increasing Mg activity suggests that magnesium inhibits calcite precipitation via a combined kink blocking and solubility mechanism. Magnesium attachment inhibits the subsequent attachment of carbonate, much like the blocking of a kink by a non-incorporating impurity. The total solubility and equilibrium ion activity product of magnesian carbonate increase significantly with Mg incorporation, but the solubility of the calcite endmember, $(Ca^{2+})_{eq}(CO_3^{2-})_{eq}$, does not change significantly with Mg uptake. Instead, the calcite endmember behaves as though an ideal solid solution is being formed, where γ_{CaCO_3} remains close to 1 up to relatively high magnesium contents.

This model is not consistent with the linear dependence of calcite step velocities on aque-

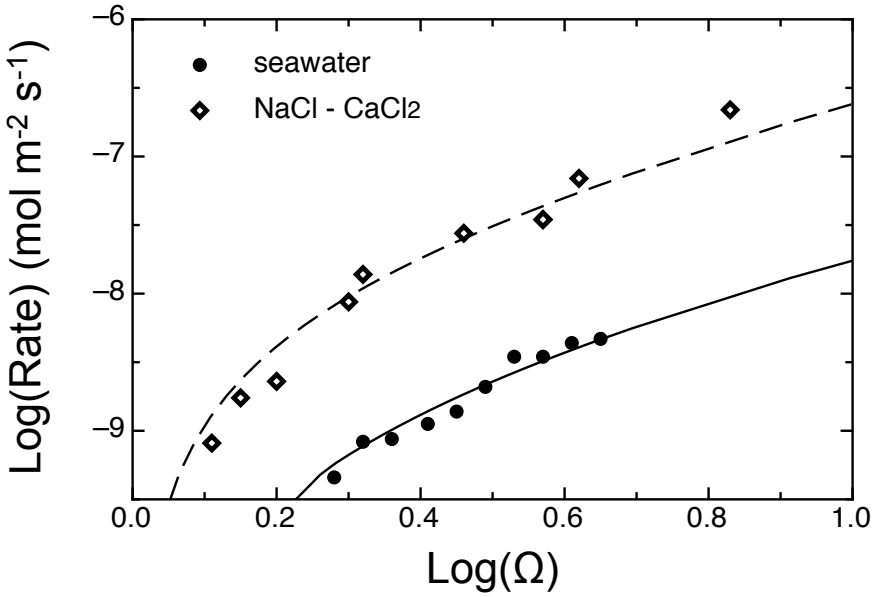

Figure 5.7: Calcite precipitation rates from NaCl - $CaCl_2$ solutions and seawater solutions as a function of calcite supersaturation reported by Lopez and Zuddas (2009). Rate data from NaCl - $CaCl_2$ solutions were fitted by setting $(Mg^{2+}) = 0$ (dashed line) , and data from seawater were fitted using the reported $Mg^{2+}/Ca^{2+} = 5.4$ (solid line). Both model fits use the same thermodynamic and kinetic coefficients listed in Tables 5.3 and 5.4, except the kinetic coefficients for ion attachment were all increased by a factor of 2.8 to fit the observed growth rates from seawater (solid line). Both models use a calcium activity $(Ca^{2+}) = 0.002$ equal to the approximate seawater value (Berner, 1965) with varied (CO_3^{2-}).

ous magnesium activity reported in Davis et al. (2000a,b). Astilleros et al. (2010) point out that steps growing upon the original (Mg-free) substrate propagate much more quickly than those precipitating on overgrowth, which are typically rough. It is possible that the Davis et al. (2000a) step velocities were recorded before a steady state growth rate was reached, where steps propagate over substrate of the same composition. This scenario is unlikely, because step propagation rates were relatively high. Davis et al. (2000a,b) use a 0.1M NaCl electrolyte solution in their experiments, while Astilleros et al. (2010) add no additional salts to their solutions. At low supersaturations, NaCl may inhibit precipitation. The complete stoppage of steps observed by Davis et al. (2000a,b) at low magnesium concentrations could possibly be due to kink pinning by the "background" electrolyte (Weaver et al., 2007).

If the assumption that detachment rate coefficients are controlled by thermodynamic equilibrium ion activity products is relaxed, it is possible to model the dependence of step velocity on Mg activity observed by Davis et al. (2000a,b). In this case, we assume that all detachment rate coefficients are equal, and calculate ν from the stoichiometric

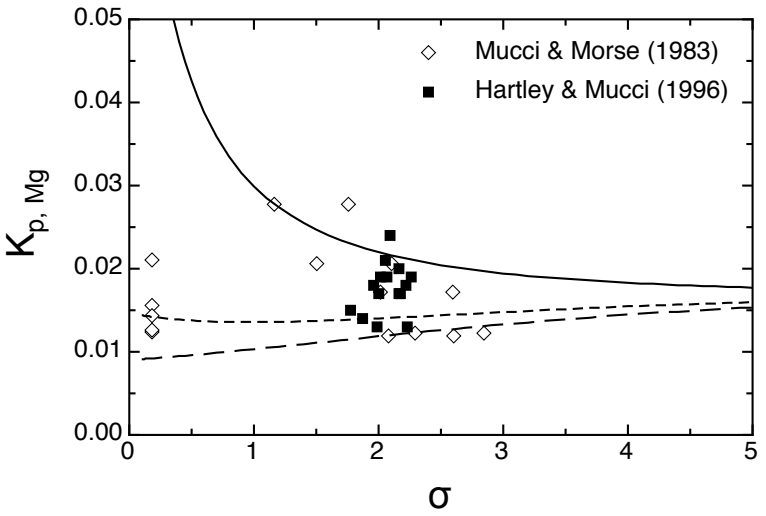

Figure 5.8: Modeled magnesium partition coefficient as a function of supersaturation with respect to calcite ($\sigma = \log(IAP/K_{sp})$). Typical measured magnesium partition coefficients during precipitation from seawater vary from 0.01 to 0.03, and estimated equilibrium partition coefficients range from ∼0.001 to 0.03 (Huang and Fairchild, 2001; Fantle and DePaolo, 2006). Fitted kinetic and thermodynamic parameters are the same as those listed in Tables 5.3 and 5.4, with the exception of γ_∞, which is varied from 0.1 (solid line) to 2 (lower dashed line). Magnesium partitioning modeled using parameters fitted to step velocity and total solubility data ($\gamma_\infty = 1.2$) is represented by the upper dashed line.

solubility of magnesian calcite ($K_{ss} = [(Mg^{2+})_{eq}(CO_3^{2-})_{eq}]^x[(Ca^{2+})_{eq}(CO_3^{2-})_{eq}]^{1-x}$), where $(Mg^{2+})_{eq}(CO_3^{2-})_{eq} = \frac{\nu^2 x}{k_{Mg^{2+}} k_{CO_3^{2-}-Mg^{2+}}}$, and $(Ca^{2+})_{eq}(CO_3^{2-})_{eq} = \frac{\nu^2(1-x)}{k_{Ca^{2+}} k_{CO_3^{2-}}}$ (from Eqs. 5.31 and 5.32). Alternative model fits to Davis et al. (2000b) data are shown in Fig. 5.9. If the same procedure is used to model Sr incorporation, however, it becomes impossible to model the observed dependence of strontian carbonate step velocity on Sr in solution.

Comparison of Sr and Mg inhibition effects

The inhibitory effects of strontium and magnesium on calcite growth significantly differ. Strontium uptake has little effect on calcite growth kinetics until a threshold strontium concentration is reached. Precipitation then abruptly halts as the solubility of the solid solution is reached. Magnesium uptake decreases the rate of calcite precipitation even at very low concentrations. With increasing magnesium concentration in solution, calcite step velocities have been shown to level off (Astilleros et al., 2010). The differences in inhibitory action may be attributed to the varying mechanisms of inhibition.

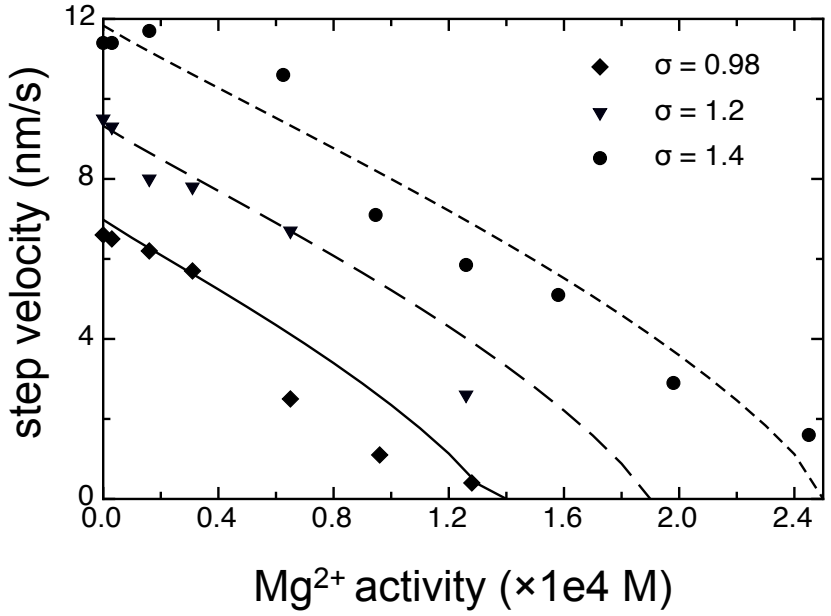

Figure 5.9: Fit to Davis (2000) obtuse step velocities using their reported IAP values. Detachment rate coefficients for Mg and Ca are assumed to be equal. Activities calculated from attachment and detachment rate coefficients violate the Gibbs-Duhem relation.

To compare the effects of Sr and Mg on calcite kink dynamics, we have plotted the Ca^{2+} detachment rate coefficient as a function of impurity mole fraction in the solid solution (Figure 5.10; from Eqs. 5.31 and 5.37). Increasing x_{SrCO_3} causes a significant increase in the solubility of the $CaCO_3$ end-member and therefore accelerates the kinetics of calcium detachment. Magnesium uptake, on the other hand, stabilizes Ca^{2+} kinks slightly. The observed exponential decrease in step velocity with increasing Mg, then, must be due to blocking of kinks by Mg ions.

5.4 Conclusion

Calcite precipitation from natural aqueous fluids usually results in the formation of solid solutions, where impurities substitute for Ca^{2+} or CO_3^{2-} in the mineral lattice. Even in the absence of impurity uptake, precipitation kinetics are typically slower in natural fluids than in simple growth solutions due to the blocking of active growth sites by adsorbed ions or molecules. Although impurity uptake and its inhibitory effects on mineral growth rate are widely observed, little is known about the mechanisms that retard growth. We demonstrated that the effects of both non-incorporated and incorporated impurities on calcite growth kinetics can be modeled using the same framework, where growth rate and composition are

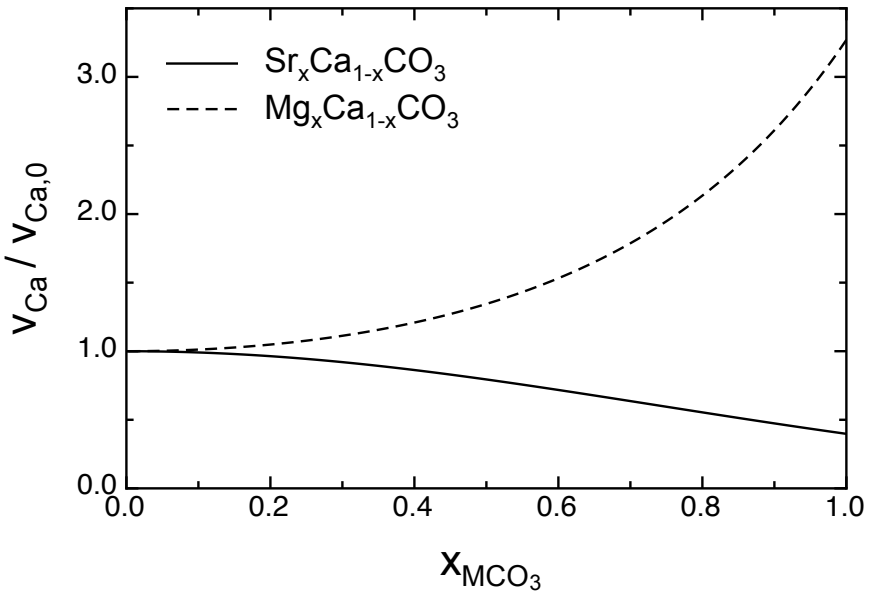

Figure 5.10: Detachment rate coefficients for calcium calculated as function of $SrCO_3$ and $MgCO_3$ mole fraction in the solid solution, normalized to the $\nu_{Ca^{2+}}$ of pure calcite.

controlled by net ion attachment to kink sites.

Incorporation of trace elements into the calcite lattice affects the mineral solubility and therefore bond energies and ion detachment kinetics. The equilibrium ion activity products of solid solution endmember components are controlled by the net fluxes of ions to and from kink sites. Using a regular solution model for strontian calcite, we were able to model the nonlinear relationship between aqueous strontium and step velocity observed by Wasylenki et al. (2005b). Using the same model, we are able to capture the exponential decrease in step velocity with increasing magnesium concentration observed by Astilleros et al. (2010). In the former case, strontium uptake causes the calcium activity coefficient to increase, which subsequently enhances the detachment rates of calcium ions. The growth rates of strontian calcite is solubility controlled. Magnesium uptake has little effect on the activity coefficient of calcium, so Mg^{2+} ions must effectively act as kink blockers. This interpretation is not consistent with the findings of Davis et al. (2000b), who observed a linear decrease in step velocity with increasing aqueous magnesium. It is unclear whether the results of Davis et al. (2000b) or Astilleros et al. (2010) are correct, but only the Astilleros et al. (2010) results are consistent with the model presented here.

The kinetic steady state model describing the effects of impurities on calcite growth kinetics and composition derived here is widely applicable to natural carbonates. The constraint equations (Eqs. 5.3-5.5) may be generalized to three or more component solid solutions if

the appropriate thermodynamic relations are known. To ensure the predictive power of this model, independent constraints on attachment and detachment rate coefficients – and the dependence of these parameters on solution compositional variables such as ionic strength – are required. Future *in situ* AFM growth experiments and corresponding molecular simulations may be used to extend our mechanistic understanding of controls on ion fluxes at kink sites. These efforts will move us towards a fully molecular description of the macroscopic growth rates and mineral compositions sampled in natural systems.

References

Astilleros J.M., Pina C.M., Fernández-Díaz L., and Putnis A. (2003) Metastable phenomena on calcite {1014} surface growing from Sr^{2+}–Ca^{2+}–CO_3^{2-} aqueous solutions. *Chem. Geol.* **193**, pp. 93–107.

Astilleros J.M., Fernández-Díaz L., and Putnis A. (2010) The role of magnesium in the growth of calcite: An AFM study. *Chem. Geol.* **271**, pp. 52–58.

Beck W.C., Grossman E.L., and Morse J.W. (2005) Experimental studies of oxygen isotope fractionation in the carbonic acid system at 15^o, 25^o and 40^oC. *Geochim. Cosmochim. Acta* **69**(14), pp. 3493–3503.

Berner R.A. (1965) Activity coefficients of bicarbonate, carbonate and calcium ions in sea water. *Geochim. Cosmochim. Acta* **29**, pp. 947–965.

Bertram M.A., Mackenzie F.T., Bishop F.C., and Bischoff W.D. (1991) Influence of temperature on the stability of magnesian calcite. *Am. Mineral.* **76**, pp. 1889–1896.

Bischoff J.L., Stine S., Rosenbauer R.J., Fitzpatrick J.A., and Stafford T.W. (1993) Ikaite precipitation by mixing of shoreline springs and lake water, Mono Lake, California, USA. *Geochim. Cosmochim. Acta* **57**(16), pp. 3855–3865.

Bischoff W.D., Mackenzie F.T., and Bishop F.C. (1987) Stabilities of synthetic magnesian calcites in aqueous solution: comparison with biogenic materials. *Geochim. Cosmochim. Acta* **51**, pp. 1413–1423.

Blum J.D., Erel Y., and Brown K. (1993) $^{87}Sr/^{86}Sr$ ratios of Sierra Nevada stream waters: Implications for relative mineral weathering rates. *Geochim. Cosmochim. Acta* **58**, pp. 5019–5025.

Böhm F., Gussone N., Eisenhauer A., Dullo W.C., Reynaud S., and Paytan A. (2006) Calcium isotope fractionation in modern scleractinian corals. *Geochim. Cosmochim. Acta* **70**(17), pp. 4452–4462.

Böttcher M.E. (1997) Comment on "Solid solution partitioning of Sr^{2+}, Ba^{2+}, and Cd^{2+} to calcite" by A. J. Tesoriero and J. F. Pankow. *Geochim. Cosmochim. Acta* **61**(3), pp. 661–662.

Bourg I.C., Richter F.M., Christensen J.N., and Sposito G. (2010) Isotopic mass-dependence of metal cation diffusion coefficients in liquid water. *Geochim. Cosmochim. Acta* **74**, pp. 2249–2256.

Burton E.A. and Walter L.M. (1987) Relative precipitation rates of aragonite and Mg calcite from seawater: Temperature or carbonate ion control? *Geology* **15**, pp. 111–114.

Burton E.A. and Walter L.M. (1990) The role of pH in phosphate inhibition of calcite and aragonite precipitation rates in seawater. *Geochim. Cosmochim. Acta* **54**, pp. 797–808.

Burton W.K., Cabrera N., and Frank F.C. (1951) The growth of crystals and the equilibrium structure of their surfaces. *Philos. Tr. R. Soc. A* **243**(866), pp. 299–358.

Butt H.J., Graf K., and Kappl M. (2006) *Physics and Chemistry of Interfaces*. Wiley-VCH, Weinheim.

Cabrera N. and Vermilyea D.A. (1958) Growth of crystals from solution. *Growth and Perfection of Crystals* (ed. R.H. Doremus), Wiley, New York, pp. 393–410.

Chang V.T., Williams R.J., Makishima A., Belshawl N.S., and O'Nions R.K. (2004a) Mg and Ca isotope fractionation during $CaCO_3$ biomineralisation. *Biochem. Biophys. Res. Commun.* **323**, pp. 79–85.

Chang V.T.C., Williams R.J.P., Makishima A., Belshawl N.S., and O'Nions R.K. (2004b) Mg and Ca isotope fractionation during $CaCO_3$ biomineralisation. *Biochem. Bioph. Res. Co.* **323**(1), pp. 79–85.

Chen C.L., Qi J., Zuckermann R.N., and Yoreo J.J.D. (2011) Engineered biomimetic polymers as tunable agents for controlling $CaCO_3$ mineralization. *J. Am. Chem. Soc.* **133**, pp. 5214–5217.

Chernov A.A., Yoreo J.J.D., Rashkovich L.N., and Vekilov P.G. (2004) Step and kink dynamics in inorganic protein crystallization. *MRS Bulletin* , pp. 927–934.

Chou L., Garrels R.M., and Wollast R.M. (1989) Comparative study of the kinetics and mechanisms of dissolution of carbonate minerals. *Chem. Geol.* **78**, pp. 269–282.

Clarkson J.R., Price T.J., and Adams C.J. (1992) Role of metastable phases in the spontaneous precipitation of calcium-carbonate. *J. Chem. Soc. Faraday T* **88**(2), pp. 243–249.

Cloud P. and LaJoie K.R. (1980) Calcite-impregnated defluidization structures in littoral sands of Mono Lake, California. *Science* **210**, pp. 1009–1012.

Davis K.J., Dove P.M., and Yoreo J.J.D. (2000a) Resolving the control of magnesium on calcite growth: Thermodynamic and kinetic consequences of impurity incorporation for biomineral formation. *Mat. Res. Soc. Symp.* **620**, pp. M9.5.1–M9.5.7.

Davis K.J., Dove P.M., and Yoreo J.J.D. (2000b) The role of Mg^{2+} as an impurity in calcite growth. *Science* **290**, pp. 1134–1137.

DePaolo D. (2011) Surface kinetic model for isotopic and trace element fractionation during precipitation of calcite from aqueous solutions. *Geochim. Cosmochim. Acta* **75**(4), pp. 1039–1056.

DePaolo D.J. (2004) Calcium isotopic variations produced by biological, kinetic, radiogenic and nucleosynthetic processes. *Rev. Mineral. Geochem.* **55**, pp. 255–288.

DeYoreo J.J., Land T.A., and Dair B. (1994) Growth-morphology of vicinal hillocks on the (101) face of KH2PO4 - from step-flow to layer-by-layer growth. *Phys. Rev. Lett.* **73**(6), pp. 838–841.

DeYoreo J.J., Zepeda-Ruiz L.A., Friddle R.W., Qiu S.R., Wasylenki L.E., Chernov A.A., Gilmer G.H., and Dove P.M. (2009) Rethinking classical crystal growth models through molecular scale insights: consequences of kink-limited kinetics. *Cryst. Growth Des.* **9**, pp. 5135–5144.

Dietzel M., Tang J., Leis A., and Koehler S.J. (2009) Oxygen isotopic fractionation during inorganic calcite precipitation - Effects of temperature, precipitation rate and pH. *Chem. Geol.* **268**(1-2), pp. 107–115.

Dove P.M. and Hochella M.F. (1993) Calcite precipitation mechanisms and inhibition by orthophosphate - In situ observations by scanning force microscopy. *Geochim. Cosmochim. Acta* **57**(3), pp. 705–714.

Dove P.M., Han N., Wallace A.F., and DeYoreo J.J. (2008) Kinetics of amorphous silica dissolution and the paradox of the silica polymorphs. *P. Natl. Acad. Sci.* **105**(29), pp. 9903–9908.

Dunn J.R. (1953) Origin of the deposits of tufa in Mono Lake. *J. Sediment. Petrol.* **23**(1), pp. 18–23.

Elhadj S., Salter E.A., Wierzbicki A., DeYoreo J.J., Han N., and Dove P.M. (2006) Peptide controls on calcite mineralization: Polyaspartate chain length affects growth kinetics and acts as a stereochemical switch on morphology. *Cryst. Growth Des.* **6**(1), pp. 197–201.

Erez J. (2003) The source of ions for biomineralization in foraminifera and their implications for paleoceanographic proxies. *Reviews in Mineralogy and Geochemistry: Biomineralization* (eds. P. Dove, J.D. Yoreo, and S. Weiner), Mineralogical Society of America, Washington, volume 54, chapter 5, pp. 115–149.

Fantle M.S. and DePaolo D.J. (2005) Variations in the marine Ca cycle over the past 20 million years. *Earth Planet. Sci. Lett.* **237**, pp. 102–117.

Fantle M.S. and DePaolo D.J. (2006) Sr isotopes and pore fluid chemistry in carbonate sediment of the Ontong Java Plateau: Calcite recrystallization rates and evidence for a rapid rise in seawater Mg over the last 10 million years. *Geochim. Cosmochim. Acta* **70**, pp. 3883–3904.

Fantle M.S. and DePaolo D.J. (2007) Ca isotopes in carbonate sediment and pore fluid from ODP Site 807A: The Ca2+(aq)-calcite equilibrium fractionation factor and calcite recrystallization rates in Pleistocene sediments. *Geochim. Cosmochim. Acta* **71**(10), pp. 2524–2546.

Farkaš J., Böhm F., Wallmann K., Blenkinsop J., Eisenhauer A., van Geldern R., Munnecke A., Voight S., and Veizer J. (2007) Calcium isotope record of Phanerozoic oceans: Implications for chemical evolution of seawater and its causative mechanisms. *Geochim. Cosmochim. Acta* **71**, pp. 5117–5134.

Flaathen T.K., Oelkers E.H., Gislason S.R., and Aagaard P. (2011) The effect of dissolved sulphate on calcite precipitation kinetics and consequences for subsurface CO_2 storage. *Energy Procedia* **4**, pp. 5037–5043.

Frank F.C. (1974) Nucleation-controlled growth on a one-dimensional growth of finite length. *J. Crystal Growth* **22**(3), pp. 233–236.

Friddle R.W., Weaver M.L., Qiu S.R., Wierzbicki A., Casey W.H., and Yoreo J.J.D. (2010) Subnanometer atomic force microscopy of peptide-mineral interactions links clustering and competition to acceleration and catastrophe. *Proc. Nat. Acad. Sci.* **107**, pp. 11–15.

Gabitov R.I. and Watson E.B. (2006) Partitioning of strontium between calcite and fluid. *Geochem. Geophys. Geosys.* **7**(11), pp. 1–12.

Gabitov R.I., Schmitt A.K., Watson E.B., McKeegan K.D., and Harrison T.M. (2011) Growth rate effect on oxygen isotopic fractionation between calcite and fluid: In situ data. *Goldschmidt Conf. Abstr.* , p. 878.

Gamsjäger H., Königsberger E., and Preis W. (2000) Lippmann diagrams: Theory and application to carbonate systems. *Aquatic Geochem.* **6**, pp. 119–132.

Garrels R.M. and Mackenzie F.T. (1967) Origin of chemical compositions of some springs and lakes. *Adv. Chem. Ser.* **67**, p. 222.

Glynn P.D. and Reardon E.J. (1990) Solid-solution aqueous-solution equilibria: Thermodynamic theory and representation. *Am. J. Sci.* **290**, pp. 164–201.

Gussone N., Eisenhauer A., Heuser A., Dietzel M., Bock B., Böhm F., Spero H.J., Lea D.W., Bijma J., and Nägler T.F. (2003a) Model for kinetic effects on calcium isotope fractionation (δ^{44}Ca) in inorganic aragonite and cultured planktonic foraminifera. *Geochim. Cosmochim. Acta* **67**(7), pp. 1375–1382.

Gussone N., Eisenhauer A., Heuser A., Dietzel M., Bock B., Böhm G., Spero H., Lea D.W., Buma J., and Nägler T. (2003b) Model for kinetic effects on calcium isotope fractionation (δ^{44}Ca) in inorganic aragonite and cultured planktonic foraminifera. *Geochim. Cosmochim. Acta* **67**(7), pp. 1375–1382.

Gussone N., Langer G., Geisen M., Eisenhauer A., and Riebesell U. (2004) Ca isotope fractionation in coccolithophores. *Geochim. Cosmochim. Acta* **68**(11), pp. A207–A207.

Gussone N., Böhm F., Eisenhauer A., Dietzel M., Heuser A., Teichert B.M.A., Reitner J., Worheide G., and Dullo W.C. (2005) Calcium isotope fractionation in calcite and aragonite. *Geochim. Cosmochim. Acta* **69**(18), pp. 4485–4494.

Harstad A.O. and Stipp S.L.S. (2007) Calcite dissolution: Effects of trace cations naturally present in Iceland spar calcites. *Geochim. Cosmochim. Acta* **71**, pp. 56–70.

Hartley G. and Mucci A. (1996) The influence of P_{CO_2} on the partitioning of magnesium in calcite overgrowths precipitated from artificial seawater at 25° and 1 atm total pressure. *Geochim. Cosmochim. Acta* **60**(2), pp. 315–324.

Hippler D., Eisenhauer A., and Nägler T.F. (2006) Tropical Atlantic SST history inferred from Ca isotope thermometry over the last 140ka. *Geochim. Cosmochim. Acta* **70**(1), pp. 90–100.

Hippler D., Kozdon R., Darling K.F., Eisenhauer A., and Nägler T.F. (2009) Calcium isotopic composition of high-latitude proxy carrier *Neogloboquadrina pachyderma* (sin.). *Biogeosciences* **6**(1), pp. 1–14.

Hofmann A.E., Bourg I.C., and DePaolo D.J. (2011) Ion desolvation as a mechanism for kinetic isotope fractionation. *Goldschmidt Conf. Abstr.* , p. 1035.

Huang Y.M. and Fairchild I.J. (2001) Partitioning of Sr^{2+} and Mg^{2+} into calcite under karst-analogue experimental conditions. *Geochim. Cosmochim. Acta* **65**, pp. 47–62.

Inskeep W.P. and Bloom P.R. (1985) An evaluation of rate equations for calcite precipitation kinetics at $p\mathrm{CO}_2$ les sthan 0.01 atm and pH greater than 8. *Geochim. Cosmochim. Acta* **49**, pp. 2165–2180.

Jellison R. and Roll S. (2003) Weakening and near breakdown of meromixis in Mono Lake .

Jellison R., Macintyre S., and Millero F. (1993) Density and conductivity properties of Na-CO_3-Cl-SO_4 brines from Mono Lake, California, USA. *Int. J. Salt Lake Res.* **8**, pp. 41–53.

Johnson C., Beard B., Roden E., Newman D.K., and Nealson K.H. (2004) Isotopic constraints on biogeochemical cycling of Fe. *Rev. Mineral. Geochem.* **55**(1), pp. 359–408.

Johnson K.S. (1982) Carbon dioxide hydration and dehydration kinetics in seawater. *Limnology Oceanography* **27**(5), pp. 849–855.

Jones and Stokes (1993) *California State Wat. Res. Control Board, Mono Basin Environmental Impact Report* .

Kasemann S., Schmidt D.N., Pearson P.N., and Hawkesworth C.J. (2008) Biological and ecological insights into Ca isotopes in planktic foraminifers as a paleotemperature proxy. *Earth Planet. Sci. Lett.* **271**, pp. 292–302.

Katz J.L., Reick M.R., Herzog R.E., and Parsiegla K.I. (1993) Calcite growth inhibition by iron. *Langmuir* **9**, pp. 1423–1430.

Kim S. and O'Neil J.R. (1997) Equilibrium and nonequilibrium oxygen isotope effects in synthetic carbonates. *Geochim. Cosmochim. Acta* **61**(16), pp. 3461–3475.

Komiya T., Suga A., Ohno T., Han J., Guo J., Yamamoto S., Hirata T., and Li Y. (2008) Ca isotopic compositions of dolomite, phosphorite and the oldest animal embryo fossils from the Neoproterozoic in Weng'an, South China. *Gondwana Res.* **14**(1-2), pp. 209–218.

Königsberger E. and Gamsjäger H. (1992) Solid-solute phase equilibria in aqueous solution: VII. A re-interpretation of magnesian calcite stabilities. *Geochim. Cosmochim. Acta* **56**, pp. 4095–4098.

Kulik D.A., Vinograd V.L., Paulsen N., and Winkler B. (2010) (Ca,Sr)CO_3 aqueous-solid solution systems: From atomistic simulations to thermodynamic modeling. *Phys. Chem. Earth* **35**, pp. 217–232.

LADWP (2010) *Aqueduct Northern District Daily Report*, p. Also available at at http://www.ladwp.com/ladwp/cms/ladwp005341.jsp.

Larsen K., Bechgaard K., and Stipp S.L.S. (2010) Modelling spiral growth at dislocations and determination of critical step lengths from pyramid geometries on calcite surfaces. *Geochim. Cosmochim. Acta* **74**(2), pp. 558–567.

Lea D.W., Bijma J., Spero H.J., and Archer D. (1999) Implications of a carbonate ion effect on shell carbon and oxygen isotopes for glacial ocean conditions. *Use of Proxies in Paleoceanography: Examples from the South Atlantic* (eds. G. Fischer and G. Wefer), Springer-Verlag, Heidelberg, pp. 513–522.

Lemarchand D., Wasserburg G., and Papanastassiou D.A. (2004) Rate-controlled calcium isotope fractionation in synthetic calcite. *Geochim. Cosmochim. Acta* **68**(22), pp. 4665–4678.

Li H.C. (1995) *Isotope geochemistry of Mono Basin, California: applications to paleoclimate and paleohydrology*. Ph.D. thesis, University of Southern California.

Li H.C. and Ku T.L. (1997) δ^{13}C- δ^{18}O covariance as a paleohydrological indicator for closed-basin lakes. *Paleoocean. Paleoclimat. Paleoeco.* **133**, pp. 69–80.

Lin Y. and Singer P.C. (2006) Inhibition of calcite precipitation by orthophosphate: Speciation and thermodynamic considerations. *Geochim. Cosmochim. Acta* **70**, pp. 2530–2539.

Lopez O., Zuddas P., and Faivre D. (2009) The influence of temperature and seawater composition on calcite crystal growth mechanisms and kinetics: Implications for Mg incorporation in calcite lattice. *Geochim. Cosmochim. Acta* **73**, pp. 337–347.

Lorens R.B. (1981) Sr, Cd, Md and Co distribution coefficients in calcite as a function of calcite precipitation rate. *Geochim. Cosmochim. Acta* **45**, pp. 553–561.

Lukashev V.K. (1993) Some geochemical and environmental aspects of the Chernobyl nuclear accident. *Appl. Geochem.* **8**, pp. 419–436.

Malkin A.I., Chernov A.A., and Alexeev I.V. (1989) Growth of dipyramidal face of dislocation-free ADP crystals - Free-energy of steps. *J. Crystal Growth* **97**(3-4), pp. 765–769.

Meibom A., Cuif J.P., Houlbreque F., Mostefaoui S., Dauphin Y., Meibom K.L., and Dunbar R. (2008) Compositional variations at ultra-structure length scales in coral skeleton. *Geochim. Cosmochim. Acta* **72**, pp. 1555–1569.

Meyer H.J. (1984) The influence of impurities on the growth rate of calcite. *J. Cryst. Growth* **66**, pp. 639–646.

Morse J.W. and Arvidson R.S. (2002) The dissolution kinetics of major sedimentary carbonate minerals. *Earth-Sci. Rev.* **58**(1-2), pp. 51–84.

Morse J.W. and Bender M.L. (1990) Partition coefficients in calcite: Examinations of factors influencing the validity of experimental results and their application to natural systems. *Chem. Geol.* **82**, pp. 265–277.

Morse J.W., Arvidson R.S., and Lüttge A. (2007) Calcium carbonate formation and dissolution. *Chem. Rev.* **107**, pp. 342–381.

Mucci A. (1986) Growth kinetics and composition of magnesian calcite overgrowths precipitated from seawater: Quantitative influence of orthophosphate ions. *Geochim. Cosmochim. Acta* **50**, pp. 2255–2265.

Mucci A. and Morse J.W. (1984) The solubility of calcite in seawater solutions of various magnesium concentration, $I_t = 0.697$ m at 25°C and one atmosphere total pressure. *Geochim. Cosmochim. Acta* **48**, pp. 815–822.

Mucci A., Morse J.W., and Kaminsky M.S. (1985) Auger spectroscopy analysis of magnesian calcite overgrowths precipitated from seawater and solutions of similar composition. *Am. J. Sci.* **285**, pp. 289–305.

Nägler T. (2000) The δ^{44}Ca-temperature calibration on fossil and cultured *Globigerinoides sacculifer*: New tool for reconstruction of past sea surface temperatures. *Geochem. Geophys. Geosys.* **1**.

Nancollas G.H. and Reddy M.M. (1971) The crystallization of calcium carbonate II. Calcite growth mechanism. *J. Colloid Interface Sci* **37**(4), pp. 824–830.

Nehrke G., Reichart G., Cappellen P.V., Meile C., and Bijma J. (2007) Dependence of calcite growth rate and Sr partitioning on solution stoichiometry: Non-Kossel crystal growth. *Geochim. Cosmochim. Acta* **71**, pp. 2240–2249.

Neumann K. and Dreiss S. (1995) Strontium 87/strontium 86 ratios as tracers in groundwater and surface waters in Mono Basin, California. *Water Resour. Res.* **31**(12), pp. 3183–3193.

Newton M. (1994) Holocene fluctuations of Mono Lake, California: the sedimentary record. *Sedimentology and Geochemistry of Modern and Ancient Saline Lakes* (eds. R.W. Renaut and W.M. Last), Society for Sedimentary Geology, Tulsa, pp. 143–158.

Nielsen L.C. and DePaolo D.J. (in review) Ca isotope fractionation in a high-alkalinity lake system: Mono Lake, California. *Geochim. Cosmochim. Acta* .

Nielsen L.C., Druhan J.L., Yang W., Brown S.T., and DePaolo D.J. (2011) Calcium isotopes as tracers of biogeochemical processes. *Handbook of Environmental Isotope Geochemistry* (ed. M. Baskaran), Springer, New York, volume 1, chapter 7, pp. 105–124.

Nielsen L.C., DePaolo D.J., and Yoreo J.J.D. (2012) Self-consistent ion-by-ion growth model for kinetic isotope fractionation during calcite precipitation. *Geochim. Cosmochim. Acta* .

Nielsen L.C., Yoreo J.J.D., and DePaolo D.J. (in prep) Theory of co-dependent calcite growth kinetics, inhibition and impurity uptake .

Nilsson O. and Sternbeck J. (1999) A mechanistic model for calcite crystal growth using surface speciation. *Geochim. Cosmochim. Acta* **63**, pp. 217–225.

Paquette J. and Reeder R.J. (1995) Relationship between surface structure, growth mechanism, and trace element incorporation in calcite. *Geochim. Cosmochim. Acta* **59**(4), pp. 735–749.

Parkhurst D.L. and Appelo C.A.J. (1999) User's guide to PHREEQc (version 2) - A computer program for speciation, batch-reaction, one-dimensional transport, and inverse geochemical calculations. *U.S. Geological Survey Water-Resources Investigations Report* **99**(4259).

Parsiegla K.I. and Katz J.L. (1999) Calcite growth inhibition by copper(II) I. Effect of supersaturation. *J. Cryst. Growth* **200**, pp. 213–226.

Piana S., Jones F., and Gale J.D. (2007) Aspartic acid as a crystal growth catalyst. *Cryst. Eng. Comm.* **9**, pp. 1187–1191.

Pingitore N.E., Lytle F.W., Davies B.M., Eastman M.P., Eller P.G., and Larson E.M. (1992) Mode of incorporation of Sr^{2+} in calcite: Determination by X-ray absorption spectroscopy. *Geochim. Cosmochim. Acta* **56**, pp. 1531–1538.

Plummer L.N. and Busenberg E. (1987) Thermodynamics of aragonite-strontianite solid solutions: Results from stoichiometric solubility. *Geochim. Cosmochim. Acta* **51**, pp. 1393–1411.

Plummer L.N., Parkhurst D.L., and Wigley T.M.L. (1979) Critical review of the kinetics of calcite dissolution and precipitation. *Chemical Modeling in Aqueous Systems* (ed. E. Jenne), ACS Symp. Ser., pp. 537–573.

Reddy M.M. and Hoch A.R. (2000) Calcite crystal growth rate inhibition by aquatic humic substantces. *Advances in Crystal Growth Inhibition Technologies* (ed. Amjad), Kluwer Academic/Plenum Publishers, New York, pp. 107–121.

Reynard L.M., Henderson G.M., and Hedges R.E.M. (2010) Calcium isotope ratios in animal and human bone. *Geochim. Cosmochim. Acta* **74**(13), pp. 3735–3750.

Reynard L.M., Day C.C., and Henderson G.M. (2011) Large fractionation of calcium isotopes during cave-analogue calcium carbonate growth. *Geochim. Cosmochim. Acta* **75**, pp. 3726–3740.

Rimstidt J.D., Balog A., and Webb J. (1998) Distribution of trace elements between carbonate minerals and aqueous solutions. *Geochim. Cosmochim. Acta* **62**(11), pp. 1851–1863.

Rocha C.D.L. and DePaolo D.J. (2000) Evidence for variations in marine calcium cycle over the Cenozoic. *Science* **289**, pp. 1176–1178.

Rollion-Bard C., Vigier N., and Spezzaferri S. (2007) In situ measurements of calcium isotopes by ion microprobe in carbonates and application to foraminifera. *Chem. Geol.* **244**, pp. 679–690.

Romanek C.S., Grossman E.L., and Morse J.W. (1992) Carbon isotopic fractionation in synthetic aragonite and calcite: Effects of temperature and precipitation rate. *Geochim. Cosmochim. Acta* **235**, pp. 365–370.

Russell A.D., Hönisch B., Spero H.J., and Lea D.W. (2004) Effects of seawater carbonate ion concentration and temperature on shell U, Mg, and Sr in cultured planktonic foraminifera. *Geochim. Cosmochim. Acta* **68**(21), pp. 4347–4361.

Russell I.C. (1889) Quaternary History of Mono Valley, California. *Eighth Annual Report of the USGS*, pp. 267–394.

Russell W., Papanastassiou D., and Tombrello T. (1978) Ca isotope fractionation on earth and other solar-system materials. *Geochim. Cosmochim. Acta* **42**(8), pp. 1075–1090.

Scholl D. and Taft W. (1964) Algae, contributors to the formation of calcareous tufa, Mono Lake, California. *J. Sediment. Res.* **34**(2), pp. 309–319.

Simon J.I. and DePaolo D.J. (2010) Stable calcium isotopic composition of meteorites and rocky planets. *Earth Planet. Sci. Lett.* **289**(3-4), pp. 457–466.

Skulan J. and DePaolo D.J. (1999) Calcium isotope fractionation between soft and mineralized tissues as a monitor of calcium use in vertebrates. *Proc. Natl. Acad. Sci.* .

Skulan J., DePaolo D.J., and Owens T.L. (1997) Biological control of calcium isotopic abundances in the global calcium cycle. *Geochim. Cosmochim. Acta* **61**(12), pp. 2505–2510.

Spero H.J., Bijma J., Lea D.W., and Bemis B.E. (1997) Effect of seawater carbonate concentration on foraminiferal carbon and oxygen isotopes. *Nature* **390**, pp. 497–500.

Steefel C.I. (2009) CrunchFlow: Software for modeling multicomponent reactive flow and transport. *Users Manual* .

Steefel C.I. and Maher K. (2009) Fluid-Rock Interaction: A Reactive Transport Approach. *Rev. Mineral. Geochem.* **70**, pp. 485–532.

Suzuki A., Nakamori T., and Kayanne H. (1995) The mechanism of production enhancement in coral reef carbonate systems: model and empirical results. *Sed. Geol.* **99**(3–4), pp. 259–280.

Suzuku A. and Kawahata H. (2004) Reef water CO_2 system and carbon production of coral reefs: Topographic control of system-level performance. *Global Environmental Change in the Ocean and on Land* (ed. M. Shiyomi), Terrapub, pp. 229–248.

Tang J., Dietzel M., Böhm F., Kohler S., and Eisenhauer A. (2008a) Sr^{2+}/Ca^{2+} and $^{44}Ca/^{40}Ca$ fractionation during inorganic calcite formation: II. Ca isotopes. *Geochim. Cosmochim. Acta* **72**, pp. 3733–3745.

Tang J., Köhler S., and Dietzel M. (2008b) Sr^{2+}/Ca^{2+} and $^{44}Ca/^{40}Ca$ fractionation during inorganic calcite formation: I. Sr incorporation. *Geochim. Cosmochim. Acta* **72**, pp. 3718–3732.

Teng H.H., Dove P.M., Orme C.A., and DeYoreo J.J. (1998) Thermodynamics of calcite growth: Baseline for understanding biomineral formation. *Science* **282**(5389), pp. 724–727.

Teng H.H., Dove P.M., and DeYoreo J.J. (1999) Reversed calcite morphologies induced by microscopic growth kinetics: Insight into biomineralization. *Geochim. Cosmochim. Acta* **63**(17), pp. 2507–2512.

Teng H.H., Dove P.M., and DeYoreo J.J. (2000) Kinetics of calcite growth: Surface processes and relationships to macroscopic rate laws. *Geochim. Cosmochim. Acta* **13**, pp. 2255–2266.

Tesoriero A.J. and Pankow J.F. (1996) Solid solution partitioning of Sr^{2+}, Ba^{2+}, and Cd^{2+} to calcite. *Geochim. Cosmochim. Acta* **60**(6), pp. 1053–1063.

Tomascak P.B., Hemming G.N., and Hemming S.R. (2003) The lithium isotopic composition of waters of the Mono Basin, California. *Geochim. Cosmochim. Acta* **67**(4), pp. 601–611.

van der Eerden J. (1993) Crystal growth mechanisms. *Handbook of crystal growth* (ed. D.J.T. Hurle), NorthHolland, Amsterdam, volume 1a, pp. 445–447.

Wasylenki L.E., Dove P.M., and DeYoreo J.J. (2005a) Effects of temperature and transport conditions on calcite growth in the presence of Mg^{2+}: Implications for paleothermometry. *Geochim. Cosmochim. Acta* **69**(17), pp. 4227–4236.

Wasylenki L.E., Dove P.M., Wilson D.S., and DeYoreo J.J. (2005b) Nanoscale effects of strontium on calcite growth: An in situ AFM study in the absence of vital effects. *Geochim. Cosmochim. Acta* **69**(12), pp. 3017–3027.

Watson E.B. (1996) Surface enrichment and trace-element uptake during crystal growth. *Geochim. Cosmochim. Acta* **60**(24), pp. 5013–5020.

Weaver M.L., Qiu S.R., Hoyer J.R., Casey W.H., Nancollas G.H., and Yoreo J.J.D. (2007) Inhibition of calcium oxalate monohydrate growth by citrate and the effect of the background electrolyte. *J. Cryst. Growth* **306**, pp. 135–145.

Weaver M.L., Qiu S.R., Friddle R.W., Casey W.H., and Yoreo J.J.D. (2010) How the overlapping time scales for peptide binding and terrace exposure lead to nonlinear step dynamics during growth of calcium oxalate monohydrate. *Cryst. Growth Des.* **10**, pp. 2954–2959.

Wiechers H.N.S., Sturrock P., and v R Marais G. (1975) Calcium carbonate crystallization kinetics. *Water Res.* **9**, pp. 835–845.

Wolthers M., Nehrke G., Gustafsson J.P., and Cappellen P.V. (2012) Calcite growth kinetics: Modeling the effect of solution stoichiometry. *Geochim. Cosmochim. Acta* **77**, pp. 121–134.

Young E.D., Galy A., and Nagahara H. (2002) Kinetic and equilibrium mass-dependent isotope fractionation laws in nature and their geochemical and cosmochemical significance. *Geochim. Cosmochim. Acta* **66**(6), pp. 1095–1104.

Zachos J., Pagani M., Sloan L., Thomas E., and Billups K. (2001) Trends, rhythms, and aberrations in global climate 65 Ma to present. *Science* **292**, pp. 686–693.

Zhang J. and Nancollas G.H. (1990) Kink densities along a crystal surface step at low temperatures and under nonequilibrium conditions. *J. Crystal Growth* **106**, pp. 181–190.

Zhang J.W. and Nancollas G.H. (1998) Kink density and rate of step movement during growth and dissolution of an AB crystal in a nonstoichiometric solution. *J. Colloid Interf. Sci.* **200**(1), pp. 131–145.

Zhang Y.P. and Dawe R. (1998) The kinetics of calcite precipitation from a high salinity water. *Appl. Geochem.* **13**(2), pp. 177–184.

Zhong S. and Mucci A. (1993) Calcite precipitation in seawater using a constant addition technique: A new overall reaction kinetic expression. *Geochim. Cosmochim. Acta* **57**, pp. 1409–1417.

Zuddas P. and Mucci A. (1994) Kinetics of calcite precipitation from seawater: I. A classical chemical kinetics description for strong electrolyte solutions. *Geochim. Cosmochim. Acta* **58**(20), pp. 4353–4362.

Appendix A

Derivation of kink density

To maintain a steady state kink density, kink sites must be annihilated and created at the same rate during mineral precipitation (Frank, 1974; Zhang and Nancollas, 1998). Along a given step length L (m), with average kink spacing x_0 (m), kink propagation rate u (s^{-1}), and molecular unit width a (m), all kinks along L are annihilated by collision in the time (t) required for a given kink to move by x_0. Thus

$$x_0 = uat. \tag{A.1}$$

The total number of kinks is L/x_0, so the frequency of annihilation due to collision (R_{coll}) is

$$R_{coll} = \frac{Lua}{x_0^2}. \tag{A.2}$$

Kinks are simultaneously being created along the step via 1D nucleation, with frequency per molecule i. The rate of kink formation (R_{fm}) is then

$$R_{fm} = 2i\frac{L}{a}, \tag{A.3}$$

where two kinks are created by each nucleation event and L/a is the number of molecules along the step.

At steady state, $R_{coll} = R_{fm}$, so kink density ($\rho = a/x_0$) may be expressed:

$$\rho = \sqrt{\frac{2i}{u}} = 2\sqrt{\frac{i}{2u}}. \tag{A.4}$$

Appendix B

Step velocity anisotropy

The vicinal faces of calcite display two distinct step edge structures, acute and obtuse. Acute steps form an acute angle with the terrace below, while obtuse steps form obtuse angles. Changing solution stoichiometry and oversaturation shifts the relative growth velocities of acute and obtuse steps, causing the angle (θ) between the faces to change (Fig. B.1)(Teng et al., 1999; Larsen et al., 2010). Due to geometric constraints of the calcite $\{10\bar{1}4\}$ face, angle γ between acute-acute and obtuse-obtuse faces is 101.6°. If obtuse step velocity, v_+, is greater than acute step velocity, v_-, θ can be shown to equal:

$$\theta = 2atan\left[tan\left(\frac{\gamma}{2}\right)\frac{v_+ + v_-}{v_+ - v_-}\right]. \tag{B.1}$$

If acute step velocities exceed those of obtuse steps, (v_--v_+) replaces (v_+-v_-) in the denominator of Eq. B.1. In time interval t, obtuse and acute steps travel by $v_+t=ny_{0,+}$ and $v_-t=ny_{0,-}$ respectively, where $y_{0,\pm}$ is the step spacing and n is the number of step widths traveled in time t. It is trivial to show that $\frac{v_+}{v_-} = \frac{y_{0,+}}{y_{0,-}}$. The fraction of new growth with obtuse geometry becomes: $f_+=\frac{v_+}{v_+ + v_-}$. By fitting the rate constants k and ν and endmember fractionation factors separately for acute and obtuse faces, independent expressions for step velocity and α_p may be obtained for each step type (Eq. 2.13). The total fractionation factor becomes:

$$\alpha_{p,tot} = f_+\alpha_{p,+} + (1 - f_+)\alpha_{p,-}, \tag{B.2}$$

where $\alpha_{p,\pm}$ is the fractionation factor associated with step type $\pm$.

Unlike trace element or isotopic composition, growth rate is independent of step proportions expressed on the surface, because

$$R_{net} = \frac{vbd}{y_0} = \frac{v_+bd}{y_{0,+}} = \frac{v_-bd}{y_{0,-}}, \tag{B.3}$$

so the solution composition dependence of only a single set of step velocities and terrace widths, acute or obtuse, must be determined experimentally to predict growth rate.

Isotopic fractionation is not expected to vary significantly with step growth anisotropy, because isotope partitioning will not be affected by kink site geometry: isotopes of different mass are similar in size. However, trace elements tend to partition strongly into the acute or obtuse face depending on ionic size, so the total distribution will be sensitive to the growth hillock shape.

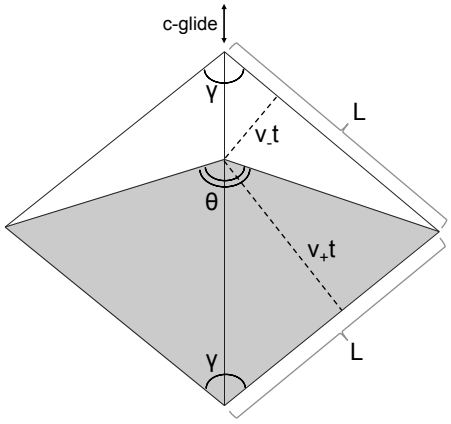

Figure B.1: Schematic plan view of a growth hillock under conditions where obtuse (+) faces (shaded) are growing more quickly than acute (-) faces. The angle between similar faces (γ) is 101.6° on the $\{10\bar{1}4\}$ face of calcite. The c-glide plane bisects γ. The step edge length, L, is equal along all faces.

Appendix C

SIMS data from calcite overgrowth experiments

Table C.1: Measured calcium isotopic composition of standard calcite (MEX) and overgrowth material from flow cell precipitation experiments. Individual analyses are reported with 2 standard error (s.e.) internal errors, and averages are reported with 2 s.e. external error. Overgrowth samples with $\Delta^{44/40}\text{Ca}_{s-f}$ values calculated relative to corrected $\delta^{44/40}\text{Ca}_{MEX}$ are denoted by Y. Corrections are made based on linear fits to MEX calcium isotopic composition as a function of X or Y position. All other $\Delta^{44/40}\text{Ca}_{s-f}$ values are calculated directly from the average $\delta^{44/40}\text{Ca}_{MEX}$. MEX calcite is 0.57(21) ‰ heavier than stock fluid calcium analyzed via TIMS.

Sample	$\delta^{44/40}$**Ca** (‰)	**2 s.e.** (‰)	**X** (μ**m**)	**Y** (μ**m**)	$\Delta^{44/40}\text{Ca}_{s-f}$ (‰)	**Corrected?**
Exp. 7 MEX						
Exp7_MEX@1	-46.04	0.07	-1430	2259		
Exp7_MEX@2	-46.16	0.09	-1430	2059		
Exp7_MEX@3	-45.79	0.11	-1530	-4766		
Exp7_MEX@4	-45.76	0.06	-1430	-4866		
Exp7_MEX@5	-45.50	0.08	-780	2274		
Exp. 7 Overgrowth						
Exp7_growth_drp@4	-46.25	0.08	-1730	-2666	0.20	Y
Exp7_growth_drp@5	-46.33	0.11	-1730	-2766	0.11	Y
Exp7_growth_drp@6	-46.14	0.07	-1530	-2741	0.30	Y
Exp7_growth_drp@7	-46.62	0.09	-1530	-2926	-0.18	Y
Exp7_growth_drp@8	-46.13	0.08	-1380	-2926	0.31	Y
average					*0.15*	
2 s.e.					*0.18*	
minimum					*-0.18*	

Continued on Next Page...

Sample	$\delta^{44/40}$Ca (‰)	2 s.e. (‰)	X (μm)	Y (μm)	$\Delta^{44/40}Ca_{s-f}$ (‰)	Corrected?
Exp. 8 MEX						
Exp8_profile@10	-45.06	0.09	-1345	-450		
Exp8_profile@11	-44.74	0.07	-1345	-250		
Exp8_profile@17	-44.26	0.06	-3845	1785		
Exp8_profile@18	-43.99	0.07	-3695	1785		
Exp8_profile@23	-44.31	0.06	2965	2035		
Exp. 8 Overgrowth						
Exp8_profile@12	-45.35	0.06	-745	2125	-0.68	Y
Exp8_profile@13	-43.83	0.07	-845	1425	1.07	Y
Exp8_profile@14	-43.80	0.06	-345	585	1.36	Y
Exp8_profile@19	-44.03	0.06	-1095	1785	0.75	Y
Exp8_profile@20	-43.68	0.09	-45	2035	1.03	Y
Exp8_profile@21	-43.49	0.10	455	2035	1.21	Y
Exp8_profile@22	-43.07	0.06	915	2035	1.64	Y
average					*0.91*	
2 s.e.					*0.57*	
minimum					*-0.68*	
Exp. 9 MEX						
Exp9_MEX@1	-44.28	0.12	-2443	5243		
Exp9_MEX@2	-44.48	0.17	-2393	5143		
Exp9_MEX@3	-44.35	0.10	-2643	5143		
Exp9_MEX@4	-44.38	0.13	-2043	-2557		
Exp9_MEX@5	-44.28	0.14	-2043	-2757		
Exp9_MEX@6	-44.52	0.10	-1793	-2857		
Exp. 9 Overgrowth						
Exp9_growth@1	-45.71	0.12	-2443	1843	-0.76	N
Exp9_growth@2	-45.67	0.08	-2443	1643	-0.72	N
Exp9_growth@3	-44.92	0.09	-2443	1443	0.04	N
Exp9_growth@4	-44.87	0.15	-2043	1843	0.08	N
Exp9_growth@5	-45.21	0.10	-2043	843	-0.25	N
Exp9_growth@6	-45.16	0.16	-1593	443	-0.21	N
Exp9_growth@7	-44.70	0.08	-1593	243	0.26	N
average					*-0.22*	
2 s.e.					*0.30*	
minimum					*-0.76*	
Exp. 10 MEX						

Continued on Next Page...

Sample	$\delta^{44/40}$Ca (‰)	2 s.e. (‰)	X (μm)	Y (μm)	$\Delta^{44/40}Ca_{s-f}$ (‰)	Corrected?
Exp10_profile@17	-44.13	0.07	-6252	952		
Exp10_profile@18	-44.15	0.05	-6252	752		
Exp10_profile@19	-44.50	0.12	-6052	752		
Exp10_profile@25	-44.41	0.05	1248	952		
Exp10_profile@26	-44.74	0.11	1248	752		
Exp10_profile@27	-44.61	0.09	1448	752		
Exp. 10 Overgrowth						
Exp10_profile@20	-44.48	0.06	-4952	952	0.40	Y
Exp10_profile@21	-46.50	0.11	-3952	952	-1.58	Y
Exp10_profile@22	-46.75	0.03	-2952	952	-1.78	Y
Exp10_profile@23	-44.88	0.08	-952	952	0.18	Y
Exp10_profile@24	-44.84	0.09	48	952	0.27	Y
average					*-0.50*	
2 s.e.					*0.97*	
minimum					*-1.78*	
Exp. 12 MEX						
Exp12_profile@1	-45.02	0.07	-2548	6957		
Exp12_profile@2	-45.33	0.10	-2548	6657		
Exp12_profile@11	-44.28	0.10	-2113	-557		
Exp12_profile@12	-44.29	0.14	-2113	-857		
Exp12_profile@13	-44.46	0.10	-2413	-1157		
Exp12_profile@16	-44.56	0.08	-500			
Exp. 12 Overgrowth						
Exp12_profile@3	-44.44	0.05	-1948	6057	1.22	Y
Exp12_profile@4	-47.23	0.10	-1648	4857	-1.71	Y
Exp12_profile@5	-46.94	0.06	-1648	4557	-1.45	Y
Exp12_profile@6	-47.57	0.06	-1648	4257	-2.11	Y
Exp12_profile@7	-45.97	0.07	-1048	4857	-0.44	Y
Exp12_profile@8	-45.80	0.11	-1048	4557	-0.31	Y
Exp12_profile@9	-44.19	0.09	-748	4257	1.28	Y
Exp12_profile@10	-45.33	0.07	-1048	3357	0.04	Y
Exp12_profile@14	-46.08	0.06	-1104	2209	-0.83	Y
Exp12_profile@15	-44.98	0.11	-1104	1309	0.17	Y
average					*-0.41*	
2 s.e.					*0.73*	
minimum					*-2.11*	
Exp. 13 MEX						

Continued on Next Page...

Sample	$\delta^{44/40}$Ca (‰)	2 s.e. (‰)	X (μm)	Y (μm)	$\Delta^{44/40}Ca_{s-f}$ (‰)	Corrected?
Exp13_profile@2	-51.41	0.06	-2720	5996		
Exp13_profile@8	-50.67	0.05	-1320	546		
Exp13_profile@9	-50.65	0.06	-1120	546		
Exp13_profile@15	-50.57	0.08	-745	-379		
Exp13_profile@16	-50.66	0.09	-545	-479		
Exp. 13 Overgrowth						
Exp13_profile@3	-51.31	0.06	-1720	5196	0.49	Y
Exp13_profile@4	-51.61	0.07	-2120	4396	0.09	Y
Exp13_profile@5	-51.40	0.06	-2120	3996	0.25	Y
Exp13_profile@6	-51.12	0.09	-2120	3596	0.47	Y
Exp13_profile@7	-51.33	0.08	-1520	3196	0.21	Y
Exp13_profile@10	-51.51	0.07	-1320	2796	-0.02	Y
Exp13_profile@11	-51.41	0.06	-970	2596	0.05	Y
Exp13_profile@12	-50.97	0.09	-845	2121	0.43	Y
Exp13_profile@13	-50.70	0.08	-745	1421	0.61	Y
Exp13_profile@14	-50.92	0.05	-745	121	0.23	Y
average					*0.28*	
2 s.e.					*0.13*	
minimum					*-0.02*	
Exp. 14 MEX						
Exp14_profile@15	-47.70	0.09	-1360	-4040		
Exp14_entcenter@1	-46.40	0.05	-1360	-3840		
Exp14_entcenter@4	-45.16	0.15	-1609	400		
Exp. 14 Overgrowth						
Exp14_entcenter@2	-38.23	0.11	-1761	-1239	8.76	N
Exp14_entcenter@3	-38.89	0.09	-1761	-1439	8.10	N
average					*8.43*	
2 s.e.					*0.54*	
minimum					*8.10*	
Exp. 15 MEX						
Exp15_profile@2	-44.90	0.06	-578	1165		
Exp15_profile@3	-44.73	0.08	-378	1365		
Exp15_profile@9	-45.30	0.08	-1703	5265		
Exp15_profile@10	-45.37	0.06	-1703	6065		
Exp15_profile@11	-45.30	0.05	-1503	6065		
Exp. 15 Overgrowth						
Exp15_profile@4	-45.13	0.08	-728	4165	0.55	N

Continued on Next Page...

Sample	$\delta^{44/40}$**Ca** (‰)	**2 s.e.** (‰)	**X** (μ**m**)	**Y** (μ**m**)	$\Delta^{44/40}$**Ca**$_{s-f}$ (‰)	**Corrected?**
Exp15_profile@5	-45.33	0.07	-728	4065	0.35	N
Exp15_profile@6	-45.11	0.10	-728	3715	0.58	N
Exp15_profile@7	-45.07	0.05	-503	4065	0.62	N
Exp15_profile@8	-44.44	0.09	-1703	3565	1.24	N
average					*0.67*	
2 s.e.					*0.30*	
minimum					*0.35*	
Exp. 18 MEX						
Exp18_MEX@32	-44.78	0.14	-913	1570		
test@6	-44.87	0.09	-752	1596		
Exp18_MEX@33	-44.92	0.09	-913	1670		
Exp18_MEX@34	-44.58	0.12				
Exp18_MEX@35	-44.75	0.06				
Exp18_MEX@36	-44.65	0.13				
Exp. 18 Overgrowth						
test@5	-46.70	0.11	-520	-2930	-1.37	N
Exp18_ctr@1	-47.16	0.08	-1380	-2858	-1.83	N
Exp18_ctr@2	-47.20	0.10	-1380	-2983	-1.87	N
Exp18_ctr@3	-46.97	0.11			-1.65	N
Exp18_ctr@4	-46.66	0.10			-1.34	N
Exp18_ctr@5	-46.60	0.14			-1.27	N
Exp18_ctr@6	-46.54	0.12			-1.21	N
average					*-1.51*	
2 s.e.					*0.21*	
minimum					*-1.87*	

Appendix D

Methods for solving kinetic equations

D.1 Calculation of growth rate inhibition by non-incorporating impurities

The following procedure may be used to calculate precipitation rate as a function of calcium (A), carbonate (B) and impurity (M) ion concentration in solution using fitted attachment and detachment rate coefficients (k_A, k_B, k_M, ν_A, ν_B and ν_M).

- Solve for kink probabilities, P_A, P_B and P_M using Eqs. 5.14-5.16
- Calculate the net kink propagation rate by substituting kink probabilities into Eq. 5.1 for each ion. The kink propagation rate of M is 0 by definition, so

$$u_{net} = u_A + u_B = k_A(A)P_B + \nu_A P_A + k_B(B)P_A + \nu_B P_B.$$

- Calculate resistance to nucleation for A and B (Ω_A and Ω_B; Eq. 5.10).
- Determine kink density (ρ) by substituting u_{net}, Ω_A and Ω_B into Eq. 5.12 to calculate C. Substitute C into Eq. 5.11, which may be solved using the quadratic equation.
- Finally, surface normal growth rate and step velocity may be determined by inserting u_{net} and ρ into Eq. 5.6.

D.2 Numerical solution of steady state growth rate and composition

Both growth rate and steady state crystal composition depend on A-, B- and M-type kink propagation rates. In the case of impurity incorporation, kink probabilities cannot be calculated analytically. Instead, the constraint equations (5.3-5.5) may be solved numerically as a function of solution composition (ion activities (A), (B) and (M)) and attachment and detachment rate coefficients (k_A, k_{B-A}, k_{B-M}, k_M, ν_A, ν_{B-A}, ν_{B-M} and ν_M). We use pseudocode to demonstrate a method for solving the system of equations using the Newton-Raphson method, but the equations may also be solved using a built-in solver such as fsolve in Matlab.

- Define inputs: ion activities, attachment rate coefficients, initial detachment rate coefficients, endmember carbonate solubilities, and thermodynamic constants (i.e. a_0).
- Initialize activity coefficients and kink probabilities: $\gamma_{AB} = 1$, $\gamma_{MB} = 0$, $P_A = 0.50$, $P_M = 0.01$ ($P_B = 1 - P_A - P_M$).
- For 20 iterations
  - (Re)calculate ν for A, B-A, M and B-M using Eqs. 5.31 and 5.32.
  - Pass rate coefficients and kink probabilities as values to the solver function.
    - Define step size for varying P_A and P_M (dP $\sim$ 1e-8) and step length ($\alpha \sim 0.2$).
    - For 50 iterations
      - (Re)calculate u_M and u_A using (1) P_A and P_M, (2) P_A + dP and P_M, and (3) P_A and P_M + dP.
      - Calculate the M/A ratio of the solid for (1) - (3), where $r_x = u_M/u_A$ for each set of kink propagation rates (Eq. 5.23).
      - Calculate u_{B-A} and u_{B-M} for (1) - (3) using Eqs. 5.21 and 5.22.
      - Define errors based on Eqs. 5.3 and 5.4 for (1) - (3). For case (1),

$$E_{A1} = u_{A,1} - u_{B-A,1}$$

$$E_{M1} = u_{M,1} - u_{B-M,1},$$

        where $u_{i,1}$ is the kink propagation rate for kink type i calculated using case (1) kink probabilities.
      - Calculate error sensitivity relative to changes in P_A and P_P. For example, sensitivity to changes in P_A may be expressed,

$$dE_A/dP_A = (E_{A2} - E_{A1})/dP$$

$$dE_M/dP_A = (E_{M2} - E_{M1})/dP.$$

· Define the Jacobian,

$$\mathbf{J} = \begin{pmatrix} dE_M/dP_A & dE_M/dP_M \\ dE_A/dP_A & dE_A/dP_M \end{pmatrix}.$$

· Calculate the change in kink probabilities, $\mathrm{d}\mathbf{P} = \begin{pmatrix} dP_A \\ dP_M \end{pmatrix}$, where

$$d\mathbf{P} = \mathbf{J}^{-1} \begin{pmatrix} E_{M1} \\ E_{A1} \end{pmatrix}.$$

· Update A and M kink probabilities, $\mathrm{P}_A = \mathrm{P}_A + \alpha\ dP_A$ and $\mathrm{P}_M = \mathrm{P}_M + \alpha\ dP_M$.

∗ Calculate P_B = 1 - P_A - P_M using final P_A and P_M.

– Calculate kink propagation rates for A and M from Eq. 5.1 using numerically determined kink probabilities.

– Calculate the steady state M/A ratio (r_x; Eq. 5.23).

– Solve for the partition coefficient (K_p; Eq. 5.33).

– Substitute r_x into Eqs. 5.21 and 5.22 for u_{B-A} and u_{B-M}, and finally calculate u_{net}.

– Follow Appendix D.1 directions to determine ρ, v_{st} and R.

- After 20 iterations, the calculated precipitation rate (R) and partition coefficient (K_p) should reach steady state values.